Universität Ulm
Institut für Festkörperphysik

FePt and CoPt nanoparticles prepared by micellar method: Effects of A1→L1$_0$ transition on oxidation resistance and magnetic properties

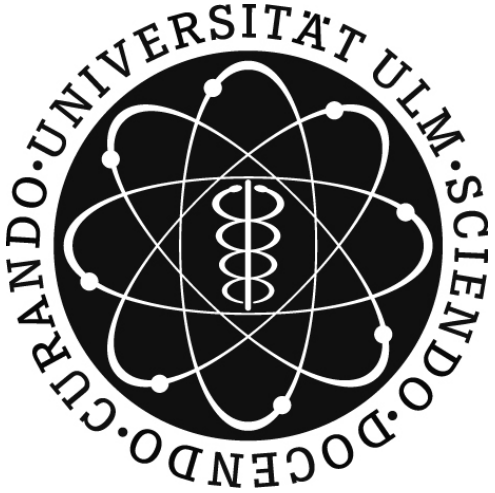

Dissertation

zur Erlangung des Doktorgrades Dr. rer. nat.
der Fakultät für Naturwissenschaften
der Universität Ulm
vorgelegt von

Luyang Han

Feb, 2011

For my parents

Zusammenfassung

In dieser Arbeit werden die Untersuchungen an mizellar hergestellten FePt und CoPt Nanopartikeln gezeigt. Die metallischen Nanopartikel mit einem Durchmesser von 2-12 nm und einem interpartikulärem Abstand von 20-150 nm wurden auf Si Substraten deponiert und auf ihr magnetisches und chemisches Verhalten bezüglich ihrer Oxidation untersucht.

Die Messungen an mit Wasserstoffplasma behandelten, 5,8 nm FePt Nanopartikeln mittels magnetischem Röntgenzikulardichroismus (XMCD) zeigen, dass das magnetische Verhalten dem der chemisch ungeordneten A1-Phase von FePt-Vollmaterial entspricht. Nach Tempern der Partikel bei Temperaturen um 650 °C findet ein partieller Phasenübergang in die $L1_0$ Phase statt. Dies kann belegt werden durch hochaufgelöste Transmissionselektronenmikroskopie (HRTEM), wobei in den Partikeln Defekte wie Zwillingsgrenzen oder Stapelfehler auftreten. Durch eine Erhöhung der Temperatur oder eine Verlängerung des Temperprozesses erhöht sich Anzahl der Partikel in der $L1_0$ Phase. Dabei liegt die durchschnittliche magnetische Anisotropieenergie der umgewandelten Partikel unterhalb 30% der Anisotropie der geordneten Phase von FePt-Vollmaterial. Nach Tempern der Nanopartikel oberhalb 750 °C erniedrigt sich hingegen die mittlere magnetische Anisotropie. Der gleiche Phasenübergang aus der A1 in die $L1_0$ Phase lässt sich auch bei FePt-Nanopartikeln mit unterschiedlichn Durchmessern sowie bei CoPt-Partikeln feststellen. Dabei sinkt das Spinmoment von Eisen in FePt-Nanopartikeln mit kleiner werdendem Durchmesser, wohingegen das Bahnmoment nahezu konstant bleibt. Gemessen bei Raumtemperatur sind die magnetischen Momente signifikant kleiner als bei tiefen Temperaturen (T<20 K), woraus sich schließen lässt, dass auch die Curietemperatur der FePt- und CoPt-Nanopartikel im Vergleich zu dem jeweiligen Vollmaterial reduziert ist.

Während des Temperns tritt bei FePt Nanopartikeln eine Segregation des Platin auf, was sich durch eine diffusionsgetriebene Anreicherung von Pt an der Oberfläche der Nanoteilchen äußert. Dies konnte anhand des verminderten Fe-Anteils in den Spektren, aufgenommen mit Röntgenabsorptionsspektroskopie (XAS) und Röntgenphotoelektronenspektroskopie (XPS), nachgewiesen werden. Die Anreicherung des Pt in der Außenhaut der Teilchen reduziert die Oxidation von Nanopartikeln mit einem Durchmesser $d > 5$ nm um einen Faktor 100-1000. Bei kleineren Partikeln konnte dieser Effekt nicht nachgewiesen werden. Dieses Verhalten kann durch die Abschätzung der Platinschichtdicke anhand eines Kern-Schale-Modells erklärt werden.

Abstract

In this thesis FePt and CoPt alloy nanoparticles are prepared with reverse micelles. The metallic nanoparticles with diameters of 2-12 nm and interparticle distances of 20-140 nm are obtained on Si substrates. The magnetic properties of FePt and CoPt nanoparticles as well as oxidation behavior of FePt nanoparticles are investigated.

X-ray magnetic circular dichroism (XMCD) measurements on 5.8 nm FePt nanoparticles after hydrogen plasma reduction at 300 °C reveals that the magnetic moment per Fe atom and magnetic anisotropy energy match chemically disordered FePt in A1 phase. Annealing at 650 °C transform portion of FePt particles to chemically ordered $L1_0$ phase. The presense of nanoparticles in $L1_0$ phase is identified by high-resolution transmission electron microscopy (HRTEM) investigation, where it is also observed that large fraction of the particles contain defects such as twin boundaries and stacking faults. By increasing the annealing temperature or prolonging annealing time, ratio of transformed particles increases. The average magnetic anisotropy energy of the transformed particles is below 30% of the value of bulk FePt in $L1_0$ phase. Annealing at above 750 °C , however, decreases the average magnetic anisotropy in the sample. Similar A1$\rightarrow$$L1_0$ transition is observed in FePt nanoparticles with different diameters as well as in CoPt nanoparticles. The spin moment of Fe in FePt nanoparticles decreases with smaller particle diameter, while the orbital moment stays almost constant. Magnetic moments at room temperature are significantly reduced compared to those at low temperature, suggesting the Curie temperatures in FePt and CoPt nanoparticles are significantly lower than in the bulk.

The annealing also induces Pt segregation towards the surface in FePt nanoparticles, which is identified by the decreased apparent Fe content measured by X-ray photoelectron spectroscopy (XPS) and X-ray absorption spectroscopy (XAS). The segregation of Pt enhance the resistance against oxidation in nanoparticle larger than 5 nm by a factor of 100-1000, but has no influence on smaller particles. Such difference is explained by the thickness of Pt segregation, which is estimated by a core-shell modeling.

Contents

1 Overview **1**

2 Introduction **3**
2.1 Preparation of magnetic nanoparticles 3
2.2 Magnetism of nanoparticles 5
2.3 Introduction to FePt and CoPt systems 9
2.4 Magnetic properties of FePt and CoPt nanoparticles 15

3 Experimental techniques and evaluation methods **17**
3.1 Overview of experimental methods 17
3.2 Quantification of XPS spectra 19
3.2.1 Model to describe XPS signal intensities 19
3.2.2 XPS spectra from core-shell structures 22
3.2.3 Evaluation of XPS spectra 24
3.3 Quantification of element-specific magnetic moment by XMCD 26
3.3.1 Introduction to XMCD and the sum rules 26
3.3.2 Experimental setup and the total electron yield 29
3.3.3 Saturation effect in the total electron yield method 30
3.3.4 Evaluation of XMCD spectra 34

4 Morphological, chemical and structural characterization of FePt and CoPt nanoparticles **39**
4.1 Sample preparation 39
4.2 Morphology and chemical state 40
4.3 Structure of FePt nanoparticles 43

5 Oxidation of FePt nanoparticles and the effect of surface segregation **47**
5.1 Experimental details 47
5.2 Oxidation of FePt nanoparticles 48
5.3 Surface segregation of Pt 51

6 Magnetism of FePt and CoPt nanoparticles **57**
6.1 Experimental details 57
6.2 XAS and XMCD of FePt and CoPt nanoparticles 58
6.3 Formation of the $L1_0$ phase 60
6.4 Size dependent magnetic properties of FePt nanoparticles 72
6.5 Temperature dependent magnetization 76
6.6 Summary of magnetic properties 78

7 Summary **81**

Bibliography **85**

Acknowledgment **93**

Curriculum vitae **97**

Publications and conference contributions **99**

1 Overview

Since more than 50 years the binary alloys FePt and CoPt are known to exhibit high magnetic anisotropy in their chemically ordered $L1_0$ phase and their bulk properties are well understood [1, 2]. Although the materials have high coercivity, good mechanical properties and excellent chemical stability compared to other hard magnetic materials [3], they are rarely used as bulk magnets in industrial applications due to their high cost. On the other hand, thanks to the combination of high magnetic anisotropy and good corrosion resistance, FePt and CoPt thin films as well as nanoparticles are promising candidate for the next generation of magnetic data storage [4, 5, 6]. FePt nanoparticles also find applications in fields of biology and medicine, such as magnetic resonance imaging [7], drug delivery [7] and hyperthermia [8]. Apart from magnetism, FePt and CoPt nanoparticles can be used as catalysts in various of reactions, where both activity and selectivity of the reactions can be tuned by controlling the size, shape and composition of the particles [9].

Such diverse applications and researches in FePt and CoPt nanoparticles are triggered by the progress in preparation techniques to produce monodispersed nanoparticles with controlled particle size, shape and composition. Example of such preparation methods are wet-chemical methods [6], inert gas condensation [10] and micellar method [11]. However, FePt or CoPt nanoparticles prepared by these methods are commonly not in the $L1_0$ phase, but in chemically disordered A1 phase with very low magnetic anisotropy, which is usually not favorable for the applications. Transformation to the energetically favored, magnetically attractive $L1_0$ phase is kinetically blocked at ambient temperature and only after a subsequent annealing at temperatures above 600 °C partial chemical order can be established [6, 11]. Moreover, even after annealing the perfect $L1_0$ order has never been obtained in FePt or CoPt nanoparticles. Instead, magnetic anisotropy energies observed in the nanoparticles prepared by different procedures are typically below 30% of the bulk value [12]. The reduced magnetic anisotropy energy in FePt or CoPt nanoparticles, as well as their size dependent magnetic properties, are still not fully understood. This thesis contributes to the knowledge of magnetic properties FePt and CoPt nanoparticles. Especially the A1 $\rightarrow$ $L1_0$ phase transition is investigated in nanoparticles of different sizes and under different annealing conditions.

Another important consideration for potential applications of magnetic nanoparticles is the chemical stability. In the case of particles containing 3d elements like Fe or Co a propensity for oxidation has to be expected, and the oxidation will deteriorate or even completely destroy the desired magnetic properties. While the FePt and CoPt in the bulk are very noble [3], their chemical stability in nanoparticles is

still an open question. The detailed oxidation process is investigated for differently sized FePt nanoparticles, and the oxidation behavior of particles in A1 phase and partially $L1_0$ phase is compared.

The thesis is organized as follows: In Section 2 the micellar method is introduced. This method is used to obtain size-selected FePt and CoPt nanoparticles. Preparational details and its advantages as well as drawbacks to other methods are compared. Moreover a general introduction to magnetic nanoparticles and FePt as well as CoPt alloy systems are presented.

Before discussing the detailed oxidation and magnetic properties, feature such as size, interparticle distances, composition and crystalline structure of nanoparticles need to be characterized. The corresponding characterization methods are discussed in Section 3 and morphological, chemical and structural information about different nanoparticles are presented in Section 4. Among all characterization methods, two in-situ techniques are extensively used in this thesis: X-ray photoelectron spectroscopy (XPS) is used to track the oxidation process and possible Pt segregation, while X-ray magnetic circular dichroism (XMCD) measures the element-specific magnetic properties. The physical principles of these two methods, as well as their quantification are presented in detail in Section 3.

In Section 5 the oxidation of differently sized FePt nanoparticles in disordered and partially ordered phases under successive oxygen exposure is investigated. Observed huge differences in the resistance to oxidation are ascribed to Pt surface segregation, which is identified as an apparent shift of the stoichiometry towards Pt-rich side.

Section 6 focuses on the magnetic properties of the nanoparticles. Orbital and spin moments as well as elemental specific hysteresis loops are measured using XMCD. The formation of $L1_0$ order is investigated in FePt and CoPt nanoparticles. Especially the evolution of A1 $\rightarrow$ $L1_0$ transition is discussed in detail for 5.8 nm FePt nanoparticles. The observed magnetic anisotropy energies in nanoparticles are compared with results in the literature and the origin of the obtained low magnetic anisotropy is explored. Magnetic anisotropy and magnetic moments per Fe atom in differently sized FePt nanoparticles are also compared. Finally temperature dependence of magnetic moment is shortly discussed, giving the estimation of Curie temperatures of the nanoparticles. All the results are summarized in Section 7 to give a complete model which describes the different properties observed in FePt and CoPt nanoparticles.

2 Introduction

2.1 Preparation of magnetic nanoparticles

Different methods have been used to prepare monodispersed magnetic nanoparticles with diameter smaller than 100 nm, all of which can basically be distinguished between physical methods and chemical methods. An often used example of physical methods is the inert gas condensation, where nanoparticles are formed by sputtering atoms from certain target and the sputtered atoms agglomerate into clusters in a continuous inert gas flow before landing on the substrate [10]. By controlling the agglomeration process, the particle size can be controlled. Advantage of such a method is that the complete process is usually performed in vacuum, yielding a clean system without contamination or oxidation. Also the composition of particles can be tuned rather easily by controlling the target composition [13]. Extra size selection mechanism can be applied to the particles that are formed during the flight towards the substrate and very narrow size distribution can be obtained [14]. However, a major drawback of this method is the random deposition of particles on the substrate.

In chemical methods particles are formed in solution, where the precursors mixed with surfactant are let to react in a controlled manner. By adjusting the kinetics of chemical reactions and surfactants, not only spherical particles but a wide range of morphologies can be obtained, such as nanocubes [15] and nanowires [16]. Since the particles are formed and dispersed in solution, further treatment of the particle such as surface modification can be performed [17]. The particles can further be deposited on substrates forming an ordered array thanks to self assembly [18]. The chemical method requires a detailed control of reaction kinetics, and for another particle system a new combination of precursors and surfactants as well as reaction conditions have to be optimized.

The magnetic nanoparticles investigated in this work are prepared by a technique based on reverse micelles, which is a hybrid of chemical and physical method [19, 11]. The main idea of this method is shortly summarized in Fig. 1. The diblock co-polymer polystyrene-b-poly-2-vinylpyridine (PS-b-P2VP) or polystyrene-b-poly-2-vinylpyridine (PS-b-P4VP) is dissolved in non-polar solvent like toluene. Above certain concentration the polymer will self-assemble into spherical reverse micelle, where the core is hydrophilic and the shell is hydrophobic [20, 21]. The hydrophilic core can be utilized as a nanoreactor to carry the precursors of the nanoparticles. For loading the the micelles, metal salts are added as precursors to the micelle solution and stirred for 3 to 4 days until the salts are completely dissolved. The choice of

metal salts is critical to achieve successful loading. Roughly speaking, the salt must form certain chemical bonds with pyridine groups on the polymer chain [22, 23]. depending on the chemical reaction occurred, the allowed relative molar ratio of the salt to the pyridine unit on polyvinylpyridine chain (loading ratio) is different for different salts.

In the second step, precursors loaded micelles are deposited on a substrate by dip-coating. By controlling the dipping speed, micelles will arrange in hexagonally closed-packed monolayer [19]. The sample is then exposed to oxygen plasma. During the plasma process the polymer is completely removed and the metal salts loaded in the micelle are transformed to the corresponding metal oxide nanoparticles. A subsequent hydrogen plasma can be used to reduce the oxide to metallic state. The procedure described here belongs to a large class of methods, by which nanoparticles are prepared thanks to the self-assembly of diblock-co-polymer [24]. As summarized by Förster and Antonietti, precursor loading can also be introduced in monomers before polymerization, in polymer molecules before the micelle formation and even after the self-assembly of micelles on the substrate. Similarly, the formation of nanoparticles can also be achieved by chemical reaction within the micelles when the micelles are still in solvent [22]. Among different procedures, the method introduced in this study is the most versatile when dealing with nanoparticles with different chemical compositions.

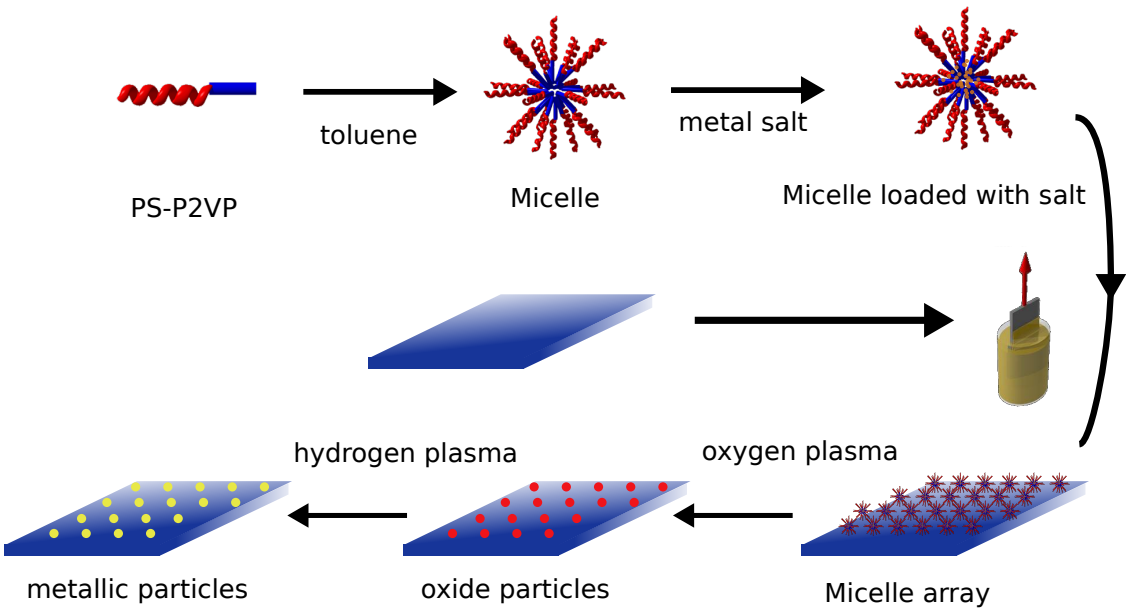

Figure 1: Successive steps of the micellar approach for preparation of supported nanoparticles. Details are explained in the text.

By the micellar approach, the particle size, interparticle distance as well as chem-

ical composition can be adjusted within certain range. The size and the distance of the particles are mainly determined by the chain length of the P2VP and PS, which in turn governs the size of the micelle core and shell [21]. The particle size can be further controlled by changing the loading ratio. This will lead to different particle size, while the interparticle distance remains constant. The interparticle distance can be further controlled by the speed of dip-coating [25]. In this study the particle sizes range from 2 to 12 nm in diameter, and interparticle distances vary between 25 to 200 nm.

2.2 Magnetism of nanoparticles

The magnetic properties of nanoparticles are the central topics of this study. For a thorough understanding of the magnetism of nanoparticles, several concepts will be introduced in this subsection.

One of the most important concept in mangetic nanoparticles is the magnetic anisotropy energy (MAE), which describes that the energy of magnetic material depends on the relative orientation of the magnetization with respect to the material [26]. Because of such energy difference, the magnetization will stay at a position where total energy is minimized, which leads to stable magnetization in the material. Such direction is called the easy direction of magnetization.

MAE can have many different origins, but all can be divided into two categories. The first kind arises purely from magnetostatics and can be explained at macroscopic scale. Whenever magnetization within the material is not homogeneous or not parallel to the surface, a stray field will emerge and interact with all the magnetization in the system. This effect give rise to MAE such as the shape anisotropy, where the energy depends on the relative orientation of magnetization to the material's shape. For example, the easy direction for a cylinder is along its axis and for a thin film it's in the plane. This also means if the shape is isotropic, i.e. spherical, there will be no shape anisotropy.

The second kind of MAE originates from the quantum effect of spin-orbit coupling and is working at atomic scale. Due to spin-orbit coupling, changing the orientation of magnetic moment of an atom will alter the charge distribution around the nucleus, which further leads to energy difference if the atom is located in an anisotropic potential field. Example of such MAE is the magnetocrystalline anisotropy, where the atoms are subjected to the potential field of the crystal lattice.

In the simplest case, the symmetry of MAE is uniaxial. By expanding to different orders, the MAE can be expressed as:

$$E = E_1 \sin^2\theta + E_2 \sin^4\theta + \dots \tag{1}$$

, where E_1, $E_2 \dots$ are the coefficients of the expansion and θ is the angle between magnetization orientation and easy axis. In case of magnetocrystalline anisotropy, the MAE is usually normalized to unit volume $K_u = E/V$. The value of K_u usually is between 10^3 to 10^7 J/m^3. Such energy density is relatively low compared to the internal energy of the material, which is on the order of 10^9 J/m^3 at room temperature. Although the MAE is much smaller than thermal energy at room temperature, the MAE can still fix the orientation of magnetization with respect to the material. The reason lies in the fact that the strong exchange coupling in ferromagnetic material tends to align all the moments in parallel. In the simplest view, to change the orientation of one moment all the moments in the material need to rotate coherently, which means the effective energy barrier to switch magnetization direction is proportional to the volume of the material. On the other hand, the effect of thermal fluctuation is applied independently on all atoms within the material, meaning that the effect is independent of the system size. In larger systems, the MAE is able to create an energy barrier sufficient to stabilize the magnetic moments against thermal fluctuation [26].

In the nanoparticles prepared in this study, the major contribution to MAE is the magnetocrystalline anisotropy from FePt or CoPt crystalline structure. Assuming that the particles are spherical, there is no shape anisotropy for single particles. However, another kind of shape anisotropy due to the dipole-dipole coupling between neighboring particles might arise. The energy of such coupling is:

$$E = -\frac{\mu_0 m_1 m_2}{4\pi r^3}(2\cos\alpha\cos\beta - \cos\gamma\sin\alpha\sin\beta) \tag{2}$$

, where m_1, m_2 are the dipole moment of each particle, r the distance between the two moments. The value of this energy depends on the relative angle of two moments with respect to the direction vector between two moments as α and β and the dihedral angle between the two moment-direction vector plains as γ. This energy contribution will be significant, if the distance between the particle is small.

The micellar method usually produces nanoparticles separated by relatively large distances. A typical example is 10 nm FePt particles separated by 50 nm. The anisotropy due to dipole coupling in this case is estimated to be 7.12 meV, while the magnetocrystalline anisotropy per particle is $K_u V = 22.9$ eV assuming the bulk saturation magnetization and magnetic anisotropy of FePt [27]. However, if all the FePt particles form a closed packing such that the particles touch each other,

energy of dipole coupling will increase to 7.6 eV. As a result, particles investigated in this study are all magnetically separated and the only effective anisotropy is the magnetocrystalline anisotropy of each single particle.

In very small nanoparticles, the effect of thermal fluctuation might overcome the energy barrier of the MAE and flip the direction of moment. The rate of such flipping can be expressed by the equation proposed by Néel [28]:

$$\tau = \tau_0 \exp\left(-\frac{K_{eff}V}{k_B T}\right) \tag{3}$$

, where $k_B T$ stands for thermal fluctuation and $K_{eff}V$ the total energy barrier from MAE. τ_0 is the attempt frequency and is physically related to the coupling between lattice vibration and moment fluctuation. τ_0 lies usually between 10^9 to 10^{12} Hz [29]. When $1/\tau$ is much larger than the typical measurement time, the magnetization will be stable and nanoparticles show ferromagnetic behavior. Considering the usual time span of the measurement in 10-30 min., a stable magnetization requires:

$$K_{eff}V > 30 k_B T \tag{4}$$

Conversely, when $1/\tau$ is much smaller the the measurement time, the magnetization will flip randomly and the nanoparticles show no net magnetization without external field. The behavior is named superparamagnetism, where the total moments of one nanoparticle rotate collectively like a macro spin [30].

Another important effect in magnetic nanoparticle is the emerging of single-domain state. At macroscopic level, the moments in ferromagnetic material tend to form magnetic domains with closed loop configuration in order to reduce the stray field and thus the system's energy. However, the domain wall that separates different domains will cause extra energy and including domain wall in very small structure will not be energetically favorable. Considering a spherical particle with uniaxial magnetic anisotropy energy, a critical size for single domain can be deduced by comparing the total energy of the homogeneous magnetized sphere and the configuration with a single domain wall. For material with high magnetic anisotropy, the critical diameter of the sphere can be expressed as [31]:

$$D_c \approx \frac{9\sqrt{AK_u}}{\mu_0 M_s^2} \tag{5}$$

, where A is the exchange stiffness constant, K_u the uniaxial anisotropy constant, M_s is the saturation magnetization. In case of FePt $D_c \approx 46$ nm is obtained. The nanoparticles investigated in this study are well below such size, thus all are essentially single-domain.

The response of magnetic nanoparticles in external magnetic field can be described by the model proposed by Stoner and Wohlfarth [32]. The model originally set forth to explain the magnetism of alloys but later found its applications in magnetic nanoparticles. The details of such applications are discussed in many literature [33, 34, 35]. Here, the main ideas of the model are as summarized:

- The total magnetic moment of the sample is the contribution of many magnetic particles, and each particle is single-domained and all the magnetic moments rotate coherently.
- The magnetic anisotropy of the particles is uniaxial.
- The energy of the particle is described as the sum of magnetostatic energy due to external field and magnetic anisotropy energy:

$$E = K_u V \sin^2(\phi - \theta) - \mu_0 M_s V H \cos\phi \tag{6}$$

, where ϕ is the angle between the external field H and magnetization M_s, θ is the angle between easy direction of uniaxial anisotropy and external field. The orientation of the moment will stay at the position where the total energy is at its local minimum. If multiple local minima are present, the moment takes the orientation which is closest to its history. Such history dependency is the source of hysteresis in the Stoner-Wohlfarth model.

The response of the particle to external field depends strongly on the orientation of its easy direction. If all the particles are randomly oriented, the response is the average of all possible orientations, and the hysteresis loop of the particles have a defined shape, shown in Fig. 2.

Certain characteristics of the hysteresis loop can be related to the magnetic properties of the particles. More specifically, the following relations are valid:

$$M_r / M_s = 0.5 \tag{7}$$

$$\mu_0 M_s H_c / 2K_u = 0.479 \tag{8}$$

$$\mu_0 M_s H_s / K_u = 2 \tag{9}$$

The K_u is the uniaxial anisotropy energy density, M_s the saturation magnetization ,M_r the remanence magnetization and H_s the field needed to saturate the sample.

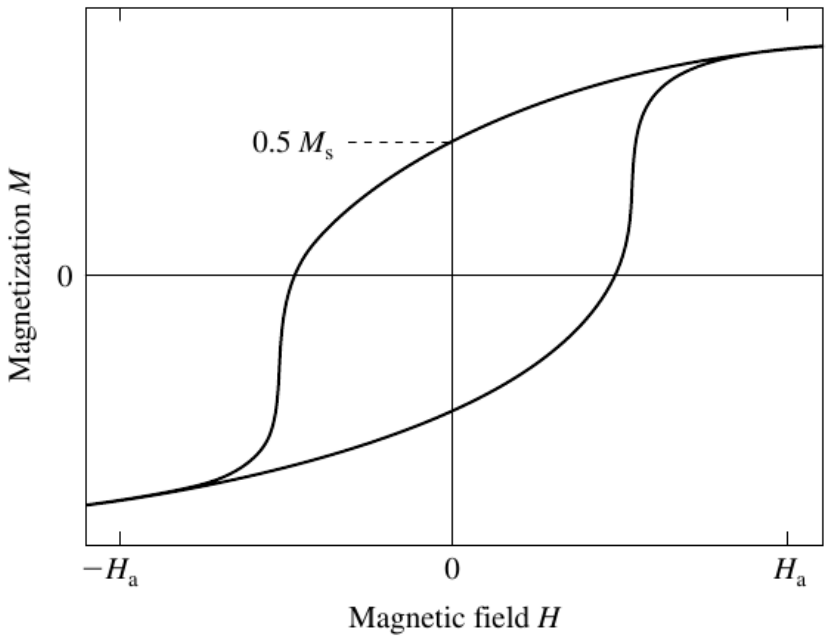

Figure 2: Hysteresis loop of an ensemble of randomly oriented uniaxial Stoner-Wohlfarth particles. Plot taken from [26].

The Stoner-Wohlfarth has not taken into account the thermal fluctuations, thus can only be used to explain the hysteresis when thermal energy is much lower than anisotropy energy of the particles. The Stoner-Wohlfarth model has been extended with thermal excitation according to the idea proposed by Néel [28] to explain the magnetic response at finite temperature [33].

2.3 Introduction to FePt and CoPt systems

FePt and CoPt alloy systems have attracted great interests mainly due to its possible application in magnetic data storage [6]. In this section the intrinsic properties of both alloy in bulk and thin film systems will be shortly reviewed.

FePt and CoPt alloys have very similar phase diagrams, as shown in Fig. 3. Both systems form A1 phase at high temperature, and can form three different ordered intermetallic phases M_3Pt, MPt, and MPt_3 (M stands for Co or Pt) at lower temperature. The MPt has $L1_0$ structure, while MPt_3 and M_3Pt have $L1_2$ structure [38]. The crystalline structure of A1 and $L1_0$ phases are shown in Fig. 4. The $L1_0$ phase is most interesting from the magnetic point of view due to its huge magneto-crystalline anisotropy. In this phase Co or Fe atoms and Pt atoms form an alternating layered structure. Due to strong spin-orbit coupling of the Pt 5d electrons [39] such structure has very large magneto-crystalline anisotropy, and the easy axis

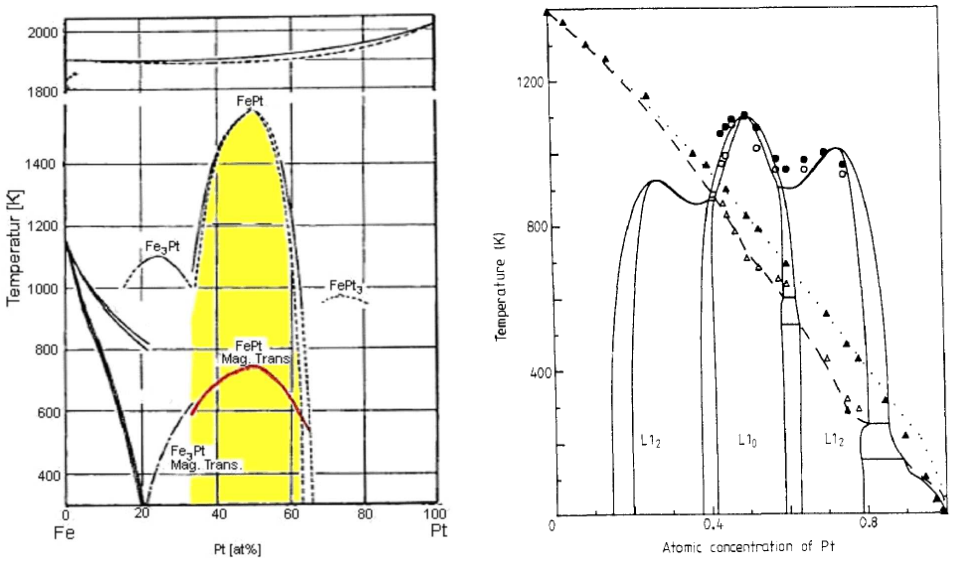

Figure 3: The phase diagram of FePt (left) [36] and CoPt (right) [2]. The ferromagnetic phase transition (Curie temperature) is also plotted for FePt. The two systems behave very similar. For both system, the $L1_0$ phase can be formed in a relative wide composition range. Details are discussed in the text.

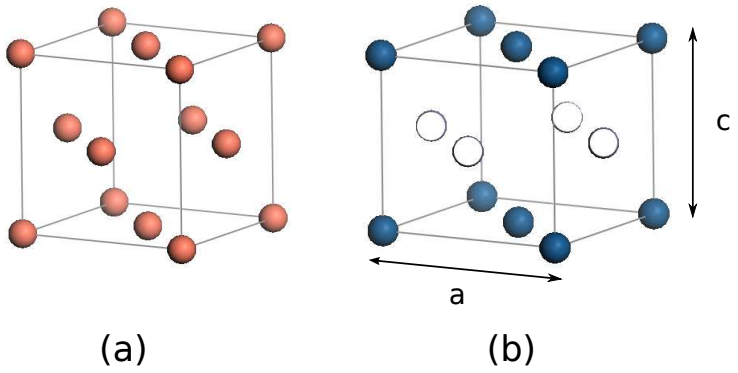

Figure 4: The crystalline structure of FePt and CoPt in A1 (left) and $L1_0$ (right) phase. The A1 phase has face centered cubic (fcc) structure and the two atoms occupy the fcc sites randomly, while the $L1_0$ has face centered tetragonal (fct) structure and the two atom species from alternating layers. The lattice of fct is slightly contracted in the perpendicular direction of the alternating atomic layers. The $L1_0$ bulk lattice constant for FePt is $a = 3.803\,\text{Å}$, $c = 3.701\,\text{Å}$, $c/a = 0.973$, for CoPt $a = 3.853\,\text{Å}$, $c = 3.713\,\text{Å}$, $c/a = 0.964$ [37]. One should notice that the lattice constants here correspond to the equiatomic ratio of Fe/Co to Pt, and the degree of chemical order S is almost 1. Deviations in the atom ratio and degree of order will change the lattice constant slightly. Using the above bulk lattice constants the densities are estimated to FePt 15.56 g/cm^3 and CoPt 15.30 g/cm^3, respectively.

is perpendicular to the alternating atomic layers. According to the phase diagram the $L1_0$ phase can be formed in a relative large range of composition: 35% - 62% Pt atomic percent for FePt and 42% - 58% Pt atomic percent for CoPt. For the atomic ratio of Co or Fe to Pt slightly deviated from 1:1, the $L1_0$ phase can still form, but the alternating atomic layer will not be pure Pt and Fe or Co, leading to slightly different lattice parameters and reduced magnetic anisotropy energies [37]. However, the same crystalline phase is maintained. This is very different from some other hard magnetic materials such as Co_5Sm, where the intermetallic phase with high MAE can only be formed in a very narrow stoichiometry window [40]. In such case, a slight deviation in the atomic ratio leads to a two phase mixture, which exhibits different magnetic properties and the system is inhomogeneous on the microscopic level. In this aspect, the FePt and CoPt nanoparticles with uniform magnetic properties are usually easier to prepare and the system is also simpler to characterize.

The phase diagrams shown in Fig. 3 is obtained under thermodynamical equilibrium. However, usual preparation methods [18, 41] produce a chemical disordered structure in the as-prepared state, where the crystalline structure is face centered cubic, and every atomic site is occupied by either Fe/Co or Pt atoms randomly, as shown in Fig. 4. This corresponds to the high temperature A1 phase shown in the phase diagram and the structure can be understood as a metastable system where atoms are "quenched" from an agitated state, which is thermodynamically unstable. Due to the disorder of the atoms, such structure usually has very low magnetic anisotropy energy [42]. In order to transform the A1 to $L1_0$ structure, an annealing step is typically required [41]. In this case the system is heated up to higher temperature, where thermodynamically the $L1_0$ phase is still favorable, and there is sufficient thermal energy to supply the kinetics of the transition. It has been shown that such order-disorder transition is a second order phase transition, and a corresponding order parameter S can be defined as [43]:

$$S = 2P - 1 \tag{10}$$

, where P is the probability that the Fe/Co or Pt atoms are at the "correct" sites of $L1_0$ lattice. In the fully ordered case, $P = 1$ and corresponding order parameter is also 1, while for complete disordered structures, one atomic species has equal probability to occupy both Fe/Co and Pt sites, thus $P = 0.5$ and the corresponding order parameter $S = 0$. Experimentally, S is usually measured with diffraction methods [44] by examining the relative intensity of (001) diffraction, which is not allowed in Al (fcc) phase, with respect to the (002) diffraction.

During the transition from A1 to $L1_0$ phase, the order parameter changes continuously with time and temperature. Similar to other order-disorder transitions, the kinetics of the transition can be summarized as the C-shape curve in the time-temperature-transformation or TTT diagram, shown schematically in Fig. 5. The low transition rate at low temperature is due to the limited thermal energy to assist the kinetics, while at high temperature the free energy difference between A1 and $L1_0$ phase is reduced and the reduced thermodynamic driving force limits the transition rate.

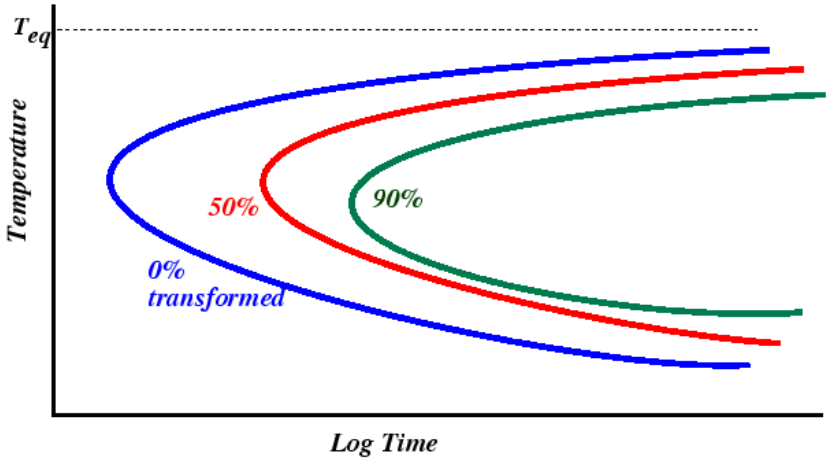

Figure 5: A schematic illustration of a TTT diagram. Each curve represents the degree transformed if held at a particular temperature. Details are explained in the text.

Given a typical measurement time in the lab, a kinetic transition temperature can be defined according to Fig. 5, where the A1→$L1_0$ transition starts. Such transition temperature in FePt reaches its minimum T_D = 375 °C at composition of 46 Pt at%, and increases rapidly to T_D = 500 °C for 55 Pt at%. The activation energy of the transition lies between 1.6 - 2.1 eV, with Pt-rich composition having higher activation energy [45]. The transition does not need long range atomic diffusion, but only rearrangement of atoms in near range is sufficient. It is shown by Monte Carlo simulations that the limiting factor for the transition is the number of vacancies available [46]. Introducing extrinsic vacancies, such as delivered by ion irradiation, will effectively reduce the activation energy and enhance the kinetics of the transition [47, 48].

The magnetic properties of FePt and CoPt have a close relation to the relative ratio of Pt and the crystalline structure. For $L1_0$ phase and 50 at% Pt, the system shows the highest magnetic anisotropy [37]. The important properties of the bulk material with 50 at% Pt and $L1_0$ phase are summarized in Table 1. Both systems

have uniaxial anisotropy. Only the lowest order of the anisotropy constant K_u is discussed in this study.

Table 1: Summary of experimental magnetic properties of FePt and CoPt in $L1_0$ phase with with 50 at% Pt [1, 49]. Both saturation magnetization and anisotropy energy are measured at room temperature. The coercive field H_c depends strongly on the microstructure and values given here are just examples of experimental data.

Name	M_s (kA/m)	H_c (T)	K_u (J/m^3)	T_c (K)
FePt	1140	12.28	7×10^6	750
CoPt	765	13	4.2×10^6	789

From saturation magnetization M_s and the crystalline structure it is estimated that the magnetic moment per FePt formula unit is 3.29 μ_B and per CoPt formula unit 2.28 μ_B, respectively. The magnetic moment of each atomic species and its corresponding spin and orbital moment has been measured by X-ray magnetic circular dichroism (XMCD). Results from the literature are summarized in Table 2. The majority of the total moment comes from Fe or Co atoms. The induced moments on Pt atoms contributes to only about 10-20% of the total magnetic moments. However, due to the presense of Pt, there are higher moments in Fe or Co compared to elemental Fe or Co. This effect is explained by the hybridization of Fe/Co 3d and Pt 5d orbits [50]. The moment per Fe atom increases with Pt content and reaches maximum at equiatomic composition, and stays almost unchanged when Pt content is further increased [51]. It is also clear from the table that the magnetic moment is not very sensitive to chemical order, which is quite different from systems such as FeAl [52]. Such phenomenon is confirmed by neutron diffraction measurement [53] and squid magnetometry [54]. As it is expected by the crystal field theory, the spin moment constitutes most of the magnetic moment and the orbital moment is very small. Although tiny contribution to the total moment, the orbital moment is closely related to the magnetic crystalline anisotropy [26], and in FePt/CoPt systems chemical order leads to slightly increased orbital moments, as shown in Table 2. The *ab-initio* calculations given in Table 2 yield reasonable prediction of spin moments for both systems. In case of FePt the spin moment measured by XMCD is slightly lower than the theoretical value. This effect is mainly due to the relatively large magnetic dipole contribution in the $L1_0$ phase, which contributes to the effective spin moment derived from the XMCD sum rules (refer to Section 3.3) [50]. The neutron diffraction measurements confirm that the moment of Fe atoms in FePt is 2.8 μ_B [53]. The theoretical calculations, however, typically underestimate the orbital moment. The measured orbital moment for FePt and CoPt is almost twice of

the theoretical prediction according to Table 2.

Table 2: Element specific spin moment μ_s and orbital moment μ_l in units of μ_B per atom for FePt and CoPt systems. All the systems have 50 at% Pt. The value is obtained either experimentally by XMCD or theoretically by layered Korringa–Kohn–Rostoker method (LKKR) and full potential method with linear muffin-tin orbit and local spin density approximation (FP-LMTO+LSDA). The experimental values for pure Fe and Co are also listed as reference.

System	Fe μ_s	Fe μ_l	Co μ_s	Co μ_l	Pt μ_s	Pt μ_l
FePt thin film A1 [55]	2.24	0.20			-	-
FePt thin film $L1_0$ [55, 51]	2.45	0.24			0.47	0.045
CoPt thin film A1 [56]			1.79	0.15	-	-
CoPt thin film $L1_0$ [57]			1.76	0.26	0.35	0.09
FePt $L1_0$ (LKKR) [58]	2.78	0.075			0.32	0.047
CoPt $L1_0$ (LKKR) [58]			1.72	0.095	0.35	0.059
FePt $L1_0$ (FP-LMTO+LSDA) [50]	2.87	0.072			0.33	0.046
CoPt $L1_0$ (FP-LMTO+LSDA) [50]			1.79	0.109	0.36	0.063
Fe thin film [59]	1.98	0.086				
Co thin film [59]			1.55	0.153		

The coercivity of FePt and CoPt in bulk or thin film depends strongly on its microstructure [60], thus the H_c value presented in Table 1 serves only as a practical example. The magneto-crystalline anisotropy energy (MAE), on the other hand, is an intrinsic property of the material and depends only on its atomic structure. Due to the $L1_0$ crystalline structure, the magneto-crystalline anisotropy energy in FePt and CoPt is uniaxial and can be expressed by a single energy density constant K_u. MAE depends strongly on the chemical ordering. For A1 phase the MAE energy is only 0.1 MJ/m^3 due to the high symmetry of the fcc lattice. Only chemically ordered $L1_0$ system shows the desired high MAE. The dependence of MAE to the chemical order S is investigated in thin film system by S. Okamoto et al. [27], where for $S < 0.8$, the K_u increases linearly with raising chemical order.

The Curie temperature T_C of FePt and CoPt is significantly reduced compared to pure Fe and Co, which arises from reduced exchange interaction. Compared to the chemically disorder phase, Curie temperature of chemically ordered CoPt decreases only about 10 K [49]. Measurements on different chemical composition of FePt reveals that the T_C is strongly influenced by the stoichiometry. Compared to $Fe_{50}Pt_{50}$, the T_C of $Fe_{59}Pt_{41}$ is reduced by 70 K [53]. The dependence of T_C with composition in FePt system is also shown in the phase diagram in Fig. 3.

2.4 Magnetic properties of FePt and CoPt nanoparticles

FePt nanoparticles have attracted great interests in research since Sun et. al. first demonstrated the preparation of monodispersed 4 nm FePt nanoparticles by chemical methods and the self-assembly of these particles on substrate in 2000 [18]. The prospect is that if the information could be stored magnetically on each nanoparticle, the information density will reach 4 Tb/in^2, exceeding even the harddisk nowadays in 2011 by almost a factor of 10. It was, however, quickly realized that several technical difficulties prevents its application. One of the major problem is that the particles prepared are in A1 phase with low MAE and the particles are essentially superparamagnetic at room temperature and cannot hold the information. While annealing up to 600 °C would create the desired $L1_0$ phase with high MAE, the particles agglomerate and the nice self-assembled array is destroyed [42]. A lot of efforts has been put into creating the $L1_0$ phase in nanoparticle without agglomeration [6]. One of such method is to disperse the particles at low concentration in a salt matrix, which allows high-temperature annealing without coalescence. After removal of the salt matrix the particles are recovered and dispersed again in solvent with the help of surfactants. The degree of order S reaches 0.8 for 4 nm diameter [61]. This high degree of order, however, has not been achieved for particles prepared by other method such as inert gas condensation [10] or micellar method [11], where both measurements yield much lower MAE compared to FePt in bulk.

There are many researches setting forth to explain the low degree of order obtained in FePt and CoPt nanoparticles. It has been observed that FePt nanoparticles after annealing show an inhomogeneous MAE [12], and similar result is also obtained for CoPt particles after annealing [62]. In both systems it is found that the MAE is composed of a high anisotropic portion that is due to chemical order and a low anisotropic portion that can essentially be described as in chemically disordered phase. This inhomogeneity suggests that the transition from A1 to $L1_0$ is incomplete, and the low degree of order obtained in these particles are in fact due to limited kinetics. Measurements in the CoPt system shows that chemical order is achieved in 2.4 nm CoPt particles after annealing at 500 °C for 16 hours. The annealing has to be performed at rather low temperature since the equilibrium order–disorder transition reduces from 825 °C to 500 - 650 °C, above which the $L1_0$ is thermodynamically unstable [63].

On the other hand, Monte Carlo simulations suggest that in nanoparticles the high degree of order is thermodynamically not favorable and extra disorder is introduced by the presence of surfaces [64]. Moreover, a tendency of Pt segregation on the (111) and (100) surface of FePt has been observed according to the simulation on

7 nm cuboctahedron FePt particles. Such segregation would shift the composition of the remaining FePt particles to Fe-rich, which further disrupt the chemical order [43]. It has also been shown experimentally by the salt-matrix annealing method that $S = 1$ can never be obtained in FePt nanoparticles smaller than 10 nm, and the maximum degree of order that can be obtained in 4 nm nanoparticles is 0.8 [61]. These researches suggest that the perfect $L1_0$ order in nanoparticles might be thermodynamically unfavorable.

The intrinsic magnetic properties such as Curie temperature and saturation magnetization change in FePt nanoparticles. XMCD measurements on colloidal FePt particles show reduced magnetic moment for Fe atoms compared to bulk FePt [51]. And the Curie temperature of 4 nm FePt nanoparticles is reduced by 50 - 100 K compared to bulk [65]. These observations suggest that the ferromagnetic order is influenced by the particle size. In extreme case, 2.5 nm FePt particles show antiferromagnetic order instead of ferromagnetism according to the *ab-initio* simulation [66]. This behavior of FePt is quite different from what has been observed on Co clusters, where with smaller cluster size increased moment and enhanced anisotropy energy are observed [67].

In this study the magnetic properties in FePt and CoPt nanoparticles are measured by XMCD, and its dependence with annealing conditions as well as particle sizes will be discussed in detail.

3 Experimental techniques and evaluation methods

3.1 Overview of experimental methods

The micellar technique typically produces a monolayer of nanoparticles with diameter smaller than 10 nm and interparticle distance larger than 50 nm, where the nanoparticles cover less than 8% of the projected surface area. This low coverage poses a great difficulty to the characterization. Generally speaking, all characterization methods can be divided into integral and microscopic methods. In the integral methods, the overall properties of the sample are measured, and the obtained result is the average over all the particles in the sample. For typical samples with a single layer of particles and relative large interparticle spacing used in this study, the difficulty is thus the small signal from the nanoparticles compared to the supporting matrix, e.g. the substrate. It is essential to separate the small contribution from the particles from the overall signal. With microscopic methods on the other hand, the properties of single nanoparticles are measured separately, and by measuring a large number of particles not only the averaged effects but also the distribution of the particle properties can be obtained [68]. Although microscopic methods yield great insights to the given characterization problem, obtaining properties of a single particle requires spatial resolution in the nanometer range, which is usually quite difficult. In this section different experimental methods used in this study will be shortly reviewed. Their application to magnetic nanoparticle systems will also be discussed.

The morphology is characterized by microscopic methods. Scanning electron microscopy (SEM) is mainly used to get a direct image of the sample, where the particle size, interparticle distance and the ordering of the hexagonal array can be easily resolved [68]. In this study Hitachi S-5200 field emission SEM is employed. Using the secondary electron signal the resolution of the SEM is about 1 nm. This is sufficient to detect and resolve the large structure of the particle, but the detailed shape of the particle is somehow blurred. Since the size of prepared particles ranges from 2 - 12 nm, with a resolution limit of 1 nm the particle diameter cannot be determined with high precision. Atomic force microscopy (AFM) is then used to determine the particle size more precisely [68]. Depending on the tip used in AFM, the lateral resolution is usually restricted to about 20 nm, but the vertical resolution can be as high as 0.1 Å. Since the interparticle distance is larger than 50 nm, the particles can be individually resolved by AFM. If we assume the particle is spherical, the AFM tip height change when scanning across the particle corresponds to the particle diameter. In this thesis the particle size is always determined using a

DI Nanoscope-III Multimode AFM in tapping mode. One should notice that both method are *ex-situ*, namely, the sample has to be removed from the vacuum and carried in ambient conditions to the corresponding microscope. During the investigation the sample is in high vacuum for SEM and stays in air for AFM. In both case exposure to ambient conditions might cause oxidation of the particles. It will be shown later in Section 5 that such effect is, however, not very prominent for the FePt systems.

Transmission electron microscopy (TEM) is used to investigate the detailed particle morphology and the crystalline structure of the particles [69]. In this thesis the TEM investigation is performed in collaboration with J. Biskupek and U. Kaiser from Arbeitsgruppe Materialwissenschaftliche Elektronenmikroskopie at Ulm University using the FEI Titan 80-300 Cs-corrected TEM. To prepare samples for TEM investigation, the nanoparticles are covered with a thin SiO_2 protective layer against oxidation, so that during the sample transfer and preparation stage, the particles are kept free of oxidation. The common bright field imaging mode can reveal the detailed particle morphology, while the high resolution mode (HRTEM) is used to measure the crystalline structure. In order to resolve the crystalline structures in HRTEM mode, the crystalline axis of the particles has to be aligned with respect to the electron beam. Considering the random orientation of the particle crystalline directions and the fact that only a small thin area on the sample can be investigated by TEM, only a small number of particles can be readily investigated to reveal their crystalline structure on one sample. For the HRTEM investigations, it is very important to get enough statistics to describe the overall properties of the particles.

The ordering parameter of $L1_0$ phase can also be measured by TEM. An indirect but easier method would be to measure the lattice constant of the particle. Using the relation between the degree of ordering and the lattice constant change [37], the order parameter S can be determined. Since the relative lattice constant change from A1 to $L1_0$ is around 3%, the lattice constant change has to be determined very precisely. However, in FePt and CoPt nanoparticle systems, due to relaxation on the surfaces the lattice constant in one particle can have significant changes larger than 3% and such change can also be inhomogeneous over the particle, as observed by Wang et al. [70]. This variation makes the estimation of overall lattice constant in FePt or CoPt nanoparticles unreliable, thus the lattice constant cannot be used to determine the order parameter. Instead, the scanning transmission mode (STEM) can be employed [69]. By either the nano-diffraction [71] or by the contrast change between Fe/Co and Pt layers [72] in STEM images, the degree of order can be quantified.

Some other techniques combined to TEM are also interesting for magnetic nanoparticles: the energy or wavelength dispersive X-ray spectroscopy (EDX, WDX) and electron energy loss spectroscopy (EELS) combined with STEM could measure the chemical composition of single particles [69]. Electron holography [73] and Lorentz microscopy [74] mode in TEM can image the local magnetic field of a single magnetic nanoparticle. While the newly developed energy loss magnetic chiral dichroism (EMCD, ChiralTEM) holds the promise that it might be possible to measure the element-specific spin and orbital moment with nanometer resolution [75]. Due to the practical limits such microscopic investigations are not performed systematically and will not be included in this thesis.

The chemical and magnetic properties of the samples are mainly measured by integral methods. X-ray photoelectron spectroscopy (XPS) is used to measure the chemical composition as well as the chemical state of the nanoparticles [76], while X-ray magnetic circular dichroism (XMCD) is applied to determine the elemental specific magnetic properties [77]. Both techniques are performed in-situ under UHV conditions. In the following two subsections details of these two methods as well as their quantification will be discussed.

3.2 Quantification of XPS spectra

In this thesis XPS is measured using Al K_α radiation (1486.65 eV) and a *Specs* EA 10+ hemispherical analyzer operating at 100 eV pass energy. The system is optimized for overall signal intensity, and has relatively low energy resolution of about 0.5 eV. The working principle of XPS is discussed in many textbooks in detail, see e.g. [76]. In this subsection a detailed model of the XPS signal intensity will be discussed. It will also be shown how such model can be applied to the experimental spectra from nanoparticles and thin films.

3.2.1 Model to describe XPS signal intensities

To quantify signal intensities obtained in XPS, the detailed process involved in XPS has to be understood. A schematic view of a XPS system is shown in Fig. 6. When the X-rays enter the specimen, their intensity starts to decrease due to absorption. The reduction of the X-ray intensity follows an exponential decay with a corresponding absorption length λ_X, depending on the photon energy as well as the material [76]. In lab-based XPS, Al K_α and Mg K_α radiations are usually used, and the corresponding λ_X in most materials is much larger than 300 nm [78, 79]. Consider that the probing depth of XPS is usually less than 5 nm (discussed below), the

change of the X-ray intensity within the probing volume is less than 2% and can be regarded as a constant.

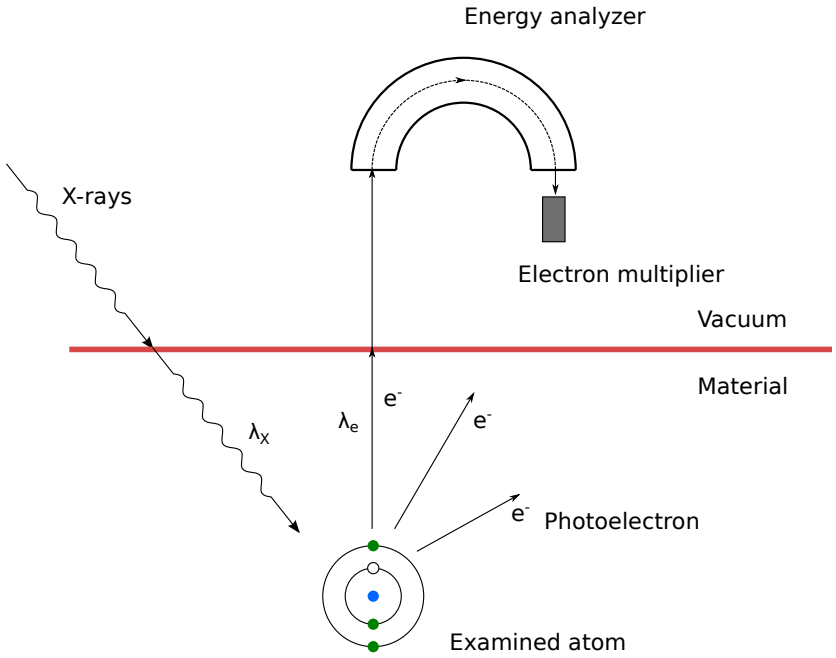

Figure 6: The working principle of XPS. Details are explained in the text.

Within the penetration depth of X-rays the photons are absorbed and electrons are generated. The amount of photoelectron yield depends on the coupling strength of incoming photons to electrons at certain orbits, expressed as subshell photoionization cross section $\sigma_{nl}(h\nu)$. As it is shown by the indices, the subshell photoionization cross section is different for each atomic orbit (n, l) and depends on the photon energy $h\nu$. Since the incoming X-rays travel almost parallel, the excited electrons have an angular distribution. If just the dipole transition term, which is the main contribution to σ, is considered, the differential cross section can be expressed as [80]:

$$\frac{d\sigma_{nl}(h\nu)}{d\Omega} = \frac{\sigma_{nl}(h\nu)}{4\pi}\left[1 + \beta_{nl}(h\nu)\left(\frac{3}{4}\sin^2\alpha - \frac{1}{2}\right)\right] \tag{11}$$

$\beta_{nl}(h\nu)$ is the energy dependent asymmetry parameter for subshell (n, l), and α is the angle between the incoming X-rays and the photoelectron. In experiments only the electrons towards the energy analyzer can be detected, thus the experimental XPS signal depends on the differential cross section at a given angle α. Both the subshell photoionization cross section and corresponding asymmetry parameters have been calculated by Yeh and Lindau [80]. One should notice that when the so-called magic angle $\alpha = 54.7°$ is fulfilled, the asymmetry term cancels out and

the cross section is independent of $\beta_{nl}(h\nu)$, which greatly simplified equation (11). Unfortunately, in our experimental setup $\alpha = 70°$, and the correction according to (11) has to be applied.

Given the corrected photonionization cross section $\sigma_{nl}(h\nu)$, the flux of the photoelectron from a given volume towards the detector can be expressed as:

$$dI_e(\mathbf{r}) = I_x \, \sigma_{nl}\,(h\nu)\, C(\mathbf{r}) dV \tag{12}$$

, where I_x is the intensity of X-rays, which is taken as a constant as discussed above. $C(\mathbf{r})$ reflects the atomic concentration of the examined element in the probing volume. In order to reach the energy analyzer, these electrons have to penetrate the material between the probing volume and vacuum, and the intensity of the electron flux will decrease due to scattering of electrons within the material. Unlike the interaction with X-rays, the electrons will gradually loose their energy when travelling within the material, and their absorption is dominated by inelastic processes. An electron inelastic mean free path (IMFP) λ_e can be defined to describe the exponential decrease of the electron intensity. Usually λ_e is much smaller than λ_X. In the case of XPS λ_e is smaller than 5 nm and the probing depth is mainly determined by the electron mean free path. λ_e depends strongly on the electron energy but seems to be independent of the material. In almost all materials the energy dependency of the λ_e follows a universal curve, as shown in Fig. 7 [81]. Such behavior can be well approximated by the formula proposed by Gries [82], especially when kinetic energy of electrons is larger than 200 eV [83].

The effect of the electron attenuation can generally be described by an attenuation factor $A(\mathbf{r}, E)$, which reads:

$$A(\mathbf{r}, E) = \exp\left(\int_\Gamma -\frac{s}{\lambda_e(\mathbf{r}+\mathbf{s}, E)} ds\right) \tag{13}$$

The integration path is a line that goes from the volume considered in (12) to the sample surface directed towards the energy analyzer, where λ_e is considered as position-dependent. As a result the attenuation is a function of the position and the kinetic energy of the electrons. The intensity of photoelectrons from certain element that leaves the specimen can then be calculated by integrating equation (12) over the volume of the specimen:

$$I_e = \int_\Omega I_x \, \sigma_{nl}(h\nu)\, C(\mathbf{r})\, A(\mathbf{r}, E) dV \tag{14}$$

The electrons that escape the sample surface will then enter the energy analyzer, and be detected by the electron multiplier. The energy analyzer has certain transfer

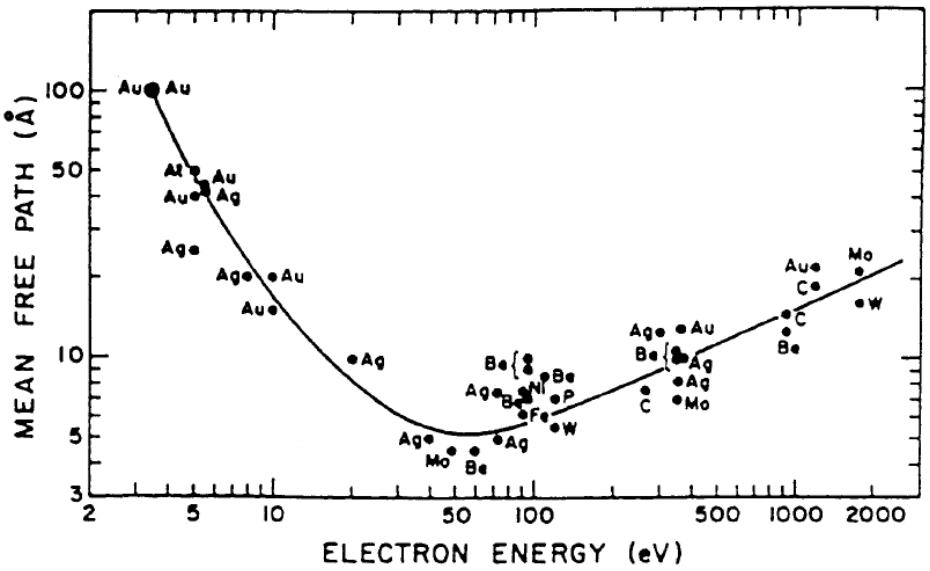

Figure 7: The "universal curve" of the electron IMFP vs. kinetic energy of the electron. The energy dependency is almost identical among different materials [84].

function $T(E)$ that leads to different signal transmission depending on the kinetic energy of the electrons. Thus the signal detected in a XPS measurement is:

$$I_{XPS} = I_e \, T(E) \, P \tag{15}$$

, with $T(E)$ is the transfer function and P a constant for normalization. In this study the $T(E)$ of the *specs* EA50 analyzer is proportional to the inverse of energy. The derived formula introduced here is quite general, and can be applied to any geometry and system. A simple case is found for a flat and homogeneous material, where an analytical result can be obtained:

$$I_{XPS} = I_x \sigma_{nl}(h\nu) \lambda_e(E) T(E) C P \tag{16}$$

For spherical nanoparticles, however, an explicit form of equation (15) is more complicated and the integration over the probing volume in equation (14) is usually approached numerically. In the next subsection a even more complicated core-shell structure will be discussed.

3.2.2 XPS spectra from core-shell structures

A very important geometry to consider is the core-shell structure, where the nanoparticles investigated by XPS are composed of spherical core and shell. The core and shell are assumed being of two different materials. If the particle size and the core

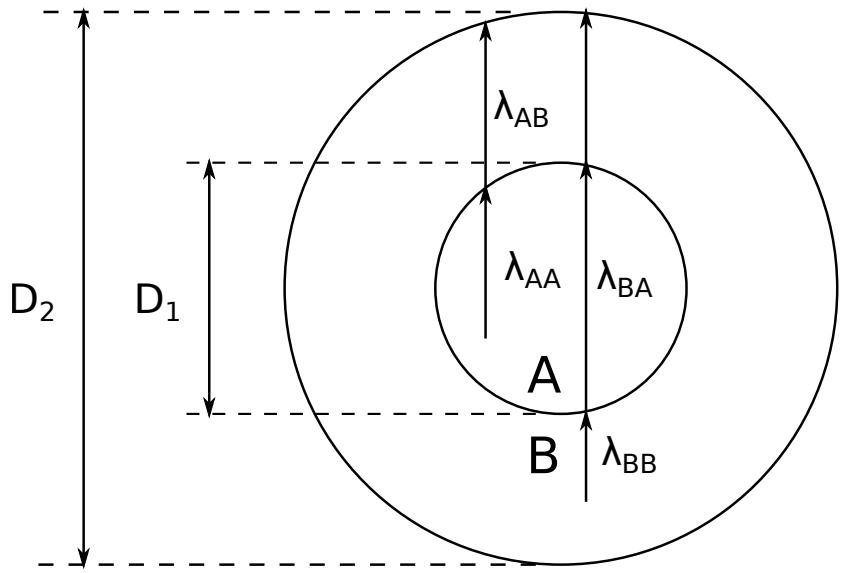

Figure 8: Core-shell model for XPS. Two different materials A and B compose the core and shell of a nanoparticle. The diameters of the particle and the core are D_2 and D_1, respectively. Photoelectrons from either A or B have to penetrate two different material, thus totally 4 different electron IMFP have to be considered when modeling observed XPS line intensities.

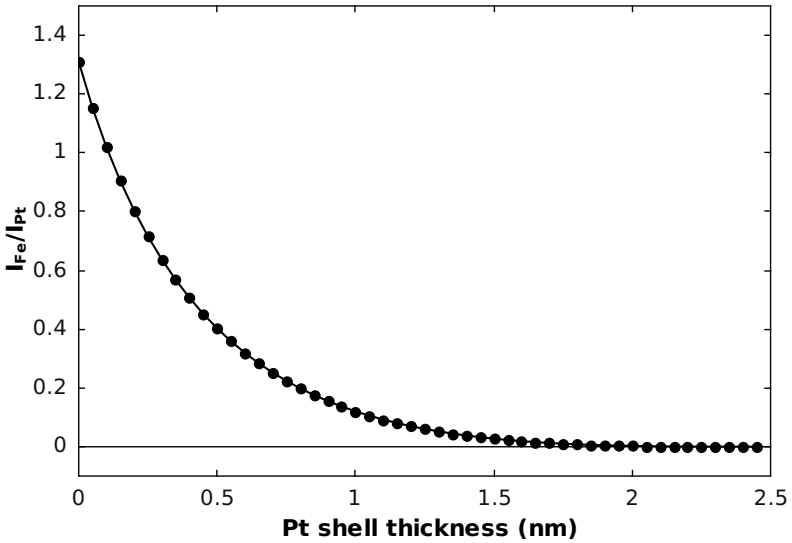

Figure 9: Relative intensity of Fe 2p to Pt 4f as a function of Pt layer thickness in a 5 nm core-shell nanoparticle composed of a FePt core and a Pt shell. Details are given in the text.

thickness is comparable to the probing depth of the XPS, the exact geometry of the particle will strongly influence the relative signals measured from core and shell atoms. On the other hand, by knowing the relative intensity from the core and shell, one can deduce the information about the particle geometry. The signal from homogeneous nanoparticles is thus a special case of the model above, where the shell thickness vanishes.

The core-shell model for XPS is illustrated in Fig. 8. The investigated material in core and shell are defined as A and B. In the model we have 6 characteristic lengths: the diameter of the whole particle D_2, of the core D_1, and the electron IMFP from A in material A λ_{AA}, from A in material B λ_{AB} and similarly λ_{BB} and λ_{BA}, as shown in the Fig. 8. The relative XPS intensities of A and B can be calculated by integrating equation (15). Due to the complicated geometry, the results can only be calculated numerically.

Experimentally, the relative intensity of A to B can be measured. And moreover, the particle diameter can be determined by AFM. If the all material properties of A and B are known, the thickness of the shell can be determined. An example is shown in Fig. 9. Assuming the particle diameter is 5 nm and composed of FePt core and Pt shell, the relative XPS intensity of Pt to Fe is estimated. The incident X-rays are from Al K_α. The relative difference in ionization cross-sections of Fe 2p and Pt 4f is less than 2% and assume to be identical [80]. The transmission function of the analyzer is assume to be $T(E) \propto 1/E$. The IMFP parameters used in the calculation are estimated using the predictive equation [82]:

- Fe 2p photoelectron in FePt: 1.10 nm
- Fe 2p photoelectron in Pt: 1.05 nm
- Pt 4f photoelectron in FePt: 1.70 nm
- Pt 4f photoelectron in Pt: 1.62 nm

The relative intensity of Fe 2p to Pt 4f is plotted against the Pt shell thickness. When there is no Pt shell the intensity of Fe is stronger than Pt due to the transmission function of the analyzer. As the Pt shell thickens, the relative intensity of Fe to Pt quickly decreases. By measuring the decrease of relative Fe intensity experimentally, the thickness of Pt shell can be deduced.

3.2.3 Evaluation of XPS spectra

In previous sections a model of XPS signal intensity has been established. However, the photoelectron current with certain kinetic energy obtained experimentally

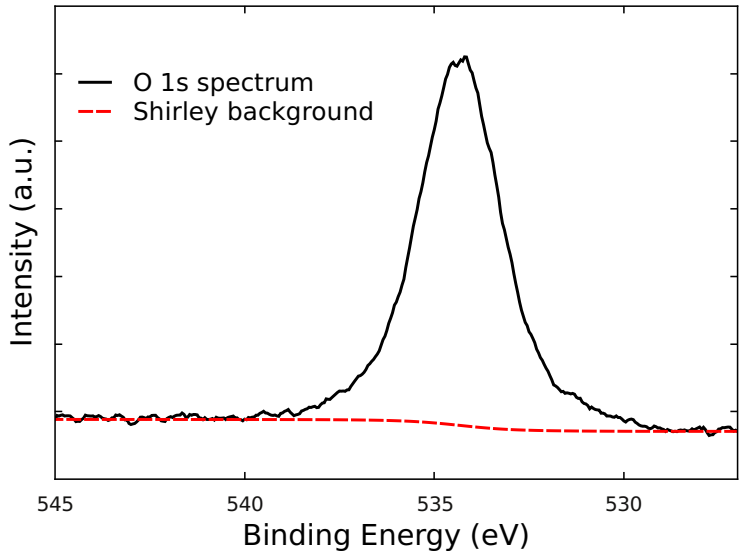

Figure 10: An example of the XPS spectra and its background. The O 1s peak is shown and Shirley background is plotted as the red dashed curve. The background has a smooth transition under the peak.

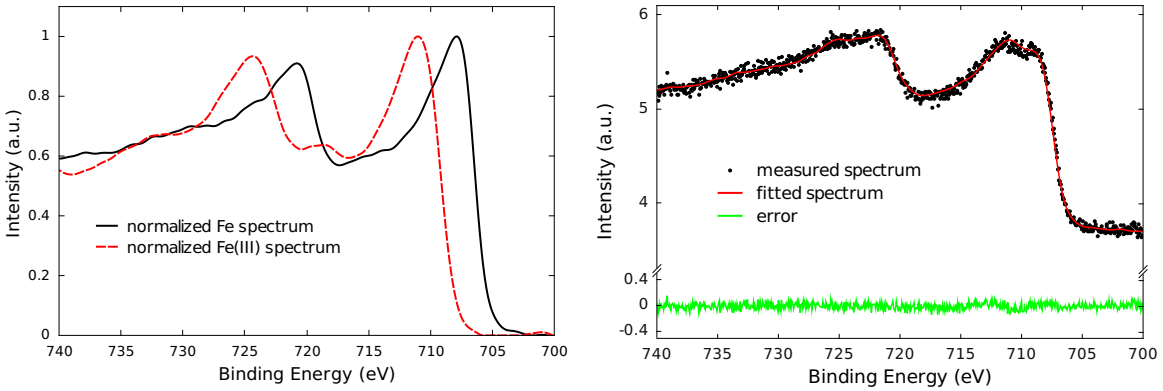

Figure 11: An example of XPS-line fitting using reference spectra. In the left figure the normalized Fe 2p reference spectra of Fe and Fe_2O_3 from bulk samples are shown. The spectra have rather complicated substructure. On the right is the measured Fe 2p spectrum from a partially oxidized FePt thin film. The spectra can be fitted as the superposition of two reference spectra. The relative ratio of oxide to metal is 2.74. The residue of the fitting is shown in the lower subplot.

is not necessarily the intensity described in the model. A typical experimental XPS spectrum is shown in Fig. 10. At the corresponding binding energy the unscattered photoelectrons give raise to a peak profile, whose area is proportional to the signal intensity described in equation (15). The spectrum has a characteristic background which shows higher intensity at the binding energy higher than the peak energy. This change in background height originates from the inelastically scattered electrons. To calculate the area under the peak this background has to be evaluated. Shirley proposed that a smooth background can be defined as the integration of a unknown signal, which is calculated iteratively in a self-consistent manner [85]. On the other hand, the method proposed by Tougaard describes the background by considering the electron energy loss cross section within the material [86], and it is generally regarded as the true background in the XPS spectra. The Shirley background does not consider the real physical process involved in the background formation, and usually will fail when the details of the peak shape need to be resolved. However, if only the relative atomic ratio between the elements is of interest, the Shirley background method usually gives reasonable and reproducible results [87]. In this study, the relative ratio of Fe/Co to Pt is evaluated using the Shirley background method.

In some cases the detailed peak shape in the XPS spectra needs to be considered, especially for transition metal oxides, where the signal from one electron orbit has usually very complicated structure [76]. In this study this happens when the sample are partially oxidized. The Co/Fe 2p signal originates from both the metal and oxide signal overlapping each other. In such case the reference spectra from a bulk metal and metal oxide are measured as reference spectra. The measured signal from the examined sample can be fitted as the weighed superposition of reference signal, as well as a linear background. One of such fitting is illustrated in Fig. 11.

3.3 Quantification of element-specific magnetic moment by XMCD

3.3.1 Introduction to XMCD and the sum rules

The X-ray magnetic circular dichroism is the effect that the absorption of X-rays in a magnetic material depends on the helicity of light and the magnetization direction of the material. A schematic view of the involved process is shown in Fig. 12. When the incoming photon energy matches the energy difference between a core level and Fermi level of the material, a resonant absorption occurs and the electron from the core level is excited to the Fermi level. The absorption cross section depends on the core level states and the empty states above Fermi level. If the incoming X-ray

photon has a defined helicity, the excited electrons are also polarized and carry the spin momentum. In 3d-ferromagnetic materials the density of state (DOS) around Fermi level is asymmetric for spin-up and spin-down electrons, leading to different absorption cross section for different helicity of the photon. The Fermi level in the ferromagnetic material acts as a "spin-detector" for the excited electrons.

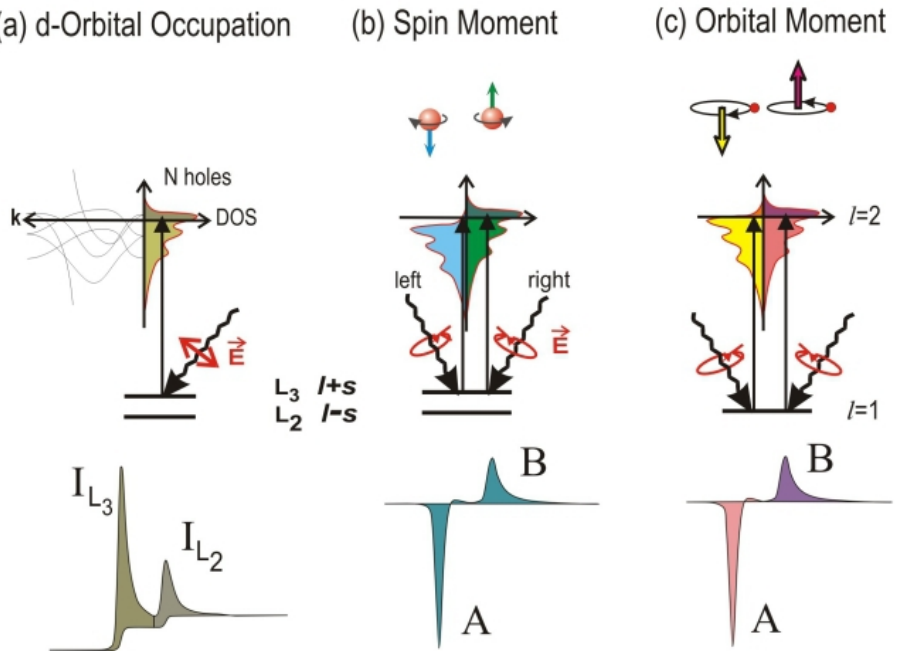

Figure 12: The schematic view of the XMCD process in ferromagnetic materials. When linearly polarized photons are used, the electrons are excited from $2p_{3/2}$ and $2p_{1/2}$ core levels to Fermi level and the absorption is proportional to the d orbit vacancy, shown in (a). When circularly polarized photons are used, due to the asymmetry of the DOS around Fermi level for different electron's spin orientation in ferromagnetic materials, different helicity of the photon leads to different absorption. The difference is shown as A and B at L_3 and L_2 edges, and it is related to the total spin moment of the atom, shown in (b). The difference between A and B is related to the orbital moment of the atom. The figure is adopted from [88].

XMCD has the unique ability to measure the element-specific magnetic moments, as well as the contribution of spin or orbital moments. Theory suggests that for transition metals the difference in the subshell transition cross section can be used to deduce the moment by the so-called *sum rules* [77], which has also been verified experimentally [89]. XMCD sum rules for transition metals can be expressed as:

$$\frac{\Delta A_{L_3} + \Delta A_{L_2}}{3A_t} = \frac{< L_z >}{2n_h} \tag{17}$$

for the orbital moment and

$$\frac{\Delta A_{L_3} - 2\Delta A_{L_2}}{3A_t} = \frac{2 < S_z >}{3n_h} - \frac{7 < T_z >}{3n_h} \tag{18}$$

for the spin moment.ΔA_{L_3} and ΔA_{L_2} are the differences of the transition cross sections at L_3 and L_2 levels between left and right circularly polarized photons, respectively. A_t is the total transition cross section for L_2 and L_3 levels for linearly polarized photons. Usually this can be taken as the average of absorption of left and right circularly polarized photons [89]. Equation (17) reveals the orbital moment $< L_z >$ in units of Bohr magneton (μ_B), while equation (18) calculates the spin moment $< S_z >$ and the magnetic dipole moment $< T_z >$ in μ_B. The spin moment is isotropic, the orbit moment and magnetic dipole moment depend on the symmetry of the crystalline lattice and are usually anisotropic [26]. n_h is the number of holes or empty states in the 3d orbit. Unfortunately, the $< T_z >$ term cannot be determined independently from XMCD measurements but usually are assumed to be small, and the spin moment term obtained by equation (18) is called the effective spin moment $< S_{z,eff} >$. In cubic lattice the theoretical value of $< T_z >$ is nearly vanishing [77], and the $< S_{z,eff} >$ approaches $< S_z >$. In lattices with lower symmetry, especially in FePt system with $L1_0$ structure, the magnetic dipole moment have a significant influence to $< S_{z,eff} >$. Even in material with random distribution of crystalline orientations, the $< T_z >$ does not cancel out [90]. In such systems the influence of $< T_z >$ should always be considered.

The sum rules are derived for atoms and the band structure as well as the transition from 2p to s orbit around the Fermi level is ignored. Moreover, only the dipole transition is considered. The n_h defined above cannot be measured but it is usually delivered by band structure calculations. Although with many limitations, it has been shown that the sum rules work reasonably well for the late transition elements such as Fe, Co and Ni [91, 92, 89].

Since the n_h has to be calculated and cannot be simply measured, the spin and the orbital moment obtained by sum rules might have a systematic error depending on the choice of n_h. However, the ratio between orbit and spin moment is independent of n_h:

$$\frac{< L_z >}{< S_{z,eff} >} = \frac{4(\Delta A_{L_3} + \Delta A_{L_2})}{3(\Delta A_{L_3} - 2\Delta A_{L_2})} \tag{19}$$

Thus, this quantity is a robust measure of the change of orbital moments, such as in FePt in A1 and $L1_0$ crystal structures [93].

3.3.2 Experimental setup and the total electron yield

XMCD measurements are performed with synchrotron radiation, where the photon energy as well as its helicity can be tuned continuously in wide range [94]. To determine the transition cross sections, one can measure the absorption directly by measuring the absorption before and after the X-ray penetrating the sample. The linear absorption coefficient can then be calculated and its change at absorption edge corresponds to the subshell transition cross section. This method, however, needs samples thin enough that X-rays can pass, which means the total thickness should not be larger than about 200 nm. Since the absorption takes place over the complete thickness of the sample, this method gives basically the bulk properties of the material. An alternative method is to measure the relaxation effect after the X-ray absorption. The core level hole created after X-ray photon absorption will relax either by the photon emission (X-ray fluorescence) or electron emission (Auger process). If X-ray fluorescence is measured, the absorption within the penetration depth of the corresponding fluorescence X-rays is detected, which is usually around 100 nm for soft X-rays [79]. In case that the electrons are measured, the process is more complicated. The generated electrons have certain energy distribution, which is similar to the case of XPS. Either the electrons with certain energy (partial yield) or the total electron yield (TEY) is recorded. While photoelectron from both X-ray excitation and primary Auger process exists, the majority of the electron yield arises from the secondary electrons that are generated by the electron inelastic scattering. The energy of such secondary electron is lower than 10 eV and the corresponding penetration depth is below 10 nm (see Fig. 7). When using the TEY method, only the absorption very close to the surface is detected by this method, providing a high surface sensitivity. On the other hand, in element number $Z < 30$ the probability of Auger process exceeds that of X-ray fluorescence [77]. These combined factors suggest that the TEY is the most favorable method for nanoparticles composed of 3d transition metals. In this study only the TEY method is used.

The experimental setup of the TEY method is summarized in Figure 13. The sample is placed facing the incoming polarized X-ray beam. The generated photoelectrons are collected by applying a voltage between the electrically isolated sample and the chamber ground (100 V in this study), so that all the generated photoelectrons will be collected. The photoelectron current is then measured by an electrometer. The typical total current is in pA range. An external magnetic field is applied parallel to the X-rays, in order to switch the sample magnetization. One should notice that since the photoelectrons are continuously extracted from the sample, the sample must be conductive so that the charging due to loss of electrons

can be compensated from the circuit.

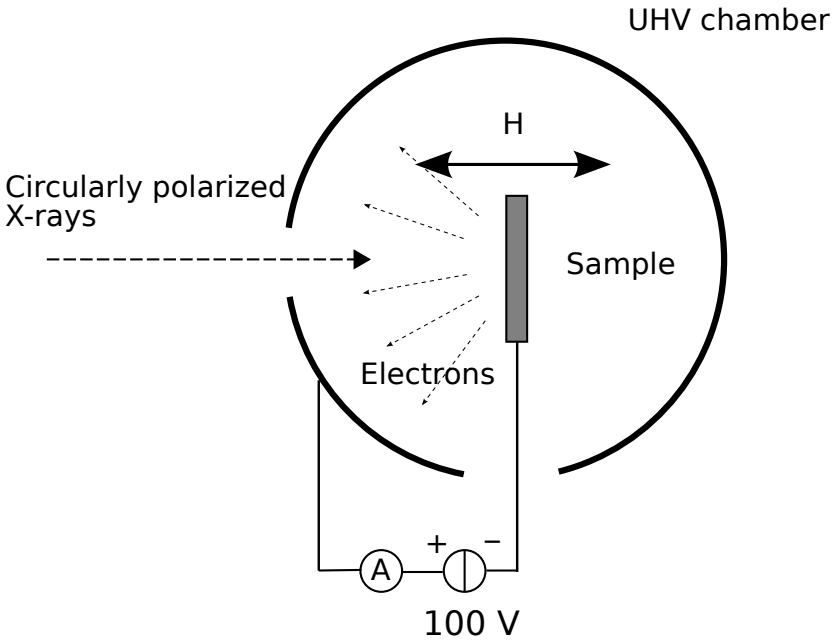

Figure 13: Scheme of the experimental setup for an XMCD measurement based on the TEY method. A high voltage is applied between the sample and the vacuum chamber and the total photoelectron current is measured. The total photoelectron current is proportional to the absorption of the X-rays under certain restriction discussed in Section 3.3.3.

In this study all the measurements are perform at PM-3 bending magnet beamline at BESSY II synchrotron facility in Berlin, Germany using the end station of Prof. Dr. Fauth from Universität Würzburg. The measurement temperature can be adjusted between 11 to 300 K and a bipolar superconducting magnet can supply external magnetic fields up to 3 T.

3.3.3 Saturation effect in the total electron yield method

As discussed above, the photoelectron measured by TEY is proportional to the absorption of X-rays. This proportionality factor, however, depends on the photon energy. The reason can be understood qualitatively as follow: the total electron yield is proportional to the integration of total X-ray absorption within the probing depth, which is determined by the electron penetration depth. When the energy of the incoming photon is changed, its absorption length will also change. Especially around the absorption edge, where the photon energy matches the energy difference between the core level and Fermi level, the absorption will enhance dramatically. In case of Fe the absorption coefficient at L_2 resonance is 3 times the

absorption before the edge [95]. This means that the integrated total absorption within the probing depth will also change dramatically.

Based on this idea, a general model similar to the quantification of XPS signal above can be established. Photoelectrons coming from a unit volume can be expressed as:

$$dI_e = P\,C(\mathbf{r})\,I_x(\mathbf{r})\,\mu_X(\mathbf{r})\,dV \tag{20}$$

The P is a proportional constant between X-ray absorption and the initial photoelectron flux, which is assumed to be a constant for certain material. $C(\mathbf{r})$ is the atomic concentration of the excited element. Since now we are considering a changing X-ray absorption length, the X-ray intensity I_x is position-dependent and the absorption within this volume is $I_x(\mathbf{r})\mu_X(\mathbf{r})$, where μ_X is the absorption coefficient of X-ray, which can be expressed as reciprocal of absorption length $\mu_X = 1/\lambda_X$. The $I_X(\mathbf{r})$ can be expressed as the integration of the absorption factor:

$$I_X(\mathbf{r}) = I_0 \exp\left(\int_\Gamma -\frac{l}{\lambda_X(\mathbf{r}+\mathbf{l})}dl\right) \tag{21}$$

, where I_0 is the intensity of the incoming X-rays and Γ is the path from the volume considered to the sample surface opposite to the direction of X-ray incidence. Unlike in the case of XPS, the generated photoelectrons have a wide energy distribution and all need to be considered. In fact, the major contribution to the photocurrent is due to secondary electrons (SE), which are generated by the Auger cascade process within the sample [76]. A typical photoelectron energy distribution is shown in Fig. 14. It is clear that most of the electrons have energies from 4 - 15 eV, with average value of 7 eV. Other contributions such as the photoelectrons from core levels are, compared to SE, very tiny. The energy of the SE is basically a constant and independent of the material, and as a good approximation it is also generated isotropically [96]. According to the universal curve in Fig. 7, the electron mean free path λ_e can be fixed at 2.5 nm, which is comparable to 2.2 nm measured in Co [97]. Since λ_e is the only material dependent parameter in the model, by assuming it as constant the model discussed here can be applied to any material system.

Unlike XPS, all the electrons reaching the surface of the sample will be collected and measured. Thus, equation (20) has to be integrated across the upper half sphere, namely in the direction where the electrons are escaping the sample surface. This can be expressed as:

$$dI_{TEY} = dI_e G(\mathbf{r}) \tag{22}$$

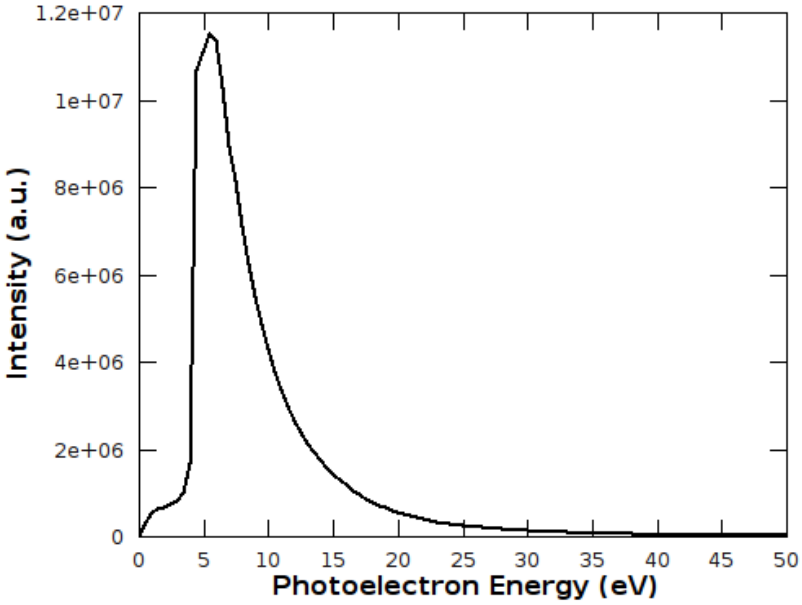

Figure 14: Energy distribution of photoelectron from Au thin film excited by X-ray of Al K_α radiation. Secondary electrons constitute the majority of the total electron yield.

$$G(\mathbf{r}) = \int_0^{2\pi} d\phi \int_0^{\pi/2} d\theta \exp\left(-\frac{s(\theta,\phi,\mathbf{r})}{\lambda_e}\right) \sin\theta \tag{23}$$

Here, $G(\mathbf{r})$ is a factor accounts for the geometry of the sample. The integration of $G(\mathbf{r})$ is expressed in spherical coordinates. $s(\theta,\phi,\mathbf{r})$ is the distance to the surface from position $\mathbf{r}$ at direction angle (θ,ϕ). λ_e is the electron mean free path, assuming as constant. Finally, to get the total TEY signal equation (22) needs to be integrated across the volume of the sample:

$$I_{TEY} = \int_\Omega P\, C(\mathbf{r})\, I_x(\mathbf{r})\, \mu_X(\mathbf{r})\, G(\mathbf{r})\, dV \tag{24}$$

The formulation above is very general and can be applied to any combination of material and geometry. The only assumption made here is a constant electron mean free path in equation (23). Such limitation can be easily lifted by modifying equation (23) to include another integral in radius direction. Applying equation (24) to a homogeneous and planar sample made of a single component, the TEY signal can be expressed as:

$$I_{TEY} \propto 2\left[1 + \frac{\lambda_X}{\lambda_e} \ln\left(\frac{\lambda_X}{\lambda_e + \lambda_X}\right)\right] \tag{25}$$

In limiting case that $\lambda_X \gg \lambda_e$, equation (25) simplifies to $I_{TEY} \propto \lambda_e/\lambda_X$, showing that the TEY signal is just proportional to the X-ray absorption coefficient. If $\lambda_X \ll$

λ_e or the absorption of X-rays is very strong, the TEY signal approaches a constant, i.e. the TEY does not increase although the X-ray absorption is increasing. This is called *saturation* effect. It is essential to correct the saturation effect for TEY method by considering the sample geometry [98].

For nanoparticles the saturation effect of the XMCD spectra also needs to be corrected [96]. Using the model discussed above and consider the geometry of a sphere, a correction factor for TEY can be calculated by:

$$I_{TEY} \propto S(r, \mu_X)\mu_X \tag{26}$$

The correction factor $S(r, \mu_X)$ needs to be calculated numerically. The explicit formula to calculate this factor is given in [99]. In Fig. 15, the correction factor is plotted against μ_X for different nanoparticle diameters. Similar to the planar geometry, the correction term decreases as absorption becomes stronger. The effect in smaller particles is not as pronounced as in large particles. For example in case of 12 nm FePt nanoparticles, the resonance absorption at L_2 edge is about 3 μm^{-1}, and intensity measured by TEY is 85% of the true absorption.

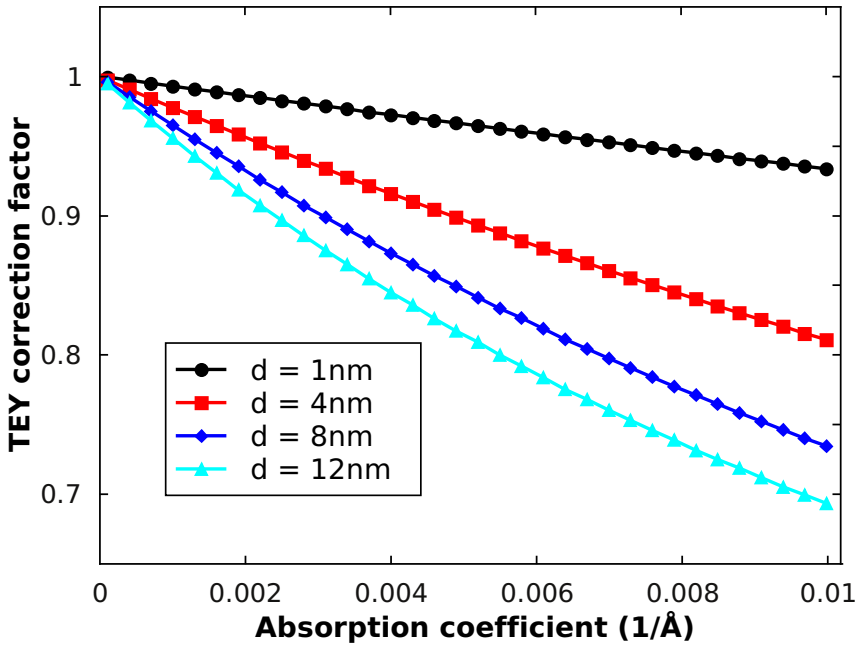

Figure 15: The correction factor for XMCD saturation effect in nanoparticles, calculated for spherical particle with different diameters. The correction is more prominent for larger particles.

3.3.4 Evaluation of XMCD spectra

The raw data in a XMCD measurement has to be properly corrected and normalized to yield the subshell ionization cross-sections, on which the sum rules can be applied. Details of data evaluation process is discussed in this subsection. As an example, measured spectra from 5.6 nm CoPt particles on Si substrate are analyzed step by step. The sample is measured at 300 K, with external magnetic field of +/- 3T. Degree of photon polarization is 92.5%.

The photocurrent from the sample as a function of photon energy is plotted in Fig. 16. In first step the measured photoelectron current needs to be normalized according to the incoming X-ray intensity. A gold grid is used to determine the incoming X-ray intensity, where the TEY from the grid is measured. The TEY current from the sample is divided by the current from the grid to cancel the effect of X-ray intensity variation from the beamline or storage ring itself. The normalized spectrum is shown in the right panel of Fig. 16.

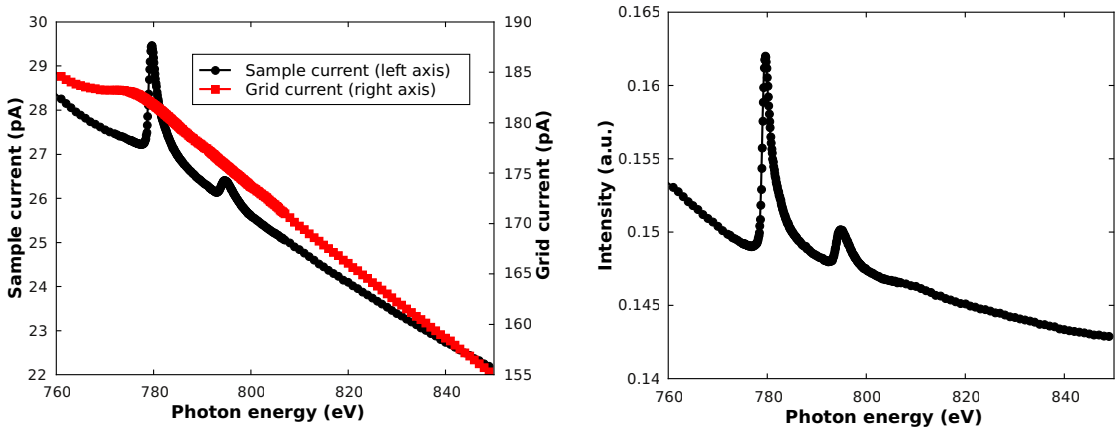

Figure 16: Normalization of the sample current to the grid current. In the left figure both the sample and grid current are shown. The variation of grid current against photon energy is due to the X-ray optics of the beamline. The right figure shows the sample current divided by the grid current.

This normalization procedure is applied to spectra measured in positive and negative magnetic field with respect to the X-ray beam direction (later called plus and minus spectrum). The normalized spectra are shown in left panel of Fig. 17. There is a slight energy shift between plus and minus spectrum, which can be corrected according to the position of the L_2 and L_3 peaks. The vertical offset of two spectra are corrected by taking a linear background which fits the pre-edge (< 770 eV in the sample) and post-edge (> 820 eV) regions. The corrected result is shown in right panel of Fig. 17

The measured spectra shown in Fig. 17 arises not only from the nanoparticles

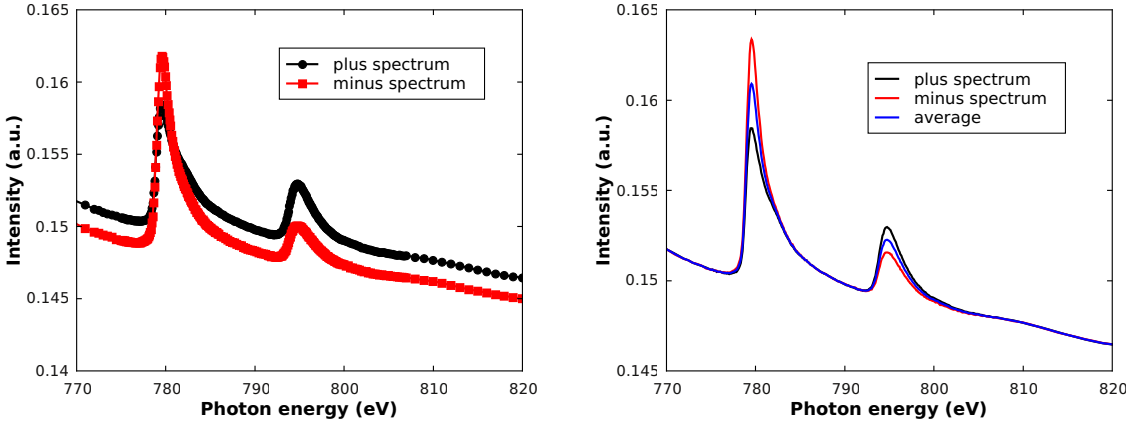

Figure 17: In the left figure the uncorrected plus and minus spectra are shown. There is a linear offset between two spectra, which can be fitted using the data point before L_3 and after L_2 edge. After correction the two spectra fit each other and the average spectrum of plus and minus can be calculated, as shown in the right panel.

but also from the Si substrate. This contribution can be fitted by a polynomial in the measured energy range. Additionally, a two-step function is introduced to describe the increase of absorption in the particles after the L_2 and L_3 edge. The total background can be expressed as:

$$B(E) = h\left[\frac{\tanh(\frac{E-E_{L_3}}{w})-1}{3} + \frac{\tanh(\frac{E-E_{L_2}}{w})-1}{6}\right] + a_0 + a_1E + a_2E^2 + a_3E^3... \quad (27)$$

The first term in equation (27) describes the resonant absorption at $L_{2,3}$ edges, i.e. from the particles. It contains only one fitting parameter h describing the total increase of the absorption. The width of the step w and step postion E_{L_2}, E_{L_3} are defined according to the spectrum. The polynomial terms in equation (27) account for the contribution of Si substrate. Since the background is not expected to show any dichroism, identical background can be used for both plus and minus spectra. This procedure is shown in Fig. 18.

The corrected spectra in Fig. 18 are related to the real absorption spectra by the following relation:

$$I(E) = A \cdot \mu(E) \cdot S(r, \mu(E)) + B \quad (28)$$

Here, $I(E)$ is the corrected spectrum shown in Fig. 18, and $\mu(E)$ is the real absorption spectrum. S is the correction factor introduced in equation (23) and shown

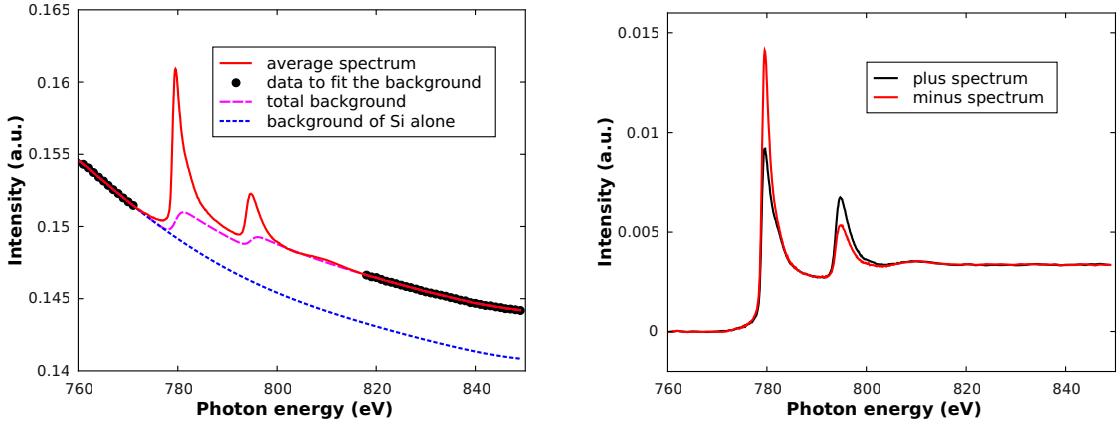

Figure 18: Background fitting of the XMCD measurement. The average spectrum obtained in Fig. 17 is used to fit the background as shown in the left figure. By subtracting the background the plus and minus spectra are shown in the right figure.

in Fig. 15. A and B are just normalization factors. The reference absorption coefficient μ before and after the absorption edges can be obtained from NIST X-ray Attenuation Databases [79] and their corresponding S can also be calculated. With the help of these two reference points the normalization factors A and B can be determined. Afterwards, $\mu(E)$ can be calculated numerically.

The sum rules in equations (17) and (18) can then be applied to the corrected spectra. The total transition cross section is obtained by integrating the average of plus and minus spectra and considering the two-step background defined in equation (27). ΔA_{L_2} and ΔA_{L_3} can be obtained by integrating the difference of plus and minus spectra. The procedure is illustrated in Fig. 19 and 20.

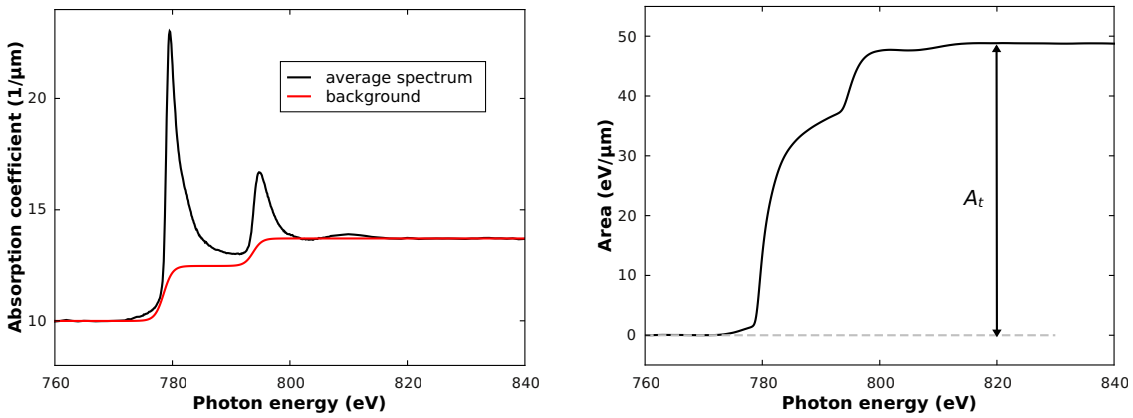

Figure 19: X-ray absorption spectrum and its background (left). The integration of the area under the peak gives the curve shown on the right. The total height of the curve is measured as the A_t in the sum rule.

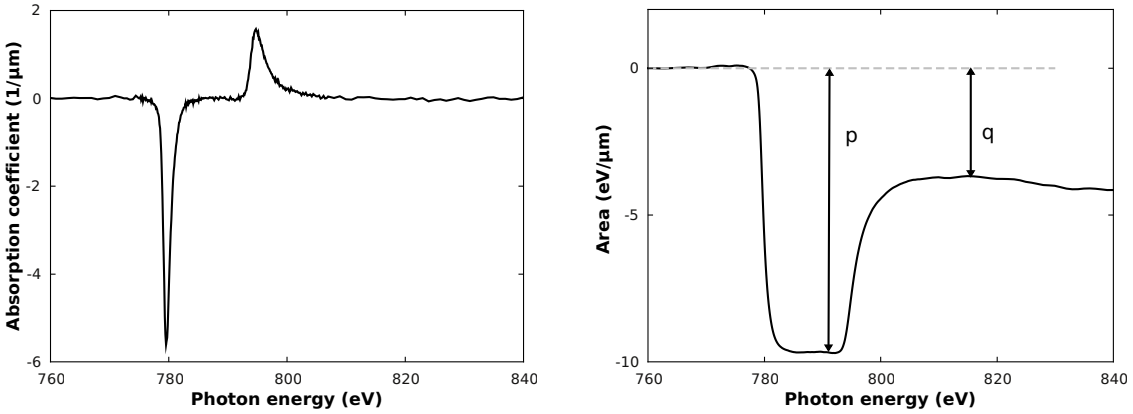

Figure 20: XMCD spectrum (left) and its integration (right). By definition $p = \Delta A_{L_3}$, $q = \Delta A_{L_3} + \Delta A_{L_2}$.

For practical reasons, the parameters p and q are defined according to Fig. 20. The sum rules can then be rewritten as:

$$< L_z >= \frac{n_h}{\sigma} \frac{2q}{3A_t} \tag{29}$$

$$< S_{z,eff} >= \frac{n_h}{\sigma} \frac{3p - 2q}{A_t} \tag{30}$$

The formula above also take correction for the degree of photon polarization σ.

The procedure described here is slightly different from what is commonly used in literature, where the sum-rules are applied to spectra measured by TEY without saturation correction, but the obtained moments are then corrected by certain factors, which are calculated using the reference absorption spectra of the same material in a thin film or bulk sample [96, 99]. Both procedures are equivalent. However, the procedure described here does not need extra reference. This can be useful in case that the measured element is in a complicated chemical environment, such as partially oxidized state, where the absorption spectra could have rather complicated structure and extra reference spectra are usually not feasible.

4 Morphological, chemical and structural characterization of FePt and CoPt nanoparticles

The magnetic properties of FePt and CoPt nanoparticles are closely related to its crystalline structure, microscopic morphology and chemical state. Before discussing the detailed magnetic properties, the morphology and chemical state of the particles should be clearly defined and their structure investigated. In this section the sample preparation method will be summarized in detail. The achievement of the sample preparation will be investigated by SEM, AFM, XPS and HRTEM, so that well-defined FePt/CoPt nanoparticle systems are established, on which their oxidation and magnetic properties can be discussed in the following sections.

4.1 Sample preparation

All the nanoparticles in this study are prepared by the reverse micelles (discussed in Section 2.1). 25 mg of PS-b-P2VP or PS-b-P4VP diblock co-polymer is dissolved in 5 ml of toluene. The polymers are commercially available from Polymer Source Inc., Canada. Afterwards Zeise's salt ($K[Pt(C_2H_4)Cl_3] \cdot H_2O$, Aldrich) is loaded as the Pt precursor. The solution is stirred continuously for a few days till complete dissolving of Pt precursor, after which the Fe (iron(III) chloride, 99.99%, Alfa Aesar) or Co (cobalt(II) chloride, 99.999%, Alfa Aesar) precursors can be added. The stirring continues till all the precursors are completely dissolved. The amount of precursor is chosen such that the atomic ratio between all metal ions of precursor and all the pyridine units of polymer is 1:2. The relative atomic ratio of Pt to Fe/Co precursor is set to 1:1. After complete dissolving of the precursor, the solution is filtered successively with filters of 1µm, 0.45 µm and 0.2 µm pore sizes (CHROMAFIL®, apolar). The micelles in the solution can then be deposited on substrates.

The micelles are deposited using dip-coating by a home-made linear stage. The substrate is emerged in the solution and pulled out perpendicularly to the liquid surface. Substrates are usually 10x5 mm Si with natural SiO_x on surface. The pulling speed will influence the interparticle distance [12]. In this study the speed is fixed at 15 mm/min.

The Si substrate deposited with micelles are loaded into a custom-build plasma etcher. An oxygen plasma treatment (frequency 13.56 MHz, operating pressure $4{\cdot}10^{-2}$ mbar, power 50 W resulting in a dc self-bias of –500 V with the sample holder grounded) is applied for 30 min. while the sample temperature is raised up to 250 °C or 300 °C for smaller and larger micelles, respectively. The polymer is

completely removed by the plasma treatment and the precursor loaded in the core of the micelles are transformed into metal oxide nanoparticles [11]. The sample is then exposed to a hydrogen plasma for 20 min. to reduced the nanoparticles into the metallic state. The condition of the hydrogen plasma is identical with oxygen plasma except the plasma is maintained at 0.1 mbar.

As discussed in Section 2.4, the particles after hydrogen plasma is in chemically disordered state. To transform the particles into partially $L1_0$ ordered state, different annealing steps are applied in the plasma chamber. The annealing is applied with background hydrogen gas at $1 \cdot 10^{-3}$ mbar. After annealing the sample is cooled down within a hydrogen plasma.

4.2 Morphology and chemical state

Magnetic properties of nanoparticles are strongly influenced by its chemical state [100]. In case of FePt nanoparticles, the presence of oxide will greatly influence the formation of chemical order and deteriorate the desired high magnetic anisotropy [101]. Before any further investigation, the chemical state of nanoparticles needs to be characterized. XPS spectra of deposited micelles loaded with Fe and Pt precursors after oxygen plasma and hydrogen plasma are presented in Fig. 21. After oxygen plasma (as discussed in Section 4.1), at the Fe $2p_{3/2}$ only the Fe^{3+} signal at 711.5 eV can be identified, indicating the Fe atoms are completely oxidized. At Pt 4f the $4f_{7/2}$ peak of PtO or Pt_2O is clearly visible. The exact oxidation state, however, cannot be clearly distinguished. Since Pt oxide is unstable against heating [102], heating up to 300 °C during the oxygen plasma decompose certain portion of the Pt oxide. As a result small shoulder at metallic Pt position can be found in the spectrum. After hydrogen plasma treatment, both Fe and Pt shows purely metallic signal. The reduction with hydrogen plasma is proven to be very effective.

Typical SEM images of FePt nanoparticles prepared by different polymers are presented in Fig. 22 and details are summarized in Table 3. The SEM image is taken after the oxygen plasma and the particles are expected to be oxidized. The size of the particle is determined by AFM after the particles are reduced by hydrogen plasma. After oxygen plasma, the Fe and Pt precursors in the core of the micelle are fully transformed into single particles. The nanoparticles form a homogeneous cover on the surface thanks to the dip-coating process. The particles show a near range hexagonal arrangement, but long range order is disrupted. Overall, the arrangement of particles on the substrate is isotropic in long range. Under the same dip-coating condition, the interparticle distance is mainly determined by the polymer. The PS(266)-P2VP(41) give very similar interparticle distance of 30 and 28 nm

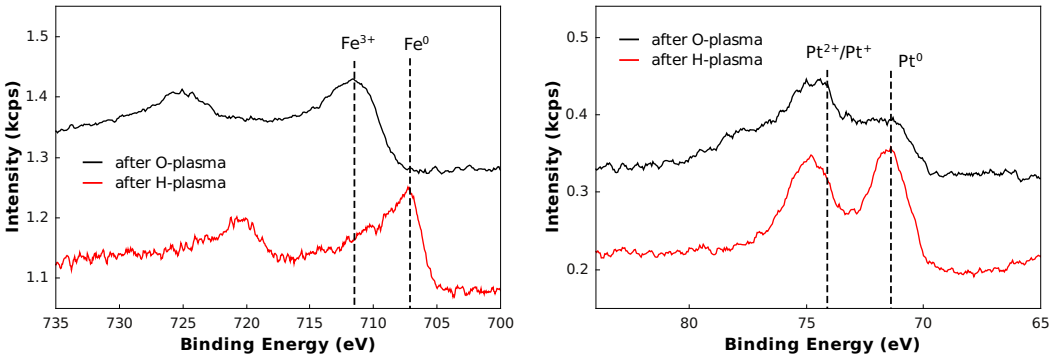

Figure 21: XPS spectra at Fe 2p and Pt 4f for deposited micelles loaded with Fe and Pt precursors after oxygen plasma treatment and after hydrogen plasma treatment. Both Fe and Pt are purely metallic after hydrogen plasma treatment. The spectra are smoothed with 5-point moving averaging. The peak positions for Fe $2p_{3/2}$ and Pt $4f_{7/2}$ in metallic and oxidized states are marked in the diagrams.

for 2.6 and 4.5 nm particles, respectively. Larger polymer PS(1779)-P2VP(685) gives much larger interparticle distance of 61 nm, and also larger particle sizes of 9.4 nm. It is remarkable that the 2.6 and 4.5 nm particles are prepared with the same polymer. This effect is ascribed to the slightly different ambient condition during micelle formation. It is well known that change in temperature will influence the morphology of micelle dramatically [25]. Moreover, high humidity in air may cause water entering the micelle cores [12], resulting larger nanoparticle sizes. The compositions shown in Table 3 are determined by XPS after the particles are reduced in hydrogen plasma. All compositions are within the range where the $L1_0$ order is possible according to the phase diagram in Fig. 3. The slight deviation of concentration from 50:50 is mainly due to the inaccuracy of weighing the precursors. Since the $FeCl_3$ salt is extremely hygroscopic, weighing in ambient atmosphere tends to give less Fe amount than desired.

Table 3: Polymer used, interparticle distance, size and composition of nanoparticles shown in Fig. 22. The polymer is expressed as PS to P2VP monomer ratio. The composition is determined by XPS after oxygen and hydrogen plasma etching.

Polymer PS-P2VP	Distance (nm)	Diameter (nm)	Composition (Fe:Pt)
266:41	30±5	2.6±0.7	48:52
266:41	28±6	4.5±1.3	44:56
1779:685	61±12	9.4±1.3	44:56

In order to transform the nanoparticles at least partially into $L1_0$ phase, annealing up to 600 °C is required. A major problem occurred for colloidal nanoparticles is that the high annealing temperature will cause agglomeration of the nanoparticles,

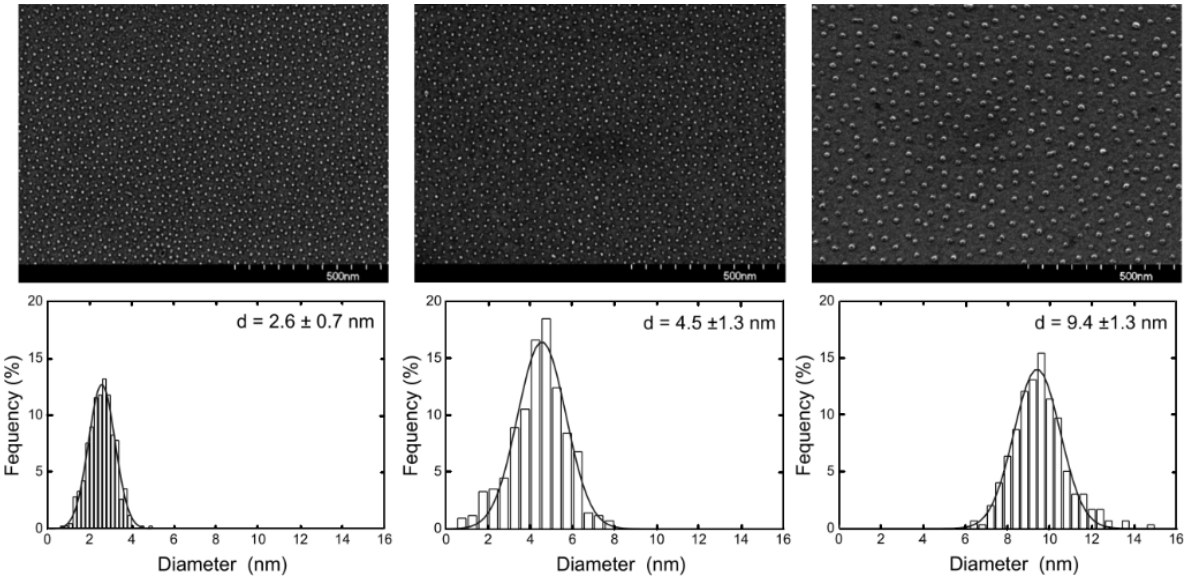

Figure 22: SEM micrographs of FePt nanoparticles with 2.6 nm, 4.5 nm, and 9.4 nm diameter and their corresponding size distribution as measured by AFM. Details are given in the text. Figures adopted from [12].

and the ordered array is thus destroyed [6]. This problem is avoided in nanoparticles prepared by the micellar method. SEM images of 9.8 nm nanoparticles just after oxygen plasma and after reduction and annealing at 700 °C for 30 min. are shown in Fig. 23. The array of the particles are preserved after annealing, which is mainly due to the relative large interparticle distances with respect to particle sizes. Due to the oxide formation, the particle size just after oxygen plasma is slightly larger than after annealing under SEM.

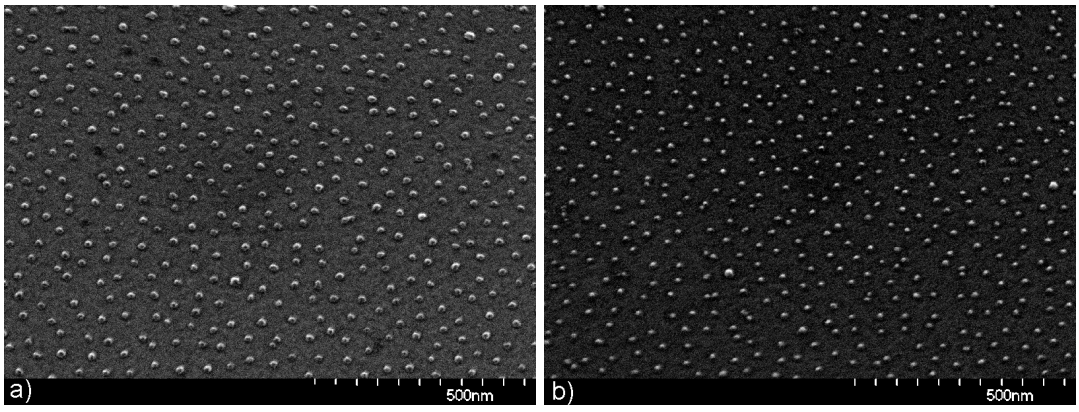

Figure 23: SEM micrographs of 9.4 nm FePt nanoparticles after oxygen plasma (a) and after reduction and annealing up to 700 °C for 30 min. Images adopted from [103].

The SEM image of CoPt nanoparticles shown in Fig. 24 resembles the results obtained for FePt. The SEM image is obtained after particles are formed by oxy-

gen plasma, and AFM size distribution is obtained after particles are reduced by hydrogen plasma. The applied polymer is PS(1779)-P2VP(685), yielding 55 nm interparticle distance, which is comparable to 61 nm obtained with the same polymer for FePt. The particle size of 5.6 nm, however, is smaller than that 9.4 nm of FePt.

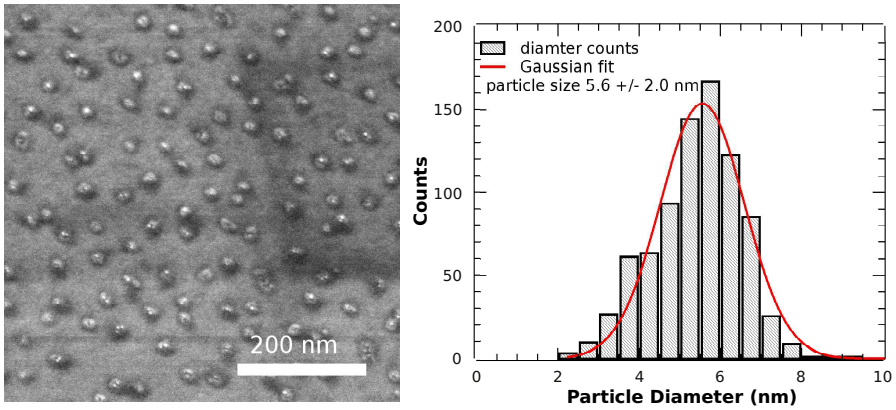

Figure 24: SEM micrograph of CoPt nanoparticles (left) and the corresponding size distribution measured by AFM (right).

4.3 Structure of FePt nanoparticles

The magnetic properties of FePt system is closely related to its crystalline structure. Due to the limitations discussed in Section 3.1, the TEM investigation is most reliable way to probe the crystalline structure of FePt nanoparticles. Example of HRTEM images of 3 nm FePt nanoparticles after annealing are shown in Fig. 25. The particles are annealed at 650 °C for 30 min. In Fig. 25(a), the $L1_0$ order is identified from the alternating atomic layers along the [001] direction. The insert shows the Fourier transform of the nanoparticle image, confirming the presence of 001 superstructure. The particle is also nearly spherical and contains no visible defects. Similar alternating atomic layers are visible In Fig. 25(b), but in the right half of the particle the crystalline orientation is misaligned, possibly due to the presence of twining boundary within the particle.

According to HRTEM image simulation, the alternating contrast along [001] direction in FePt nanoparticles has rather complicated relation with degree of order S, and HRTEM imaging cannot be used to quantify of S accurately [72]. Nevertheless, the simulation suggests that in 5 nm FePt nanoparticle, clear 001 superstructure is only visible with $S > 0.56$. This suggests that the nanoparticles shown in Fig. 25 tend to have relatively high degree of order.

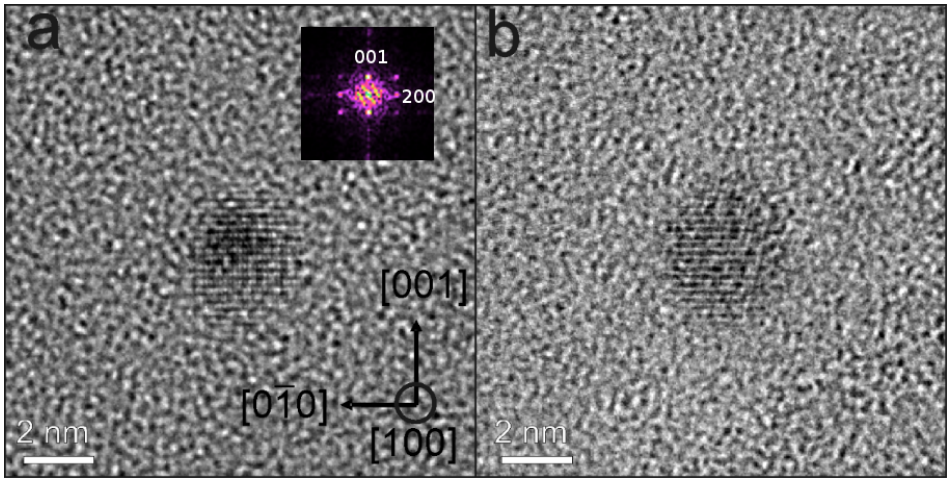

Figure 25: HRTEM images of 3 nm FePt nanoparticles after annealing at 650°C for 90 min. The images are taken along the [100] direction. The insert in (a) is Fourier transform of the particle image. The superstructure is clearly visible. The chemical ordering can also be identified in HRTEM image along the [001] direction from the alternative atomic layers. Images are taken from [12].

Due to the limit of microscopic methods, only a small number of particles can be investigated by TEM. On the other hand, the 001 superstructure is only visible along 001 direction. Since the crystalline orientations of the particles are random, only a small fraction of the particles lies in the specific direction where the chemical order can be identified. The HRTEM shown in Fig. 25 proves the existence of $L1_0$ chemical order in some FePt nanoparticles, but a statistics among many particles is still missing.

Defects within the nanoparticles are more clearly visible in 8 nm FePt particles shown in Fig. 26. The images are taken along the [101] direction, thus the $L1_0$ superstructure as well as the alternating atomic layers are not visible and chemical order cannot be distinguished. While the particle shown in Fig. 26(a) contains no defects, stacking faults and twin boundaries are clearly visible in particles in Fig. 26(b,c).

A statistical analysis of in total 70 nanoparticles (3 nm) shows that 38 FePt NPs exhibit defects along the [101] direction. From this result and the fact that additional defects may exist which cannot be seen in the [101] projection, it can be concluded that for the majority of particles crystal defects are a common feature. For 8 nm FePt NPs defect-free NPs are rare [12]. The presence of defects in nanoparticles may have large influence to its magnetic properties. Nanoparticles such as shown in Fig. 26.(b,c) are divided into small regions with different crystalline orientation and thus different easy axis orientation of the magnetization. On the other hand, all the magnetic moments within the particle are pointing to the same direction, as the particle size is well below the critical size of single domained particle. The

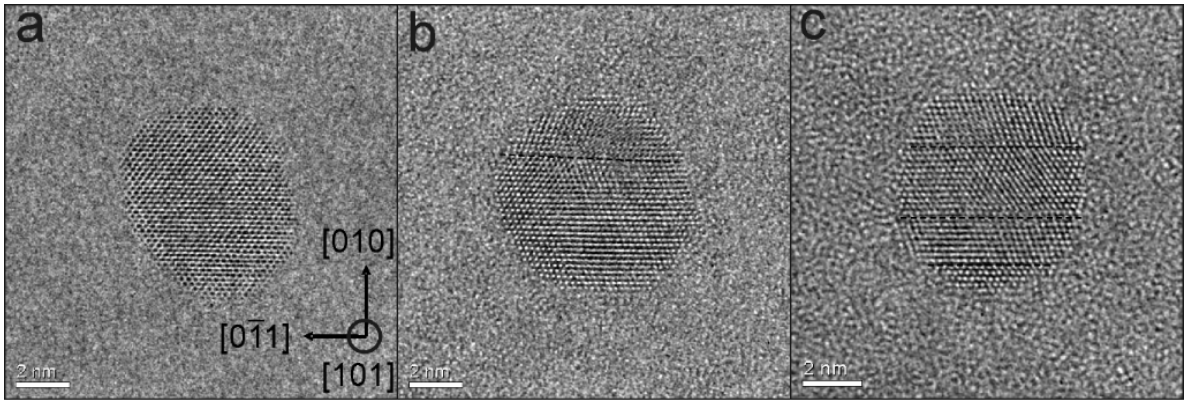

Figure 26: HRTEM images of 8 nm FePt particles along [101] direction. Crystalline defects such as twining and stacking faults can be identified, shown as dashed lines in (b,c). Images are taken from [12].

total anisotropy energy experienced by the particle is the averaged effect of different magnetocrystalline anisotropy terms originated from each small regions. The total effective anisotropy energy can be very low, even when the chemical order in each small region is high. As a result, the presence of the defects reduces the effective anisotropy energy density within the particle.

5 Oxidation of FePt nanoparticles and the effect of surface segregation

Similar to other nanoparticles composed of transition metals, FePt and CoPt nanoparticles will oxidize when exposed to air [101], which will deteriorate or destroy their desired magnetic properties. In this section the details on the oxidation of FePt nanoparticles will be discussed [104]. Especially, the initial oxidation behavior of FePt nanoparticles from the metallic state is investigated as functions of particle size. It is found that after annealing the oxidation is greatly hindered in FePt nanoparticles. Also the apparent Pt to Fe signal increases after annealing, suggesting a possible surface segregation of Pt. This surface segregation might be responsible for the change of oxidation behavior.

5.1 Experimental details

FePt and CoPt nanoparticles of different sizes are prepared by reverse micelles as discussed in Section 4.1. The parameters of different nanoparticles used in the study of oxidation are summarized in Table 4. The particle size is measured by AFM, and the composition is determined using XPS. For all the samples the composition lies within the possible range of $L1_0$ phase formation. As a reference for oxidation experiments, a 50 nm thick FePt film was prepared on top of a MgO(001) substrate at room temperature by pulsed laser deposition. The as-prepared film is found in the chemically disordered state (A1 structure) and shows (001)FePt‖(001)MgO; [100]FePt‖[100]MgO cube on cube epitaxy as proven by x-ray diffraction [54].

Table 4: Summary of the nanoparticle samples investigated in the oxidation experiments. All particle's compositions are found around equiatomic. The size distributions are quite narrow, thus size dependent effects can be investigated. As a reference a FePt thin film is also examined.

Name	Used polymer	Diameter (nm)	Composition (Fe/Co:Pt)
FePt NP	PS(1192)-b-P4VP(400)	11.5±2.3	53:47
FePt NP	PS(1788)-b-P2VP(857)	9.8±0.6	53:47
FePt NP	PS(528)-b-P2VP(177)	4.9±0.7	51:49
FePt thin film	-	50 (thickness)	50:50

After 15 min. hydrogen plasma reduction at 250 °C the nanoparticles are in chemically disordered A1 state [11]. Nanoparticles are then subjected to successive molecular oxygen exposure, and XPS spectra of Fe 2p and Pt 4f levels are measured in-situ after each exposure step. For oxygen doses below 10^{11} Langmuir (L), molec-

ular oxygen is used, while for higher oxygen doses the samples are exposed to the ambient atmosphere. After one complete series of oxidation steps the samples are reduced by hydrogen plasma and annealed at 650 °C for 90 min at 10^{-3} mbar hydrogen atmosphere. During this step FePt nanoparticles partially transform into the chemically ordered $L1_0$ state [11]. Identical oxidation steps are then applied to these annealed samples and the oxidation behavior is compared to the as-prepared state.

To quantify the degree of oxidation, measured spectra of Fe are fitted using the method shown in Fig. 11, where the relative signal intensity of Fe^0 to Fe^{3+} is extracted. The possible surface segregation of Pt is quantified with a core-shell model of XPS shown in Fig. 30, where the change of Fe-to-Pt intensity ratio can be related to the thickness of Pt shell.

5.2 Oxidation of FePt nanoparticles

As a first step, the changes of the chemical state in the nanoparticles by oxidation should be understood. XPS spectra of FePt nanoparticles before and after the oxygen exposure are shown in Fig. 27. The Pt 4f and Fe 2p spectra are measured on 11.5 nm FePt nanoparticles in the reduced state and after exposure to ambient air for 24 h. In the reduced state a fully metallic signal is observed for both Fe and Pt, which confirms that the hydrogen plasma treatment is able to completely reduce the nanoparticles, providing a defined initial state for the following oxidation steps. The exposure to ambient condition causes clearly a shift of Fe $2p_{3/2}$ peak to about 711 eV, while at the metal position (707 eV) only a small shoulder can be observed, indicating the formation of iron oxide in Fe^{3+} state [105], where both Fe_2O_3 and Fe_3O_4 are possibly formed [106]. Due to insufficient signal to noise ratio in this measurement, the exact phase of the iron oxide cannot be distinguished from fine structures of the XPS spectra. Contrary to Fe, the spectrum at Pt 4f peaks reveal no significant change. Both, before and after the oxygen exposure, the Pt $4f_{7/2}$ remains at 72 eV, indicating the metallic state of Pt is unchanged. This finding is quite astonishing, since even bulk Pt will form a thin layer of oxide when exposed to oxygen [102]. In case of FePt, however, the Fe acts as the reduction agent for oxide of Pt. This behavior is very similar to the case of sacrifice anode in electrochemistry, where one metal connected to another less noble metal will be protected against corrosion, and oxidation only occurs on the other metal. Such behavior has also been observed for alloy systems in a single phase such as FeCr [107].

To track the development of oxidation with successive oxygen exposure, the relative ratio of Fe^{3+} to Fe^0 is determined for each exposure step. Note that in

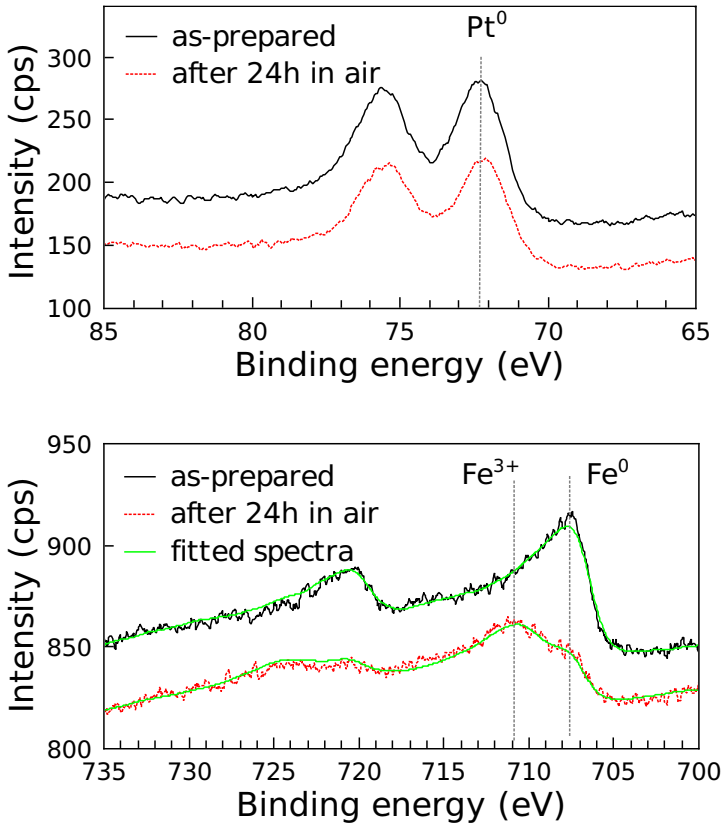

Figure 27: Pt 4f and Fe 2p XPS spectra of 11.5 nm FePt particles before and after exposure to ambient air for 24 h. After the exposure majority of Fe signal is from the Fe^{3+} state, while Pt atoms remain metallic. All spectra are smoothed by three-point moving window averaging. The spectra are vertically off-set for clarity and no further normalization is performed. Solid green lines in lower panel are fits based on Fe^0 and Fe^{3+} reference spectra as shown in Fig. 11. The figure is adopted from [104].

case of metal nanoparticles, the oxidation usually starts at the surface [100], which has also been shown for FePt nanoparticles [55]. Since XPS has probing depth of only few nanometers, the contribution to the oxide signal might arise from the thin surface oxide, and the remaining metallic signal is from the core of nanoparticles. As a consequence, the ratio of Fe^{3+} to Fe^0 determined here is not necessarily the portion of the Fe atoms that are oxidized. Assuming the oxidation initiates from the surface, the same Fe^{3+} to Fe^0 ratio for larger nanoparticles corresponds to a lower Fe^{3+} content compared to smaller nanoparticles. A quantitative measure between the experimental ratio and the actual oxidized portion can be established if the spherical geometry of the nanoparticles is taken into account [104].

The result of successive oxidation for differently sized FePt nanoparticles as

well as the reference film is presented in Fig. 28. For the thin film sample in the as-prepared metallic fcc state a minimum dose of molecular oxygen of 10^8 L is necessary to observe a Fe^{3+} signal above the detection limit. For higher exposures the ratio of Fe^{3+} to Fe^0 changes logarithmically. In the partially $L1_0$ ordered state of the film, however, as obtained after annealing, pure molecular oxygen does not lead to significant formation of Fe oxides. In that case, exposure to ambient air is necessary to increase the Fe oxide-to-metal ratio to detectable range. It is possible that the humidity presented in ambient condition plays a significant role in the oxidation of chemically ordered film.

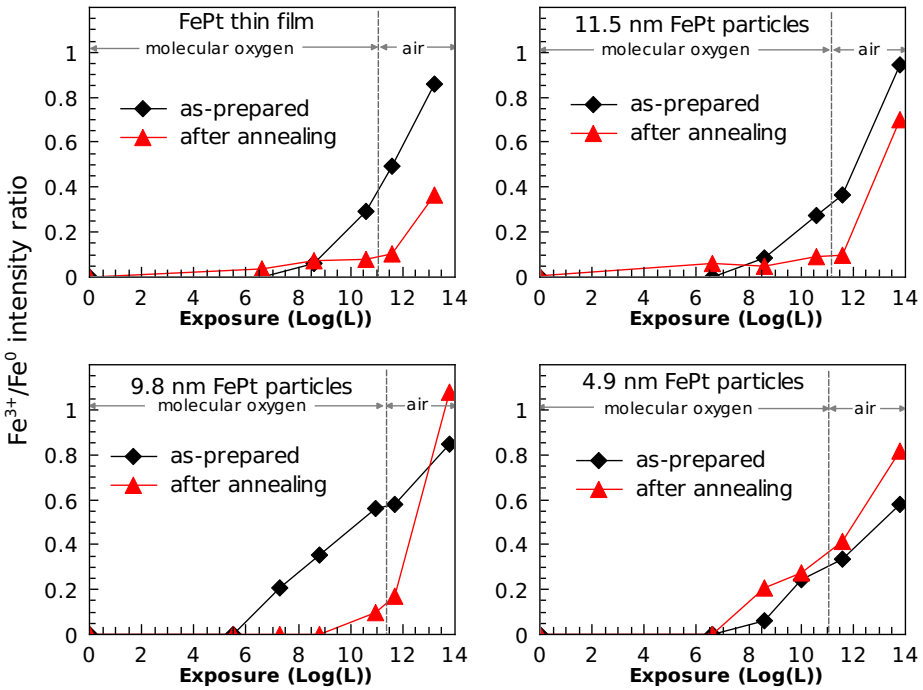

Figure 28: Oxidation experiments of differently sized FePt nanoparticles and FePt thin film before and after annealing at 650 °C for 90 min. The relative ratio of Fe^{3+} to Fe^0 as obtained by fitting XPS spectra is plotted against the exposure in Langmuir (L). Due to the reduced signal to noise ratio in the spectra, the relative error in the ratio is 10% for NP samples. For exposure larger than 10^{11} L the sample is directly exposed to ambient air, which is shown as dashed line in the plot. Figure adopted from [104].

Similar oxidation behavior is also observed for 11.5 nm and 9.8 nm FePt particles. In both cases the as-prepared nanoparticles show detectable oxidation above 10^8 L, and the annealed nanoparticles start to oxidize only after exposure of 10^{10} L. Compared to other metallic nanoparticles such as Fe and Co [100], the FePt system is relatively inert. Annealing leads to further enhanced resistance to oxidation, and the partially ordered FePt nanoparticles can withstand 100-1000 longer oxygen

exposure compared to the as-prepared nanoparticles. After the nanoparticles are exposed to air, both the as-prepared and annealed samples show the same rate of oxidation. A completely different oxidation behavior is observed for the 4.9 nm FePt nanoparticles. Within the experimental error, the onset of oxidation occurs equally at around 10^6 L for as-prepared and annealed sample, and the rate of oxidation afterwards is identical within the error bar.

Although NP of smallest size shows significant different oxidation behavior compared to larger nanoparticles after annealing, it has been shown that for all the nanoparticles the low temperature coercivity increases after annealing, indicating the partial formation of $L1_0$ phase [12]. As a consequence, the increased resistance to oxidation after annealing in FePt thin film and larger particles cannot be ascribed solely to the chemical order. Rather, the inertness of FePt system after annealing might be due to the surface segregation of Pt. This effect is investigated in the next subsection.

5.3 Surface segregation of Pt

Several theoretical studies have focused on the order–disorder transition in FePt nanoparticles due to annealing, and suggest that Pt segregation towards the particle surface is likely: A Monte Carlo approach with an Ising-type Hamiltonian revealed a strong tendency for Pt segregation on (001) facets and a less pronounced tendency on (111) facets of any excess amount of Pt in the particles [43]. At equiatomic composition another Monte Carlo simulation [108] has shown that Pt segregation is likely even before reaching the typical annealing temperatures used in experiments (600–800 °C). Ab initio calculations assuming pure Fe(001) or Pt(001) facets in FePt cuboctahedra containing 561 atoms yielded a strong, scalable energy difference of 44 meV/atom in favor of Pt(001) facets [66].

Experimentally, the effect of Pt segregation in FePt nanoparticles has been observed indirectly by HRTEM, where icosahedral FePt nanoparticles show increased lattice constants towards the particle surface, suggesting a gradual enrichment of Pt towards the surface [70]. Also these icosahedral FePt nanoparticles are quite inert to oxidation. In this thesis, the elemental specific XPS measurement is performed to investigate the segregation of Pt towards nanoparticle surface.

The relative intensity of Fe to Pt is measured before and after the formation of partial chemical order. Result of one of such measurement on 9.8 nm nanoparticles is shown in Fig. 29. Fe 2p and Pt 4f spectra are measured before and after annealing without any oxygen exposure. The spectra are normalized such that for both cases the area under the Pt 4f doublet peaks is identical. In Fig. 29 it is clearly shown that

the normalized Fe signal decreased drastically to about 40% after annealing. If the Fe and Pt atoms in the particles stay homogeneous, the composition of the nanoparticles would shift from $Fe_{53}Pt_{47}$ to $Fe_{31}Pt_{69}$. Such composition change would forbid the formation of $L1_0$ chemical ordering. However, in Section 6 the measured magnetic properties on these nanoparticles clearly prove that partial chemical order after such annealing steps is achieved. Thus, the apparent composition change observed here cannot be explained by a loss of Fe atoms. Rather, a core-shell model with FePt core and segregated Pt shell needs to be introduced to explain the apparent composition change in XPS.

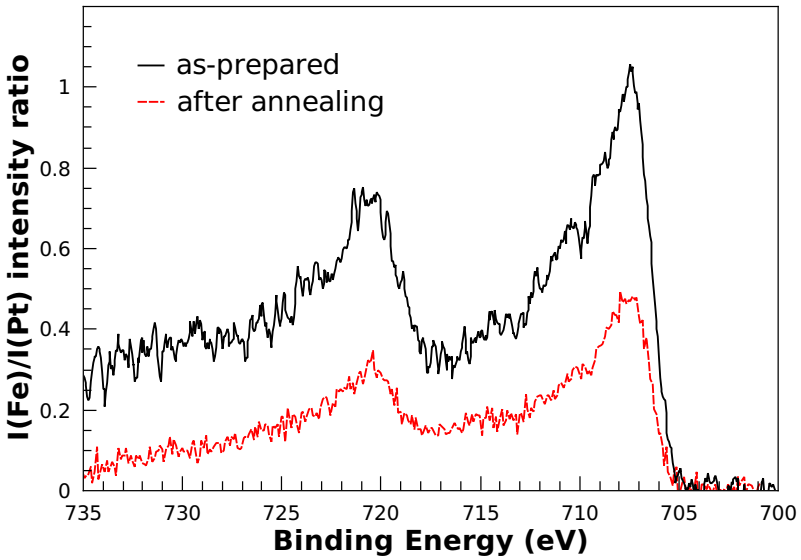

Figure 29: Intensity of Fe 2p normalized to the Pt 4f intensity for 9.8 nm FePt nanoparticles in the metallic as-prepared state and after annealing to 650 °C for 90 min. The significant decrease of Fe intensity indicates the segregation of Pt atoms towards the surface.

The core-shell model is established according to procedures described in Fig. 8 of Section 3.2.2, with FePt core and Pt shell. Such model assumes that a distinct boundary is formed separating Pt shell and FePt core, which is usually not realistic in nanometer scale. As it is suggested by HRTEM result [70], probably the Pt concentration increases gradually towards the surface. Thus, the core-shell model is a simplification of the real situation and the Pt layer thickness should be understood as an effective segregation effect. Furthermore, the composition of the core is assumed to be $Fe_{50}Pt_{50}$. In reality prepared particles always have slight variation from 50:50 composition, and even for FePt particles in equiatomic composition, by forming a thin layer of Pt the core will shift to Fe rich. Thus the assumption for the composition is sound only when the Fe:Pt ratio is close to 50:50 and the Pt

segregation layer is thin.

Based on the predictive formula by Gries [82], the following IMFP values were chosen: within the FePt core a value of 1.1 nm is attributed to the Fe 2p and of 1.7 nm to the Pt 4f photoelectrons, while the corresponding values in the pure Pt shell are 1.05 nm and 1.62 nm, respectively. Similarly to Fig. 9, a relation between the apparent Fe intensity change and Pt layer thickness can be established. Here, the Pt layer thickness is taken as a constant and the intensity ratio of Fe to Pt is calculated for different particle diameters. This ratio is then normalized to the same ratio calculated for a homogeneous FePt particle, i.e. Pt layer thickness of 0. Such normalized ratio is then equivalent to the relative decrease of the normalized Fe signal obtained experimentally. Dependence of such normalized ratio to particle diameter is presented in Fig. 30. Three different Pt shell thicknesses of 0.1, 0.2 and 0.3 nm are calculated. The reduction of apparent Fe signal depends on the particle size and its effect is most obvious for particles smaller than 6 nm, where smaller particle leads to significant decrease of apparent Fe signal. This is also expected since smaller particles have higher ratio of surface atoms. As Pt segregates towards the surface, the increase of Pt signal is more obvious for smaller particles. Conversely, for particles larger than 12 nm the change of relative Fe signal does not show strong size dependence. As a comparison, the reduction of apparent Fe signal is also calculated for thin film geometry. The nanoparticles always shows a stronger reduction compared to thin film, which is mainly due to the spherical geometry, i.e. more surface atoms are probed.

It is worth noticing that the core-shell model assumes a continuous distribution of material, and the atomic nature of the material is ignored. In this sense the Pt layer thickness is better understood as an equivalent Pt content on surface. For example, 0.1 nm layer thickness is even smaller than the Pt inter-atomic distance, and should be understood as an incomplete monatomic layer of Pt segregation on the surface.

The measured Fe 2p to Pt 4f ratios for three nanoparticle samples and the thin film are also plotted in Figure 30. Compared to the simulated, the Pt layer thicknesses of 0.2 nm and 0.3 nm are deduced for 11.5 nm and 9.8 nm particles, respectively, and for the reference film a value of 0.3 nm is obtained. The larger particles and the film deliver similar results, as already observed in the context of oxidation. For the smallest particles (4.9 nm), however, a very thin Pt layer thickness smaller than 0.1 nm is observed for 4.9 nm particles. Comparing the extracted Pt shell thicknesses to that of a close-packed Pt monolayer of about 0.23 nm immediately suggests the following explanation for the various observed oxidation behaviors: in

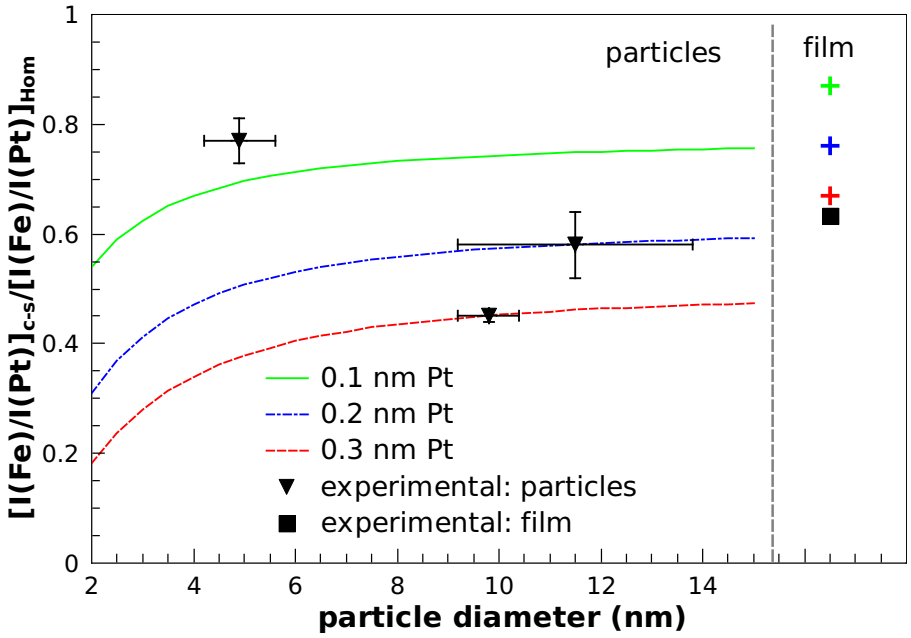

Figure 30: FePt–Pt core–shell model: ratio of Fe(2p)-to-Pt(4f) XPS intensities as calculated for a spherical core–shell particle of given diameter and Pt shell thickness normalized to the corresponding ratio $[I(\mathrm{Fe})/I(\mathrm{Pt})]_{C-S}/[I(\mathrm{Fe})/I(\mathrm{Pt})]_{Hom}$ for a homogeneous FePt particle of identical diameter. Different curves are calculated for three shell thicknesses as given in the inset. The crosses on the right of the vertical dashed line are obtained for a planar geometry with corresponding Pt top layers. Experimental data obtained for nanoparticles (solid triangles) as well as for a reference film (solid square) are included.

the as-prepared metallic state the reference FePt film as well as all particles behave similarly, forming detectable amounts of Fe oxide after exposure to pure oxygen for approximately 10^6 L. Annealing the samples causes Pt to segregate towards the surface. In this way, in the case of the film and the larger particles a Pt surface layer approximately one monolayer thick is formed which strongly impedes further oxidation. In the case of the small particles, however, this Pt monolayer is no longer complete and thereby loses its protecting effect. As a consequence, annealing of these small particles does not lead to a shift of the oxidation curve towards higher oxygen doses.

The reason why smaller particles do not form a complete Pt surface layer may be attributed to the compositional change within the core of the particle induced by Pt segregation. Generally, the relative number of Pt atoms needed for a complete surface layer increases with decreasing particle diameter due to the increasing ratio of surface-to-bulk atoms. For example, assuming that the 4.9 nm FePt particle formed complete Pt shell, the atomic composition of the core would shift from

from $Fe_{51}Pt_{49}$ to $Fe_{68}Pt_{32}$. According to the FePt bulk phase diagram, this change in composition is related to a structural transformation into the Fe_3Pt phase. The driving force of a decreasing total surface energy due to Pt segregation is probably overcompensated by the energy needed to form Fe_3Pt from FePt.

6 Magnetism of FePt and CoPt nanoparticles

6.1 Experimental details

FePt and CoPt nanoparticles are perpared by the reverse micelles as discussed in Section 2.2. The resulting particle sizes as determined by AFM and composition measured by XPS are summarized in Table 5. XPS spectra are obtained after the reduction by hydrogen plasma but without annealing, in order to avoid the effect of Pt surface segregation discussed in the Section 5.3.

Table 5: Summary of the nanoparticle samples investigated by XMCD method. The particle diameter is measured by AFM and composition is determined by XPS.

Material	Polymer	Diameter (nm)	Composition (Fe/Co:Pt)
FePt	PS(266)-b-P4VP(41)	2.6±0.7	48:52
FePt	PS(266)-b-P2VP(41)	4.5±1.3	44:56
FePt	PS(1779)-b-P2VP(695)	5.8±2.6	48:52
FePt	PS(528)-b-P2VP(177)	6.3±1.4	50:50
FePt	PS(1779)-b-P2VP(695)	9.4±1.3	46:54
CoPt	PS(1779)-b-P2VP(695)	5.8±2.0	56:44

The magnetic properties are characterized by XMCD performed at beamline PM3 at BESSY II synchrotron facility, Berlin (Germany). The plasma etching chamber is attached to the high-field XMCD end station, so that the sample can be exposed to reducing hydrogen plasma or high temperature, and the sample can be characterized in-situ. Each sample is reduced in hydrogen plasma for 15 - 30 minutes at 300 °C prior to inspection. Different annealing steps are then applied to the sample. During the annealing a hydrogen background pressure of 1×10^{-3} mbar is maintained to prevent oxidation. After annealing, the sample is cooled down within a hydrogen plasma. After each step, XMCD spectra are measured at Fe or Co $L_{2,3}$ edges with fixed photon helicity in magnetic field of ± 3 T at different sample temperatures. For each XMCD spectrum, 4 separate absorption spectra are obtained in +3 T, -3 T, -3 T, +3T magnetic field, respectively. The spectra of identical external fields are then merged together to compensate any systematic drift in the background signal. XMCD spectra are then analyzed according to the method described in Section 3.3.

Additionally, elemental specific hysteresis are taken at fixed photon energy at Fe or Co L_3 edge with maximum dichroic difference and scanning the external field. The correspondence of such measurement to hysteresis loops measured by standard magnetometry has been shown earlier [109].

6.2 XAS and XMCD of FePt and CoPt nanoparticles

Before discussing the magnetic properties, the chemical state of nanoparticles should be characterized by XAS spectra. XAS and XMCD spectra of 5.8 nm FePt nanoparticles just after hydrogen plasma reduction at 300 °C for 20 min. and after annealing at 740 °C for 30 min. are shown in Fig. 31. The spectra are measured at 15 K for the reduced sample and 11 K for the annealed sample. Normalization according to reference grid current has been applied, while background correction has not been performed, yet. The resonant absorption at Fe $L_{2,3}$ edges clearly shows that the Fe atoms are in metallic state. Only a single asymmetric peak exists at L_3 or L_2 edge, which is the fingerprint metallic Fe [93]. The Fe L_3 peak is located at 708.45 eV, which is identical to previous result from our group [11] and other literature reports [93, 55]. The XAS spectrum after annealing is virtually unchanged except for a constant shift in the background. The XMCD spectra (right panel in Fig. 31) show also the typical behavior of metallic Fe [55]. The L_2 edge exhibits a broad positive peak while the L_3 edge is composed of a narrow and large negative peak with a tiny positive contribution (indicated by arrow in Fig. 31). This small positive feature is characteristic of the Fe-L_3 XMCD spectrum [89] and should also be taken into account when applying the sum rules. As expected, the shape of the XMCD spectrum remains almost unchanged after annealing. For all the FePt nanoparticles measured after different annealing steps and at different temperature, the shape of the XAS and XMCD spectra stay nearly identical, which guaranties that no oxidation or other chemical reactions occur.

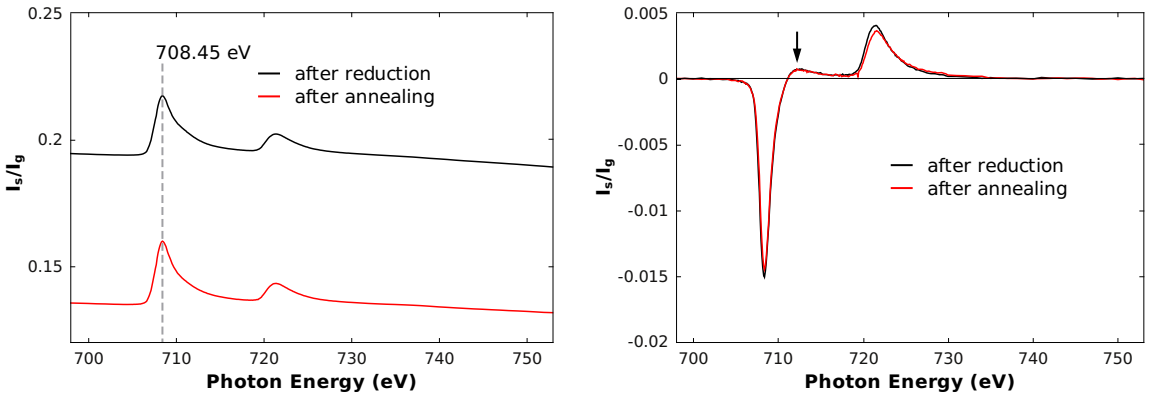

Figure 31: XAS (left) and XMCD (right) spectra of 5.8 nm FePt nanoparticles after hydrogen plasma reduction at 300 °C for 20 min. and after annealing at 740 °C for 30 min. The signal is obtained by normalizing the sample's total electron yield I_s with respect to that of the reference grid I_g. XAS spectra are averaged over single spectra measured in +/- 3T field, while the XMCD spectra are the difference between merged +/- spectra. No background correction is applied.

By normalizing sample current to reference grid current, the beam intensity variation should in principle be eliminated. However, a relative large change in the background is observed between the two measurement shown in Fig. 31. This effect is, most probably, due to small variation of the X-ray beam spot position and relative angle between the X-ray beam and sample. Such effect is an uncontrolled systematical error involving all measurements. Since the shape of the $L_{2,3}$ absorption edges remain unchanged, the spectra are fitted onto each other by introducing a linear background shift and a scaling factor for each spectrum, namely:

$$I_{fit}(E) = a \cdot E + b + c \cdot I(E) \tag{31}$$

$I(E)$ is the measured spectrum. The linear background $a \cdot E + b$ accounts for the uncontrolled systematically error and the scaling factor c corresponds to possible change of the Fe content. An example of such fitting is performed to spectra measured on the 5.8 nm FePt nanoparticles after annealing at different temperatures. The result of the fitting is shown in Fig. 32. All spectra can be fitted onto a single curve. Parameters of the linear background for each fitting show no systematic trend, but scaling factor c decreases systematically when different annealing steps are applied. As it is shown in Fig. 32, the scaling factor is reduced to about 90% of the initial value after annealing at high temperature. This means that the Fe content in the probing depth of TEY method is slightly reduced. Such apparent reduction of Fe content is consistent with the model of Pt surface segregation discussed in Section 5.3.

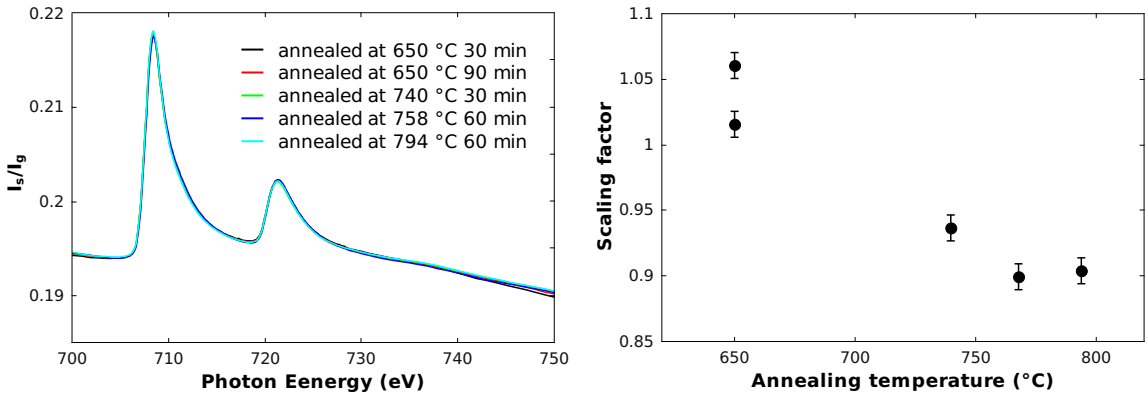

Figure 32: The XAS spectra of 5.8 nm FePt particles after different annealing steps are fitted onto each other according to (31). The result of the fitting is shown in the left figure. In the right figure the scaling factor for Fe $L_{2,3}$ signal is plotted against different annealing temperatures. The dashed curve is added as guideline for The slight decrease of the scaling factor from 1.06 to 0.90 indicates the reduction of the Fe content in the probing depth of XAS.

The XAS and XMCD spectra of 5.6 nm CoPt nanoparticles are shown in Fig. 33. The sample is measured after annealing at 700 °C for 90 min. and the spectrum is taken at 300 K. The XAS spectrum of CoPt shows that the Co atoms are also purely metallic [57]. Unlike Fe, the XMCD spectum at Co L_3 edge has only one negative peak without the positive shoulder.

To quantify the result and calculate the spin and orbital moment, all spectra are treated according to the method described in Section 3.3. According to (29) and (30), three quantities need to be extracted from the measurement: p and q as the integration of XMCD spectrum for L_3 and $L_{2,3}$, and A_t as the integration of XAS for $L_{2,3}$ peaks. As it is shown in Fig. 31, in the case of XAS the signal from the $L_{2,3}$ peaks is small compared to the background, while in XMCD the background virtually vanishes. The background correction such as shown in Fig. 18 will introduce a relatively large systematic error in A_t. Such error is different for each single spectrum, which makes the quantitative comparison between different measurements difficult. To remedy such difficulty, all the XAS spectra measured on the same sample are fitted together like shown in Fig. 32 and the corresponding scaling factors c are applied to each XMCD spectra. The average of the fitted XAS spectra is then taken as the universal XAS spectrum for all the measurements. Different measurements on the same sample can then be compared with the same systematic error in A_t. To compare the measurements on different samples, one further restriction is imposed when trying to fit the background described defined in (27). Here, the height parameter h in equation (27) is not taken as a fitting variable, but fixed such that in the final XAS spectrum after saturation correction the relative ratio of height after $L_{2,3}$ edges and L_3 peak height is a constant. This is illustrated in Fig. 34. Physically, the ratio h_1/h_2 is related to the number of empty s and d state around Fermi level, which should be a constant as long as chemical environment of Fe atom is unchanged. Such ratio is taken as identical for all the samples and the value is 0.20 for FePt. This value is comparable to the literature value obtained on FePt thin film of 0.18 [55] and nanoparticles of 0.19 [93].

6.3 Formation of the $L1_0$ phase

FePt nanoparticles prepared by the micellar method are generally found in the chemically disordered state after hydrogen plasma reduction and annealing over 600 °C is needed to achieve partial chemical order [11]. In order to track the transition from A1 to $L1_0$ phase, successive annealing is applied to the 5.8 nm FePt nanoparticles. The sequence and condition of the annealing steps are summarized in Table 6. The sample is treated with gradually increased temperature or longer

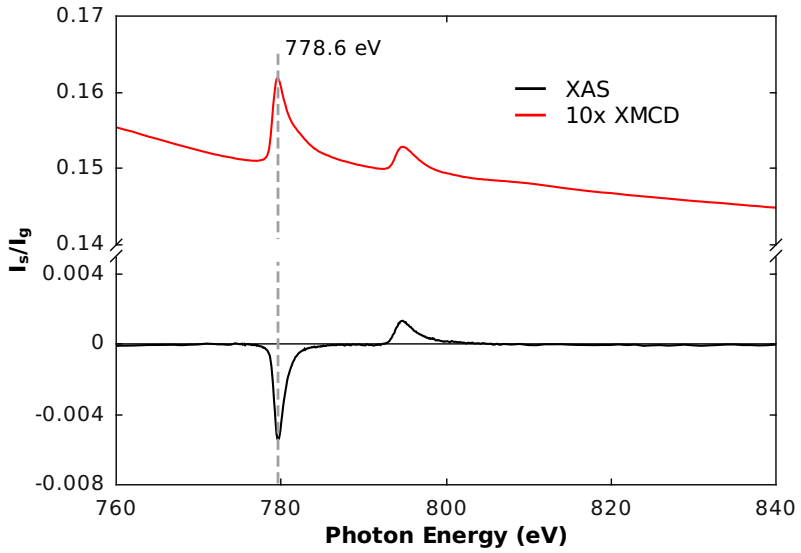

Figure 33: The XAS and XMCD spectra of 5.6 nm CoPt particles after annealing at 700 °C. The spectrum is taken at 300 K. The signal is obtained by normalizing the total electron yield from the sample I_s to the reference grid I_g. The XAS spectrum is the average between the spectra measrued in +/- 3T field, while the XMCD spectrum is the difference between those two. No background correction is applied.

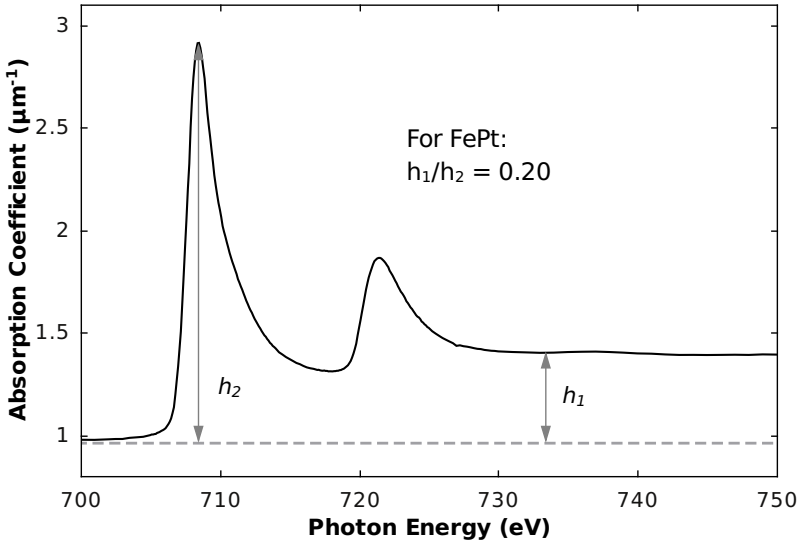

Figure 34: An example of the XAS spectrum after background removal and saturation correction. Spectra of different samples are normalized such that the h_1/h_2 is a constant.

annealing time. After each step the XMCD spectra as well as the hysteresis are measured.

Table 6: Series of annealing steps on 5.8 nm FePt nanoparticles. Every step is applied successively on the same sample, after which the XMCD measurement is performed at given temperature. Larger step number means higher annealing temperature or longer annealing time. In step 1, the sample has been reduced in hydrogen plasma while all other steps are in 10^{-3} mbar hydrogen background. In measurement of step 6 the X-ray spot is not fully focused on the sample, and the result is not valid.

Step	Annealing temperature (°C)	Time (min.)	Measurement temperature (K)
1	300	20	300
2	650	30	290
3	650	60	290
4	700	30	265
5	740	30	260
6	758	60	N.A.
7	768	120	260
8	794	60	300

As discussed before, a universal XAS spectrum is obtained by fitting spectra of all the measurements. The result after saturation correction is shown in Fig. 35. The background is determined considering the condition imposed on the peak shape as shown in Fig. 34. By applying such normalization procedure, XMCD spectra of different measurements can be directly compared and element-specific moments can now be extracted from the XMCD spectra by applying sum rules.

XMCD spectra and hysteresis are measured at 15 K and 300 K after hydrogen plasma reduction (step 1), presented in Fig. 36. XMCD spectra clearly reveal different intensities at two different temperatures, but the shape of the curves match each other. The magnetic moment of Fe atoms is calculated by sum-rules and the number holes in d shell is taken as 3.705 [50]. The moment per Fe atom at 15K is $\mu_s^{eff} = 2.36 \pm 0.12\,\mu_B$, $\mu_l = 0.19 \pm 0.03\,\mu_B$ and $\mu_l/\mu_s^{eff} = 0.082 \pm 0.014$. At 300 K the moment decreases significantly: $\mu_s^{eff} = 1.83 \pm 0.12\,\mu_B$, $\mu_l = 0.16 \pm 0.03\,\mu_B$ and $\mu_l/\mu_s^{eff} = 0.087 \pm 0.018$. However, the ratio of orbital-to-spin moment stays constant, indicating there is no change in the magnetic ordering and the reduced moment at 300 K is the effect of thermal fluctuations. The hysteresis measurement at 15 K shows clearly ferromagnetic response, with coercivity $\mu_0 H_c = 0.13\,\mathrm{T}$ and remanence $M_r/M(3T) = 0.58$. The coercivity and remanence of the hysteresis measured at 300 K are both close to 0. The opening the hysteresis curve at 300 K is very small and within the experimental error, thus the nanoparticles are super-

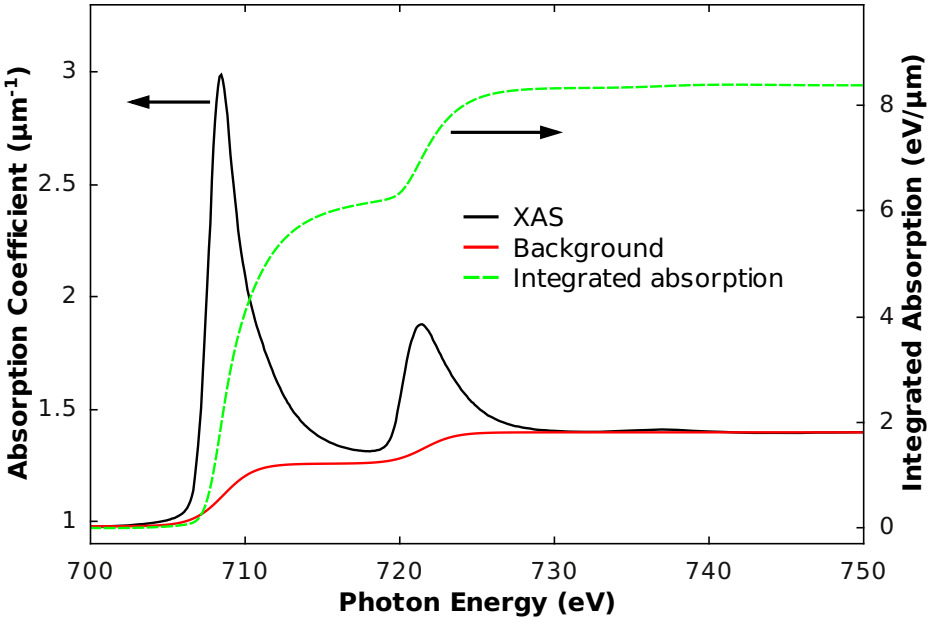

Figure 35: XAS spectrum at Fe $L_{2,3}$ for 5.8 nm FePt nanoparticles after normalization according to Section 6.2. After subtracting the two-step background the total area of the Fe $L_{2,3}$ is obtained by integration.

paramagnetic at 300 K. In both hysteresis measurements, the sample is saturated at 3 T, which means the moment measured by XMCD is proportional to the true spontaneous magnetization, and the reduced moment at 300 K is due to the effect of thermal excitation. Such dependence of spontaneous magnetization to temperature is well understood in ferromagnetic materials [26]. The Curie temperature is estimated later in Section 6.5.

In the superparamagnetic state the response of nanoparticles to external field can be expressed by the Langevin function [26]:

$$M(H)/M_s = \coth\left(\frac{\mu_0 m H}{k_B T}\right) - \frac{k_B T}{\mu_0 m H} \tag{32}$$

, where H is the external magnetic field, $k_B T$ the total thermal energy and m is the magnetic moment of the particle. By fitting the superparamagnetic curve the total moment of each particle can be obtained, providing another independent method to measure the moment. Here, the moment per particle is $9.5(7) \times 10^{-20}\,\mathrm{A \cdot m^2}$. Assuming spherical shape with diameter of 5.8 nm, the saturation magnetization is then 940 kA/m. This value is 82% of the saturation magnetization of bulk FePt at room temperature according to Table 1. If one assumes that the relative change of magnetization is identical to the relative change of Fe atomic moments, the spontaneous magnetization at low temperature should be 1210 kA/m,

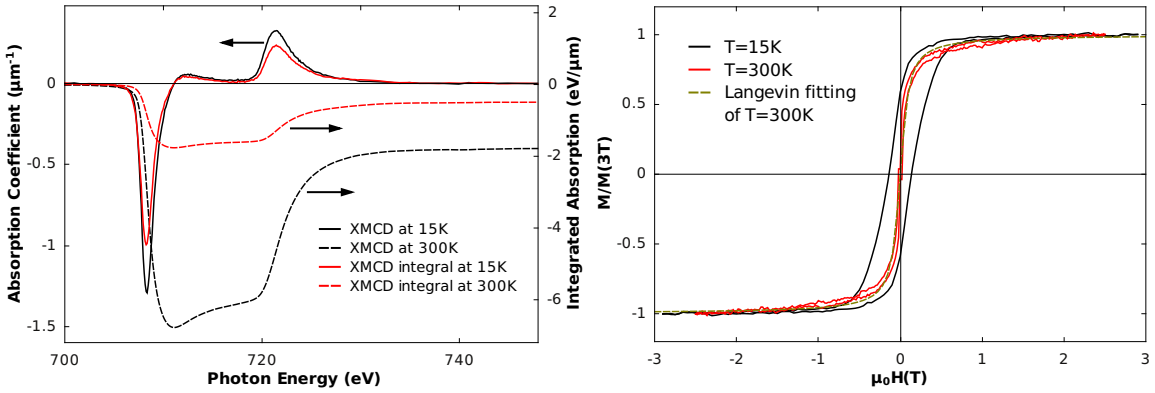

Figure 36: The XMCD spectra (left) and hysteresis (right) of 5.8 nm FePt nanoparticles after hydrogen plasma at 300 °C for 20 minutes (step 1). The measurements are performed at 15 K and 300 K, respectively. The hysteresis measured at 300 K shows superparamagnetism and the curve can be fitted with Langevin function. The fitting reveals an average moment per particle of $9.5(7) \times 10^{-20} \mathrm{A} \cdot \mathrm{m}^2$.

which is very close to 1250 kA/m observed in FePt thin films at 10 K [110]. The discrepancy of room temperature magnetization can only be explained by reduced Curie temperature: while the low temperature magnetization in nanoparticles is identical to the bulk, due to reduced Curie temperature, the saturation magnetization will have a larger decrease compared to bulk.

After annealing at 740 °C for 30 min. (step 5) XMCD and hysteresis are measured at 17K and 265 K and shown in Fig. 37. The shape of the XMCD spectra remains unchanged and compared to those measured after step 1 (Fig. 36), only different intensities are observed. The moment per Fe atom at 17 K is $\mu_s^{eff} = 2.27 \pm 0.12\,\mu_B$, $\mu_l = 0.12 \pm 0.03\,\mu_B$, $\mu_l/\mu_s^{eff} = 0.053 \pm 0.014$ and at 265 K $\mu_s^{eff} = 1.96 \pm 0.12\,\mu_B$, $\mu_l = 0.16 \pm 0.03\,\mu_B$, $\mu_l/\mu_s^{eff} = 0.082 \pm 0.017$. Similar to the observed moment difference after step 1, the Fe moment reduces significantly at higher temperature. Compared to the moment observed after step 1, the spin and orbital moment measured at low temperature are slightly reduced, and the spin moment at higher temperature is slightly increase. However, such change is relatively small and comparable to the error bar of the moment determination. The hysteresis loops, however, show a significant change. The curve measured at 17 K behaves as a very hard ferromagnetic material, with $\mu_0 H_c = 0.78\,\mathrm{T}$ and $M_r/M(3T) = 0.56$. Moreover, the hysteresis curve opens already at 3 T field. This indicates that with 3 T field it is not sufficient to fully magnetize the particles, and the measured hysteresis is in fact a "minor loop". This also means that the moment observed at 3T is lower than the true spontaneous magnetization, which is in line with the slightly reduced moment measured by XMCD at low temperature compared to the moment measured before

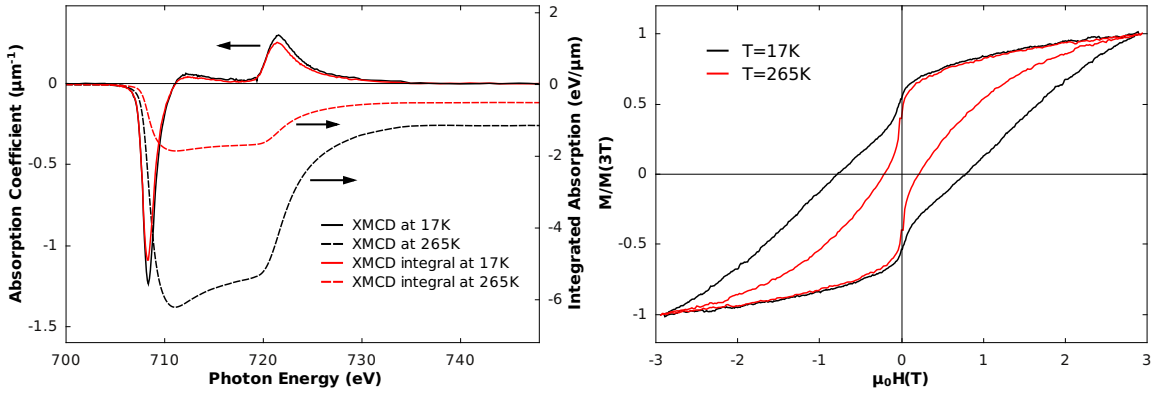

Figure 37: The XMCD spectra (left) and hysteresis (right) of 5.8 nm FePt nanoparticles after annealing at 740 °C for 30 minutes (step 4). The measurements are performed at 17 K and 265 K, respectively.

annealing. The overall shape of the hysteresis loop also changes compared to those presented in Fig. 36. In the re-magnetization process, the magnetization decreases rapidly at around 0 T shown as a "narrow waist" around 0 field, but then switches gradually across a large field range shown as a long tail in the negative field range. This suggests that there are two components in the total magnetic moments with two different magnetic anisotropy energies [12]. The hysteresis measured at 265 K shows clearly an open hysteresis, with $\mu_0 H_c = 0.20\,\mathrm{T}$ and $M_r/M(3T) = 0.40$, and its shape also suggests that there are two components with different magnetic anisotropies. By thermal excitation, however, the H_c is strongly reduced and with 3 T field one is able to saturate the sample. The remanence is a bit lower than the expected value of 0.5 from Stoner-Wohlfarth model, which means some portion of the particles are still superparamagnetic at 265 K.

Although a significant change in hysteresis is observed after the annealing step, the orbit and spin moment as well as their ratio remain almost unchanged. This is in distinct contrast to the result obtained in 6 nm FePt colloidal particles reported by Antoniak et al. [93], where the orbital moment of Fe was almost completely quenched after hydrogen plasma reduction at room temperature ($\mu_l = 0.056\,\mu_B$), and increased to about 0.24 μ_B after annealing at 600 °C. The relatively large incease in the orbital moment was related to the formation of partial chemical order. On the other hand, the XMCD measurements on FePt thin films suggest that the change of orbital moment due to chemical order should be fairly small [55], with 0.20 μ_B for A1 phase and 0.24 μ_B for $L1_0$ in [001] orientation. It is worth noticing that the extreme small Fe orbital moment in chemically disordered FePt nanoparticles reported by Antoniak et al. [93] has never been observed in disordered FePt thin film or bulk and its value is even smaller than the orbit moment observed in pure

Fe [59]. On the other hand, the observed orbital moment for chemically disordered 5.8 nm particles according to Fig 36 is in line with the thin film result. This suggests that the extreme low orbit moment observed by Antoniak et al. [93] cannot be due to chemical disorder alone. A possible explanation is the slightly different plasma reduction condition: while the hydrogen plasma reduction is carried out at 300 °C in this study, the temperature was kept at room temperature in [93]. The hydrogen plasma might introduce the hydrogen impurities or hydride formation in FePt lattice, changing its magnetic properties. Simliar effect of hydrogen plasma has been observed in Co nanoparticles, where CoH_x is formed after hydrogen plasma reduction at room temperature. The the hydrogen could be expelled by annealing at 650 °C for 5 min. Compared to pure Co nanoparticles, the orbital moment of Co in CoH_x nanoparticles is reduced from 0.16 μ_B to 0.06 μ_B per Co atom [111].

The Stoner-Wohlfarth model can be used to relate the hysteresis curve to the magnetic anisotropy energy [26]. The detailed application of the model to magnetic nanoparticles is discussed in many literature's [33, 34, 35]. Hysteresis loops shown in Fig. 36 and 37 have been analyzed quantitatively by Wiedwald et al. [12], where the low temperature hysteresis curves are simulated considering a distribution of uniaxial anisotropy energy K_u among the particles. While the hysteresis loop after reduction can be simulated using a single anisotropy energy constant $K_u = 0.15\,\mathrm{MJ/m^3}$, a bimodal distribution of K_u is necessary to reproduce the features of the hysteresis curve after annealing, where a low anisotropy component $K_L = 0.10\,\mathrm{MJ/m^3}$ and a high anisotropy component $K_H = 1.90\,\mathrm{MJ/m^3}$ are observed. The distribution of anisotropy energy is shown in Fig. 38, where variance of the low anisotropy component is much narrower than the high anisotropy component. The emergence of a high anisotropy component indicates the formation of chemical order. However, the high anisotropy component K_H in nanoparticles is only about 30% of that observed in $L1_0$ FePt bulk material. Assuming that the dependency of anisotropy energy to the degree of order is the same as in FePt thin films [27], the degree of order can be estimated to $S = 0.3$.

Similar bimodal distribution of anisotropy energy has also been observed in 2.6 nm FePt particles after annealing up to 790 °C for 60 min. According to fitting of the hysteresis measured at 10 K, the anisotropy energy of the low and high anisotropy portion are $K_L = 0.15\,\mathrm{MJ/m^3}$ and $K_H = 1.71\,\mathrm{MJ/m^3}$, respectively. The anisotropy distribution is shown in Fig. 38. The shape of the distribution is similar to what has been observed in 5.8 nm particles. Alternative to a low temperature measurement, the hysteresis measured at higher temperature is influenced by the thermal excitation, where particles with lower magnetic anisotropy will become gradually

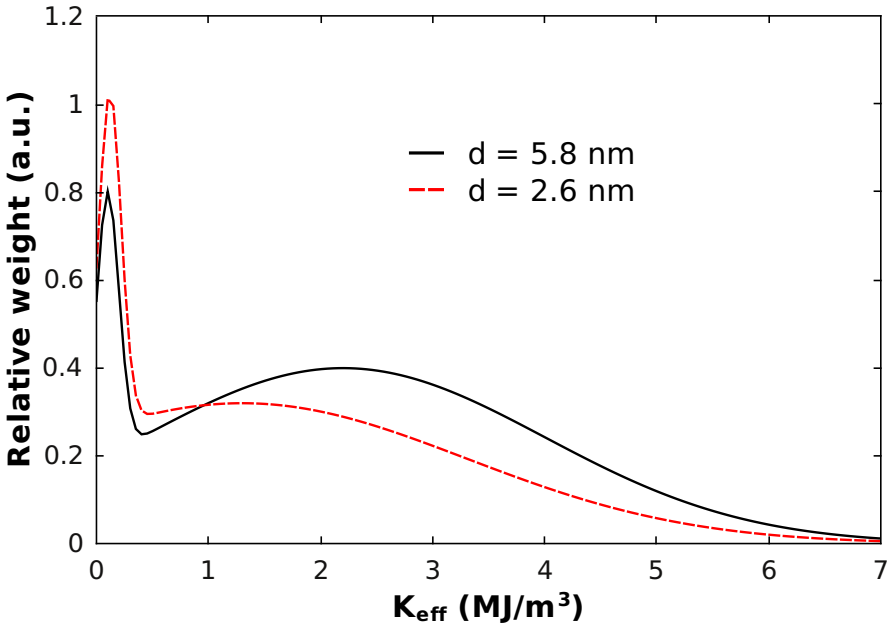

Figure 38: Distribution of anisotropy energy of 2.6 nm and 5.8 nm FePt particles are obtained by fitting the hysteresis loops measured at low temperature. 5.8 nm particles are annealed at 740 °C for 30 min. and 2.6 nm particles are annealed at 790 °C for 60 min. Details are discussed in text.

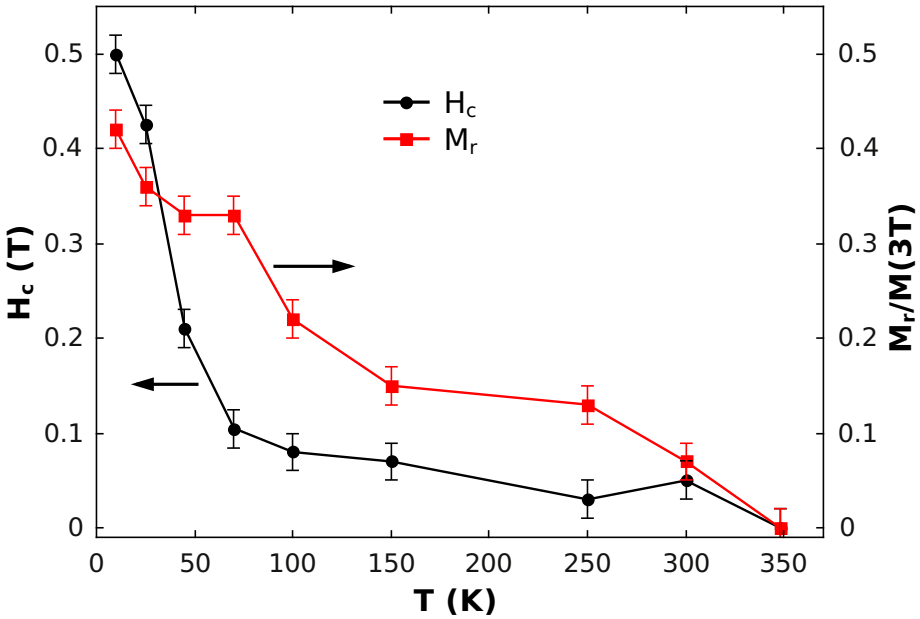

Figure 39: Temperature dependence of coercivity H_c and remanence M_r measured for 2.6 nm FePt particles after annealing at 790 °C for 60 min.

superparamagnetic. To track such transition the hysteresis loops are measured successively as function of temperatures. The temperature dependence of coercivity H_c and normalized remanence $M_r/M(3T)$ are presented in Fig. 39. As temperature increases, both H_c and $M_r/M(3T)$ are reduced as larger portion of the particles becomes superparamagnetic. A distinct feature of the $M_r/M(3T) - T$ dependence is that it does not follow a smooth curve. M_r decreases rapidly when temperature increases from 10 K to 45 K, then stays constant from 45 K to 70 K, followed by a gradual decrease from 70 K to 350 K. As a first approximation, deviation of normalized remanence to 0.5 can be viewed as proportional to ratio of particles that are superparamagnetic according to Stoner-Wohlfarth model:

$$R = 1 - 2M_r/M_s \tag{33}$$

According to this relation, the temperature where $M_r/M(3T)$ decreases represents that portion of particles crossing their blocking temperature and become superparamagnetic, and the magnitude of the decrease is proportional to the relative amount of these particles. And such temperature can be converted to anisotropy energy density according to equation 4. The shape of $M_r/M(3T) - T$ curve suggests that there are two portions of anisotropy energy among the particles: a low anisotropy portion with narrow energy distribution and a high anisotropy portion with broad energy distribution. Such expectation is consistent with the anisotropy distribution obtained by fitting the hysteresis measured at low temperature, as shown in Fig. 38.

In both 2.6 nm and 5.8 nm FePt particles, the anisotropy energy after annealing is strongly reduced compared to bulk value, and the anisotropy energy shows a bimodal distribution. The low anisotropy energy component K_L is around 0.1 MJ/m^3 for both samples, which coincides with the effective magnetic anisotropy energy of FePt in A1 phase [27]. This raises the question whether the A1 $\rightarrow$ $L1_0$ transformation by annealing is incomplete and some portion of the particles stays in A1 phase, giving raise to the low anisotropy energy component. To help answering this question, it is very helpful to track the evolution of A1 to $L1_0$ transition. In Fig. 40 the Fe moments, coercive field H_c and remanence $M_r/M(3T)$ after different annealing steps (see Table 6) are presented. To avoid unsaturated sample due to emerging high anisotropies, only the results obtained at high temperature are discussed here. Although the slightly different measurement temperatures for each steps will in principle change the Fe moment, such change is expected to be smaller than the error bar. The temperature dependence of moment will be discussed further in Section 6.5.

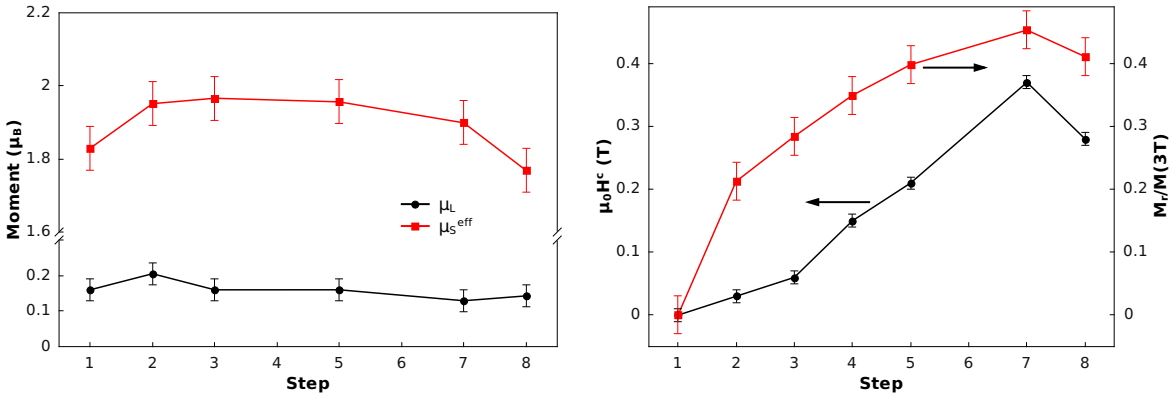

Figure 40: The evolution of Fe magnetic moment (left), coercive field and remanence (right) after each annealing step according to Table 6. Spin and orbital moments are obtained by applying the sum rules to the XMCD spectra. The coercive field is obtained from hysteresis measurement. At each step the measurements are performed at slightly different temperature between 265 K and 300 K. The influence of temperature variation to the result is expected to be fairly small and below the experimental error.

First, it is noticed that the evolution of Fe moments shows only little variation after each annealing step, indicating that the chemical environment of Fe remains almost unchanged. The orbital moment stays constant around 0.16 μ_B within the error bar. The spin moment increases slightly from 1.83 μ_B to 1.95 μ_B when annealing starts (step 2), and decreases at the last annealing step to 1.77 μ_B. However, the relative change is just on the edge of the error bar. Such behavior is, to a certain degree, also expected, since the difference in the Fe moment in A1 and $L1_0$ phase is found to be small in thin film [55]. On the other hand, the coercive field H_c changes dramatically. Starting from 0 as superparamagnetism ($\mu_0 H_c = 0$) in the reduced state, H_c gradually increases for higher annealing temperature or longer annealing time. H_c reaches a maximum of $\mu_0 H_c = 0.38\,\mathrm{T}$ after annealing at 760°C for 120 min. and then decreases to $\mu_0 H_c = 0.30\,\mathrm{T}$ after annealing at 794 °C for 60 min. In the first approximation, H_c is proportional to the anisotropy energy, and thus this quantity can be related to the degree of chemical order [48]. Successive annealing gradually increases the average degree of chemical order of the particles, until the annealing temperature exceeds 760 °C, after which the average degree of chemical order decreases again. This conclusion is consistent with remanence change after each annealing steps. According to equation (33), the ratio of superparamagnetic particles decreases gradually from 100% after reduction to 10% after annealing at 760°C for 120 min. But annealing at 794 °C for 60 min. increases the ratio to 18%. It seems that at temperature up to 794 °C the $L1_0$ phase is no longer thermal dynamically

favorable.

According to the bulk phase diagram of FePt (Fig. 3), the thermal equilibrium transition from $L1_0$ to A1 in FePt would occur around 1300 °C at equiatomic composition, and decreases rapidly when composition differs from 50:50. In nanoparticles, this transition temperature T_D can be significantly reduced up to 400 K [112, 43]. In similar CoPt system, the T_D of nanoparticles is reduced by 325–175 K compared to bulk, and T_D of smaller particles is lower [63]. Such effect might provide the explanation for the reduced coercivity after annealing at very high temperature.

It is noteworthy that after each annealing step, the superparamagnetic component always exists, and simulation of low temperature hysteresis loops always yields a bimodal anisotropy distribution. It is quite reasonable to postulate that the low anisotropy portion of particles from the fitting corresponds to the superparamagnetic component observed in the hysteresis measured at higher temperature, and those particles are still in A1 phase. By longer annealing time and higher annealing temperature, more particles are transformed to partially ordered phase, but the transformation is never complete. The presence of A1 phase at each annealing step means the system is kinetically hindered and is not at thermodynamic equilibrium. Similar limit of kinetics in A1 $\rightarrow$ $L1_0$ transition has also been observed in colloidal FePt particles [113]. While increasing temperature would enhance kinetics of the phase transition, thermodynamic driving force will decrease and possibly leads to reduced degree of order at equilibrium. This is especially important in nanoparticle system, where transition temperature T_D can decrease significantly. To achieve high degree of order the annealing has to be performed at relative low temperature for very long time [63].

According to this model, the portion with high anisotropy energy as shown in Fig. 38 corresponds to particles transformed to partial $L1_0$ order. Even when the degree of order is not restricted by kinetics in these particles, the maximum anisotropy energy can never reach the bulk value. The average anisotropy energy is below 40% of the bulk value. This suggests that an intrinsic limit to the anisotropy energy exists in FePt nanoparticles. Similar reduction has also been observed in FePt nanoparticles prepared by colloidal methods [93] and inert gas condensation [114]. In all these cases the maximum effective anisotropy energy K_u is no more than 30% the bulk value.

Different mechanism has been proposed to explain the low value of K_u. One idea is that the chemical composition varies between different particles, and deviation from stoichiometry will decrease the degree of order [12]. Following this explanation, if the variation is totally random, the composition distribution would

follow a Gaussian distribution centered at equiatomic composition, which would lead to an anisotropy energy distribution with a higher weightage at high K_u. The observed anisotropy energy distributions clearly differ from such pattern, which suggests that either the composition variation is not random but towards Fe rich or Pt rich, or other mechanisms are influencing the anisotropy energy.

One possible explanation for non-random composition variation is the tendency of Pt segregation on FePt nanoparticle surfaces, which has been discussed in Section 5.3. Due to the Pt segregation on the surface, the core of the particles will be Fe-rich, shifting its composition away from equiatomic and reducing the degree of order as well as anisotropy. Lattice Monte Carlo simulations confirm that the Pt segregation on surfaces will disrupt the chemical order in the core of FePt nanoparticles [43].

Yet another completely different reason might explain the low anisotropy obtained in FePt nanoparticles. According to Fig. 26, defects such as twin boundaries and stacking faults exist in nanoparticles and one particle is divided into several regions with different crystallographic orientations. This means the effective anisotropy energy of the whole particle is averaged over different magnetocrystalline anisotropy terms pointing towards different directions. Depending on the situation, the final effective anisotropy could be very low even when the chemical order in each small region is high.

The formation of $L1_0$ phase has also been observed in CoPt nanoparticles. Here, 5.6 nm CoPt nanoparticles are annealed at 700 °C for 90 min. The hysteresis loops are then measured at different temperatures, shown in Fig. 41. The result is very similar to that obtained on the FePt nanoparticles of the same size. The hysteresis loop measured at low temperature also shows a bimodal distribution of anisotropy energy. The observed open hysteresis loop at 300 K shows $\mu_0 H_c = 50\,\mathrm{mT}$ and $M_r/M(2.9T) = 0.20$. While the remanence of ideal Stoner-Wohlfarth particles is expected to be $0.5M_s$, small remanence observed at 300 K indicates that 60% of the particles are superparamagnetic at 300 K, which originates from the portion of particles with low anisotropy. The average anisotropy energy is estimated to be $1.5\,\mathrm{MJ/m^3}$, which is 29% of the CoPt bulk value.

The moment of Co atoms is determined by applying the sum rules, using the number of d holes $n_h = 2.628$ [57]. The result is summarized in Table 7. The spin moment at low temperature is 1.60 μ_B, which is 9% smaller than the value of 1.76 μ_B observed in CoPt thin film [57]. This small difference can be ascribed to an insufficient external field to saturate the sample, as indicated by the "minor loop" shown in Fig. 41. The spin moment measured at higher temperature shows a systematic decrease. This trend is similar to that observed in FePt particles, where the magneti-

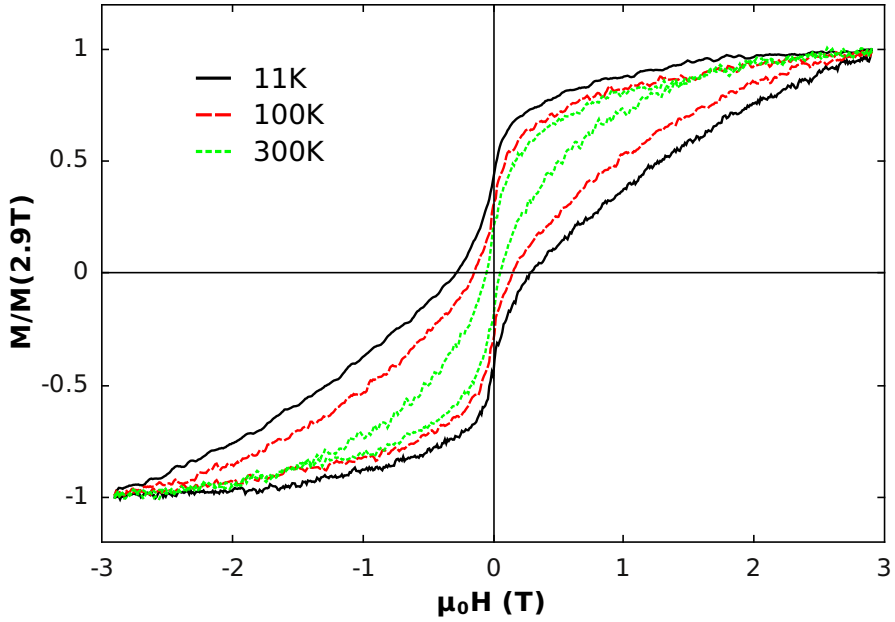

Figure 41: Hysteresis loops of 5.6 nm CoPt nanoparticles after annealing at 700 °C for 90 min. Note that the signal is normalized to the magnetization at maximum field [12].

zation decreases as the temperature approaches T_C. The orbital moment measured at different temperatures shows little change. The μ_l/μ_s^{eff} = 0.11 is comparable to the ratio observed in CoPt thin films [57, 115].

Table 7: Spin and orbital moment of Co atoms in CoPt nanoparticles after annealing at 700°C for 90 min. The ratio of orbital-to-spin moment is also listed.[12]

T(K)	$\mu_s^{eff}(\mu_B)$	$\mu_l(\mu_B)$	μ_l/μ_s^{eff}
11	1.60 ± 0.16	0.19 ± 0.04	0.13 ± 0.02
100	1.56 ± 0.19	0.15 ± 0.04	0.10 ± 0.03
300	1.26 ± 0.01	0.15 ± 0.01	0.11 ± 0.01

6.4 Size dependent magnetic properties of FePt nanoparticles

The results from the previous subsection gives evidence for the formation of $L1_0$ phase in the 5.8 nm FePt particles after annealing. It is an interesting question whether this transition can be observed in particles of different sizes, and what degree of chemical order can be obtained. In this part these questions will be addressed.

First of all, the formation of the $L1_0$ phase in differently sized particles can be tracked by hysteresis measurements [12]. The results are summarized in Fig. 42. Af-

ter annealing at 700 °C for 30 min, hysteresis loops are measured at 300 K and 15 K, respectively. Coercivity measured at 300 K shows a systematic decrease as particle size is reduced. For particles with diameter smaller than 4.5 nm, coercivity reduces to 0 and the particles are superparamagentic. For particles showing superparamagnetism at a given temperature, its anisotropy energy obeys $30k_BT < K_uV$, assuming the time window for the measurement to be 600 s [26]. In case the bulk anisotropy energy is reached in FePt nanoparticles, the critical diameter can be calculated to be 3.2 nm, below which the particles would show superparamagnetism at 300 K. The experimental critical diameter at 4.5 nm, however, indicates that the bulk anisotropy energy is not achieved in nanoparticles. The insert in Fig. 42 shows the coercivity measured at 15 K versus particle size, which has significant scattering. Similar to what has been shown in Fig. 37, hysteresis loops measured after annealing always exhibit two kinds of switching behavior, corresponding to two components with different anisotropy energy. Depending on relative ratio of two components and the value of anisotropy, the observed coercivity can vary within a large range.

Using a bimodal anisotropy energy distribution hysteresis loops measured at 15 K can be successfully fitted [12]. As a result, the low anisotropy energy component K_L stays constant around 0.1 MJ/m^3 among different sizes. This value coincides with the effective magnetic anisotropy energy of FePt in A1 phase [27]. The high anisotropy energy components K_H have no clear correlation with particle size but all are found below 2.5 MJ/m^3. The median effective magnetic anisotropy energy K_{eff} shows similar scattering. Assuming the same relationship between anisotropy energy and degree of order observed in FePt thin film [27], the degree of order in nanoparticles can be estimated. Independent of particle size, maximum degree of order S obtained in FePt nanoparticles is always below 0.35. This result is quite different form those obtained in ultra-thin granular FePt films, where the anisotropy energy reaches value of bulk FePt for film thicker than 7nm, and starts to decrease as the film thickness is reduced [44, 110].

As it was discussed in the previous subsection, presence of low anisotropy portion indicates that the system does not reach equilibrium, i.e. the measured K_H and K_{eff} has not reached the maximum value allowed in equilibrium. In contrast, the hysteresis loops measured in thin films show a homogeneous anisotropy energy as well as chemical order, indicating that the system has reached equilibrium and the chemical order is only limited by the thermodynamic driving force [110]. Indeed, even anisotropy measured in 3 nm thick FePt films is 3.5 MJ/m^3 [110], larger than all anisotropy values observed in the nanoparticles, which again suggests that transition to the chemically ordered phase in nanoparticle is not complete. As a result,

the dependence of chemical order in equilibrium to particle size cannot be testified in this study. The measured anisotropy energy distribution is due to the limited kinetics of A1 $\rightarrow$ $L1_0$ transition.

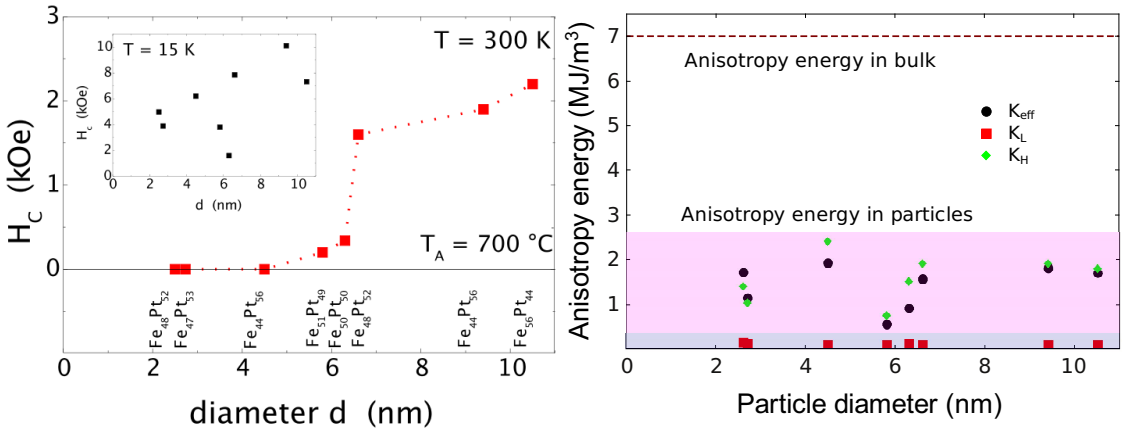

Figure 42: Size dependence of coercive field (left) and magnetic anisotropy energy (right) of FePt nanoparticles after annealing at 700 °C for 30 min. Both curves are extracted from element specific hysteresis loops. Compositions shown in the left figure are determined by XPS. The coercive fields in the left figure are measured at 300 K, while in the insert are those measured at 15 K. The magnetic anisotropy is evaluated using the Stoner-Wohlfarth model. In the right figure size dependence of the median effective magnetic anisotropy constant K_{eff} and the peak values K_H and K_L are presented (details are given in the text). All K_L values are almost identical and corresponds to chemically disordered FePt, and K_L values lie in a region much lower than the bulk anisotropy energy. Left panel is taken from [12].

Spin and orbital moments of Fe atoms after the annealing at 700 °C for 30 min. are determined from XMCD spectra using sum rules. The results are shown in Fig. 43. The orbital moments stay within 0.1 - 0.2 μ_B and possess no clear size dependence. The spin moments, however, slightly increases with increasing particle size. The spin moment of 9.8 nm particles approaches the bulk value of 2.45 μ_B measured by XMCD [55]. Unlike the anisotropy energy, the relative change of magnetic moments with respect to chemical order is small. According to Table 2, the spin moment per Fe atom in FePt is 2.24 μ_B in A1 phase and 2.45 μ_B in $L1_0$ phase. The variation of spin moments according to the degree of order is too small to account for the observed moment change. Besides, all the particles have relatively low degree of order as indicated in Fig. 42. It is thus plausible that the observed change in spin moments is a finite size effect. Indeed, similar positive correlation of magnetization with film thickness has been observed in FePt thin films, where saturation magnetization M_s of 3 nm thick film is reduced to 70 % of M_s in 10 nm thick film, and the 10 nm thick film has almost the same M_s as bulk FePt

[110]. Similar trend is evident in the nanoparticles, where spin moment in 2.57 nm particles is 76% of that in 9.8 nm particles.

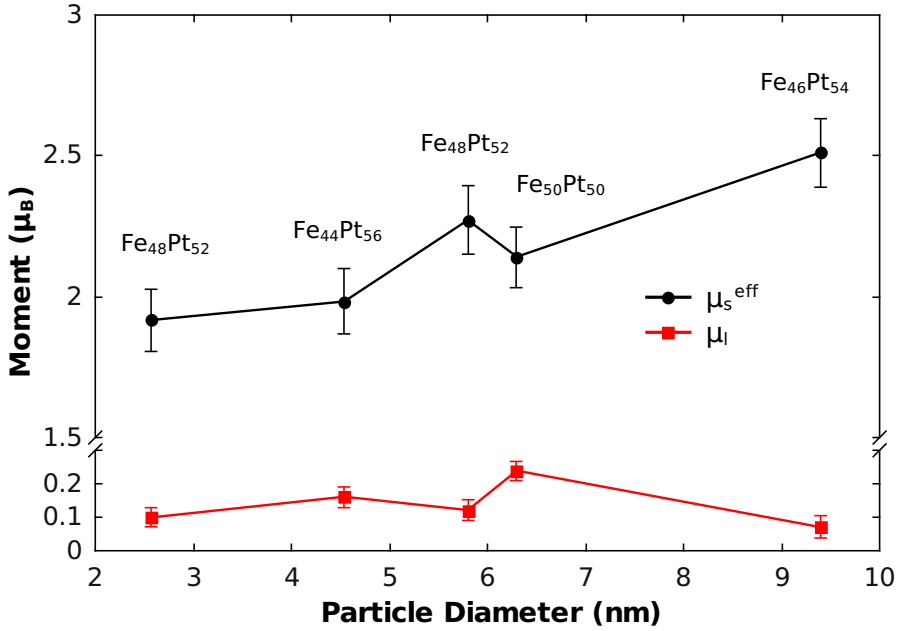

Figure 43: Spin and orbital moments of Fe atoms in differently sized FePt nanoparticles after annealing at 700 °C for 30 min measured at temperatures between 10 to 15 K. Corresponding compositions determined by XPS are also given.

Many models have been proposed to explain reduced magnetic moments as well as their size dependence in FePt nanoparticles. One explanation is due the intrinsic problem of XMCD measurement, where sum-rule analysis of the spectrum yields an effective spin moment which contains a negative contribution from the magnetic dipole moment. Such contribution cannot be canceled out even for randomly oriented crystallographic axes [90]. Assuming an increased negative contribution from the surface atoms, the effective spin moment could give certain correlation with particle size considering the limited probing depth of TEY detection method. However, such effect is quite small and it is not likely to account for almost 30% change in the moment observed in nanoparticles as well as in thin films. Also the reduced moments in thin films and nanoparticles can be observed using standard magnetometry, where the total magnetic moment of the sample is measured [116, 110]. Another possible explanation is that Fe atoms on the particle surface are subjected to an even stronger anisotropy contribution, which forces moments of surface atoms pointing perpendicular to the surface, effectively reducing the observed magnetization of the surface atoms in limited external field. Example of such behavior has been observed in $\gamma - Fe_2O_3$ nanoparticles, where hysteresis curve at high field has

a slightly positive slope [117]. Similar canting effect in FePt has not be reported in the literature, and an extremely strong surface anisotropy for FePt nanoparticles with relative small degree of order is unlikely.

An alternative model proposed by Antoniak et al. ascribes reduced moments in FePt nanoparticles to local chemical environment of Fe atoms [51]. To summarize shortly, the moment of Fe atoms depends on its local chemical environment. The Fe moment will increase with increasing local Pt concentration, till local composition reaches 50:50, after which further increase of Pt content does not influence Fe moment. In case of FePt nanoparticles, it has found out that Fe atoms are in Fe-rich environment and Pt atoms in Pt-rich environment by extended X-ray absorption fine structure (EXAFS), which effectively reduces the moment per Fe atom. If we take into account of the Pt segregation effect discussed previously, the following model may explain the reduction of magnetic moment in nanoparticles: assuming a layer of Pt atom is formed on the particle surface, the core of the particle will be depleted of Pt. Such effect will be stronger for smaller particles, leading to more Fe-rich core and smaller Fe moment. Assuming a monolayer of Pt (thickness of 0.23 nm) is formed on particle surface due to segregation, for 9.4 nm $Fe_{50}Pt_{50}$ particles composition will shift to $Fe_{56}Pt_{44}$. But for 5 nm $Fe_{50}Pt_{50}$ particles composition will change to $Fe_{60}Pt_{40}$. The effect of composition shift is stronger for smaller particles, leading to more reduced moments in smaller nanoparticles. For particles even smaller than 5 nm, as discussed in Section 5.3, a complete Pt layer segregation is not favorable due to strong composition change which would require a phase transition towards Fe_3Pt in the core. In other words, the shift in the core composition has certain limited range and the Pt segregation is hindered so that the composition change is kept within this range. Due to the limited composition shift the magnetic moment for particles smaller than 5 nm does not show significant size dependence.

6.5 Temperature dependent magnetization

As discussed in previous sections, the magnetic moments per Fe atom decreases when measured at higher temperature. Such temperature variation is summarized in Table 8. The average moment measured around room temperature is about 80 % of the value obtained at low temperature. According to the estimation of mean field theory, such reduction in moment corresponds to a temperature reaching 0.8 of Curie temperature, assuming spin quantum number $S = 3/2$ [26]. However, it is well known that mean field theory underestimates the effect of thermal fluctuations at low temperature. In order to get a more reasonable estimation of Curie temperature a phenomenological model of $M \sim T$ by Kuz'min [118] is used:

$$\mu(T) = \mu(0)\left[1 - \gamma(T/T_C)^{3/2} - (1-\gamma)(T/T_C)^{5/2}\right]^{1/3} \quad (34)$$

The 0 K magnetic moment $\mu(0)$ and Curie temperature T_C serves as scaling factor for the curve, and γ is the factor which influence the shape of the curve. γ value for FePt with low degree of order is experimentally determined to be 1.40 [53]. By scaling (34) onto the experimental points, Curie temperatures are estimated and listed in Table 8. It is worth noticing that at low temperature the nanoparticles after annealing cannot be saturated with external field as shown in Fig. 37, which means the moments obtained at low temperatures are underestimated, and the true Curie temperature is even lower than the value reported in Table 8. Due to the fact that only two points with a relatively large error bar are available, the determined Curie temperatures have large uncertainty and a size dependence cannot be identified. Nevertheless, all the T_C in nanoparticles are significantly below the bulk value at 750 K.

Table 8: Spin moment per Fe atom in FePt nanoparticles measured at two different temperatures. All the particles are annealed at 700 °C for 30 min.

Diameter (nm)	Low temp. moment (μ_B)	High temp. moment (μ_B)	T_C (K)
4.5	2.14 (15K)	1.63 (290K)	483
5.8	2.39 (11K)	2.10 (280K)	716
6.3	2.38 (15K)	1.72 (300K)	445
9.4	2.58 (15K)	2.19 (300K)	615

The Curie temperature of CoPt can also be estimated from Co moment measured at different temperature as listed in Table 7. Compared to the moment variation measured in bulk CoPt [115], Curie temperature of the CoPt nanoparticles after annealing at 700 °C for 90 min. is around 525 K, which is also much lower than the value of bulk CoPt at 789 K.

The reduced Curie temperature has also been reported for FePt colloidal nanoparticles [65, 112] and thin films [110]. In the case of thin films, the Curie temperature decreases as film thickness reduces, and for 3.5 nm film thickness Curie temperature is reduced to 580 K [110]. The Curie temperature measured on 4 nm colloidal FePt particles, however, depends strongly on the composition. The Curie temperature reaches a maximum of $T_C = 700$ K at $Fe_{50}Pt_{50}$ composition, and decreases rapidly when composition deviates from 50:50 [65]. The Curie temperature estimated for FePt nanoparticles in this study shows similar trend.

6.6 Summary of magnetic properties

Before analysis of magnetic properties, the chemical state of nanoparticles is checked using XAS spectra, which proves that both, FePt and CoPt nanoparticles, are metallic after hydrogen plasma reduction and all annealing steps. The apparent Fe signal intensity decreases by 14% with successive annealing steps ranging from 650 °C to 790 °C. Such decreasing Fe signal intensity is consistent with the reduction of apparent Fe content measured by XPS, as discussed in Section 5.3.

Magnetic properties of FePt and CoPt nanoparticles are investigated in detail by XMCD. 5.8 nm FePt particles after hydrogen plasma reduction show rather low magnetic anisotropy energy, indicated by the low coercive field $\mu_0 H_c = 0.20\,\mathrm{T}$ at 15 K and the superparamagnetic behavior at 300 K. The effective anisotropy energy is estimated to be $K_u = 0.15\,\mathrm{MJ/m^3}$. The magnetic moment per Fe atom measures $\mu_s^{eff} = 2.36 \pm 0.12\,\mu_B$, $\mu_l = 0.19 \pm 0.03\,\mu_B$ at T = 15 K. These results compare well with those obtained in chemically disordered FePt thin films shown in Table 2. FePt nanoparticles after hydrogen plasma reduction are found in the chemically disordered A1 phase. The magnetic moment at ambient temperature is significantly reduced, resulting in $\mu_s^{eff} = 1.83 \pm 0.12\,\mu_B$, $\mu_l = 0.16 \pm 0.03\,\mu_B$. Such reduction of the Fe magnetic moment at higher temperature is related to disruption of magnetic order by thermal excitation. The superparamagnetic response measured at 300 K is fitted by a Langevin function, yielding the saturation magnetization of FePt $M_s = 940\,\mathrm{kA/m}$ at 300 K. Assuming the relative change in M_s with temperature is identical to the relative change of the Fe atomic moment, M_s is estimated to be 1210 kA/m at 15 K, close to 1290 kA/m observed in FePt thin films at 15 K [110].

Annealing at 740 °C for 30 min. significantly increases the magnetic anisotropy energy in the particles. The coercive field increases to $\mu_0 H_c = 0.78\,\mathrm{T}$ at 17 K and the particles cannot be fully saturated with the maximum field of 3 T in the experiments. The moment per Fe atom measures $\mu_s^{eff} = 2.27 \pm 0.12\,\mu_B$, $\mu_l = 0.12 \pm 0.03\,\mu_B$ at 17 K. The slightly reduced moments compared to those directly after reductions is due to limited external field that cannot fully drive the sample to saturation. The "narrow waist" shape of the hysteresis loops at low field of annealed particles indicates the presence of two components in magnetic anisotropy energies. Fitting of hysteresis loops using the Stoner-Wohlfarth model gives a bimodal distribution of the magnetic anisotropy energy, with a narrow component centered at $K_L = 0.10\,\mathrm{MJ/m^3}$ and a broader component centered at $K_H = 1.90\,\mathrm{MJ/m^3}$. It is suggested that the A1 $\rightarrow$ $L1_0$ transformation is not complete in FePt nanoparticles, where the low anisotropy portion corresponds to particles still in the A1 phase and the high anisotropy portion corresponds to particles with partial $L1_0$ order.

Successive annealing from 650 °C to 750 °C gradually increases the portion of particles with higher anisotropy, as indicated by the hysteresis loops measured at room temperature. Annealing at 790 °C, however, decreases this portion again, which suggests that at 790 °C the $L1_0$ is thermodynamically unstable for 5.8 nm particles.

2.6 nm FePt particles show similar increase in magnetic anisotropy energy after annealing at 790 °C. Due to their small dimension, however, these particles do not exhibit ferromagnetism at ambient temperature. Hysteresis loops measured at low temperature also suggest a bimodal distribution of the anisotropy energy, which is confirmed independently by the temperature dependence of hysteresis, where particles with low magnetic anisotropy energy have blocking temperature between 10-45 K and other particles have a broad blocking temperature ranging from 70 to 350 K.

$L1_0$ ordering is also observed in 5.6 nm CoPt particles after annealing at 700 °C for 90 min. According to the shape of the hysteresis, the anisotropy energy in CoPt particles exhibits a bimodal distribution as well. The moment per Co atom measured at 11 K gives $\mu_s^{eff} = 1.60 \pm 0.16\,\mu_B$, $\mu_l = 0.19 \pm 0.04\,\mu_B$. Compared to an equiatomic CoPt thin film sample the spin moment is reduced by 9%, which is expected due to unsaturated sample at 3 T. The μ_l/μ_s^{eff} = 0.11 is comparable to the ratio observed in chemically ordered CoPt thin films of μ_l/μ_s^{eff} = 0.14 [57].

The formation of chemical order is investigated as function of FePt particles diameter after annealing at 700 °C 30 min. In the size range of 2 nm to 10 nm, all the particles show partial chemical order after annealing, and the magnetic anisotropy energies show the bimodal distribution as observed in 5.8 nm particles, with low anisotropy portion at around $K_L = 0.10\,\mathrm{MJ/m^3}$ and high anisotropy portion K_H below 35% of the bulk value of $7\,\mathrm{MJ/m^3}$. The spin moment per Fe atom measured at low temperature shows a systematic decrease as particle size is reduced. In 9.8 nm particles $\mu_s^{eff} = 2.5\,\mu_B$ and is close to that of bulk FePt measured by XMCD, while the spin moment for 2.6 nm particles decreases to $1.9\,\mu_B$. The orbital moment per Fe atom for different particle sizes almost stays constant at 0.1-0.2 μ_B.

The Curie temperatures of FePt and CoPt nanoparticles are estimated by considering the decreased magnetic moment at ambient temperature. Due to lack of complete information about the exact temperature dependence of the magnetic moment, Curie temperatures cannot be determined precisely. However, for all FePt particles the estimated Curie temperatures are found below the bulk value at 750 K. The estimated Curie temperature for 5.6 nm CoPt particles after annealing at 700 °C for 90 min is 525 K, much lower than the bulk value of CoPt at 789 K.

7 Summary

In this thesis ordered arrays of metallic FePt and CoPt nanoparticles are prepared by a micellar method. According to the morphological and chemical characterization in Section 4, particle sizes from 2 - 10 nm having interparticle distances between 20 to 140 nm were achieved. The particles can be reduced to the pure metallic state by hydrogen plasma and the composition of the particles are successfully adjusted within the range where $L1_0$ order is the favored structure in the bulk. Due to large distances between the particles, the samples can be safely annealed to high temperature not risking agglomeration or sintering of nanoparticles. The main focus of the thesis is set to the magnetic properties and oxidation behavior of FePt and CoPt nanoparticles. In this summary the main results are summarized to give a comprehensive view on the particle systems investigated.

FePt nanoparticles after hydrogen plasma reduction are found to be in the chemically disordered state. Elemental specific magnetic moments per Fe atoms agree well with results obtained in chemically disordered FePt thin films according to the XMCD result in Section 6.3, which proves that alloying of Fe and Pt is obtained in the nanoparticles. The low magnetic anisotropy energy of $0.1\,\mathrm{MJ/m^3}$ is consistent with FePt in the A1 phase.

The A1 phase is thermodynamically unfavorable at ambient temperature in the bulk, but the transition to thermodynamically stable $L1_0$ structure is hindered by limited kinetics. To enhance the kinetics annealing above 600 °C is required. In FePt nanoparticle annealing at different temperature only leads to partially chemical order. More specifically, the A1→$L1_0$ transition only takes place in certain portion of the particles during annealing, while other particles stay unchanged in the A1 phase. These transformed particles have a rather broad magnetic anisotropy energy distribution and their average value is below 40% of the magnetic anisotropy energy in FePt with perfect $L1_0$ order. The magnetic anisotropy energy distribution in the particles after annealing then shows a bimodal distribution, which is observed from the distinct "narrow waist" shape of the hysteresis loops measured at low temperature. Such bimodal distribution of magnetic anisotropy energy is observed among all different particles sizes and all different annealing conditions, suggesting that one limiting factor of magnetic anisotropy energy is the limited kinetics of the transition. A higher portion of the particles can be transformed by prolonging the annealing time, which is verified experimentally by successive annealing of 5.8 nm FePt particles at 650 °C. Similar effects can be achieved by enhancing kinetics of the transition, where successive annealing of 5.8 nm particles at increasing temperature from 650 °C to 750 °C also results in increasing number of transformed particles.

However, after annealing these particles at 790 °C, a decrease of the portion of particles with higher magnetic anisotropy is observed, indicating that certain particles with partial chemical order are brought back to A1 phase. This finding suggests that the equilibrium transition temperature between A1 and $L1_0$ phase is above 300 °C and below 790 °C for 5.8 nm FePt nanoparticles. This value is strongly reduced to the bulk value of 1550 K. To achieve high degree of chemical order, the annealing temperature must be kept below such decreased equilibrium transition temperature, which on the other hand leads to limited kinetics. A way out of this dilemma is an annealing step at moderate temperature for very long time, which has been reported by Alloyeau et al. [63] for CoPt nanoparticles.

In the particles already transformed to partial chemical order, the magnetic anisotropy energy is still much lower than the bulk value. In FePt nanoparticles of different sizes and annealed at different temperatures, the distributions of high anisotropy energy portion always cover a wide range of values from nearly 0 up to $7\,MJ/m^3$(bulk value for FePt), with average value below $3\,MJ/m^3$. This suggests that the low magnetic anisotropy energy obtained in transformed FePt nanoparticles is not limited by kinetics, but most probably is an intrinsic property of the nanoparticles.

Different models have been proposed to explain the limited magnetic anisotropy in this thesis. One of the models is that during annealing, Pt atoms have a tendency to segregate towards surfaces. Such Pt segregation is consistent with the observed decrease of apparent Fe signal in XPS and XAS after annealing. Using a core-shell model the decreased Fe signal intensity in XPS spectra is related to an effective Pt segregation layer thickness. For thin film and nanoparticles larger than 9 nm, the Pt segregation layer thickness is found between 0.2-0.3 nm, while for 4.9 nm particles this thickness is below 0.1 nm. Since the thickness of Pt monolayer in close packing is 0.23 nm, Pt segregation layer forms a complete cover layer in larger particles and thin films. Such Pt covering on surfaces would provide an enhanced resistance against oxidation. As discussed in Section 5, the onset of oxidation of annealed 9.8 nm and 11.5 nm FePt nanoparticles is observed for 100-1000 times higher oxygen doses as compared to the identical samples before annealing. On the other hand, due to the incomplete Pt cover layer, oxidation starts almost at the same oxygen exposure in 4.9 nm particles.

The Pt segregation have a profound influence on magnetic properties. Due to the large fraction of surface atoms in nanoparticles, a complete Pt segregation layer will significantly change the composition of the remaining core towards the Fe-rich side. Such deviation from equiatomic composition would disrupt the $L1_0$ chemical order,

thus reducing the magnetic anisotropy energy. On the other hand, the observed size dependence of Fe magnetic moment in nanoparticles can also be explained by the shift of composition. Assuming identical thicknesses of the Pt overlayer are formed due to segregation, in smaller particles the composition will be Fe-rich. According to the XMCD measurement on FePt thin films of different composition [51], the magnetic moment per Fe atom in FePt system is reduced when composition shifts towards the Fe-rich side. This means that for smaller nanoparticles the magnetic moment per Fe atom is expected to be reduced compared to larger particles or bulk FePt, as observed in Section 6.4. Additionally, any deviation from the equiatomic composition significantly reduces the Curie temperature T_C. Although T_C of FePt nanoparticles cannot be determined precisely, in all particles T_C is well below 700 K, which is smaller than the bulk $T_C = 750\,\mathrm{K}$. Such finding is also consistent with the model of Pt segregation and a Fe-rich core.

On the other hand, results from the HRTEM investigations suggest additional explanation for the low magnetic anisotropy. FePt nanoparticles with $L1_0$ order is clearly identified from HRTEM images and the estimated degree of order S should be larger than 0.56. However, a large fraction of the particles contain defects such as twin boundaries and stacking faults as shown in Section 4.3, which divide one particle into several small regions with different crystalline orientations and thus different directions of the easy axes. The effective anisotropy energy of a whole particle consisting of several well-ordered structural grains is the averaged effect of different magneto-crystalline anisotropy terms pointing at different directions. In the extreme case, the final effective anisotropy could be very low although the chemical order in each small region is high.

For CoPt nanoparticles, the process of A1→$L1_0$ transition is very similar to FePt. After annealing at 700 °C for 90 min., a bimodal distribution of anisotropy is observed in 5.6 nm particles. The average anisotropy energy in these particles is estimated to be $1.5\,\mathrm{MJ/m^3}$, which is also below 30% of the CoPt bulk value. From temperature-dependent Co moments, the Curie temperature of CoPt nanoparticles (5.6 nm) is estimated to $T_C = 525\,\mathrm{K}$, which is also much lower than the bulk value of 789 K.

Bibliography

[1] O. A. Ivanov, L. V. Solina, V. A. Demshina, and L. M. Magat, Physics of Metals and Metallography **35**, 81 (1973).

[2] C. L. J M Sanchez, J L Moran-Lopez and M. C. Cadeville, Journal of Physics: Condensed Matter **1**, 491 (1989).

[3] K.H.J. Buschow, editor, *Concise Encyclopedia of Magnetic and Superconducting Materials*, 2 ed. (Elsevier Ltd, Oxford, UK, 2005).

[4] D. M. Newman, M. L. Wears, M. Jollie, and D. Choo, Nanotechnology **18**, 205301 (2007).

[5] S. Sun, Science **287**, 1989 (2000).

[6] S. Sun, Advanced Materials **18**, 393 (2006).

[7] C. Sun, J. S. H. Lee, and M. Zhang, Advanced drug delivery reviews **60**, 1252 (2008).

[8] Q. A. Pankhurst, J. Connolly, S. K. Jones, and J. Dobson, Journal of Physics D: Applied Physics **36**, R167 (2003).

[9] G. A. Somorjai and J. Y. Park, Topics in Catalysis **49**, 126 (2008).

[10] B. Rellinghaus *et al.*, IEEE Transactions on Magnetics **42**, 3048 (2006).

[11] A. Ethirajan *et al.*, Advanced Materials **19**, 406 (2007).

[12] U. Wiedwald, L. Han, J. Biskupek, U. Kaiser, and P. Ziemann, Beilstein Journal of Nanotechnology **1**, 24 (2010).

[13] D. Peng, Journal of Magnetism and Magnetic Materials **277**, 201 (2004).

[14] J. Lau, A. Föhlisch, R. Nietubyc, M. Reif, and W. Wurth, Physical Review Letters **89** (2002).

[15] M. Chen, J. Kim, J. P. Liu, H. Fan, and S. Sun, Journal of the American Chemical Society **128**, 7132 (2006).

[16] Z. Wu *et al.*, Solid State Phenomena **154**, 89 (2009).

[17] M. Aslam, L. Fu, S. Li, and V. P. Dravid, Journal of colloid and interface science **290**, 444 (2005).

[18] S. Sun, C. B. Murray, D. Weller, L. Folks, and A. Moser, Science **287**, 1989 (2000).

[19] G. Kästle *et al.*, Advanced Functional Materials **13**, 853 (2003).

[20] I. I. Potemkin *et al.*, Langmuir **15**, 7290 (1999).

[21] M. Antonietti, S. Heinz, M. Schmidt, and C. Rosenauer, Macromolecules **27**, 3276 (1994).

[22] S. Mössmer *et al.*, Macromolecules **33**, 4791 (2000).

[23] M. Antonietti, S. Förster, J. Hartmann, and S. Oestreich, Macromolecules **29**, 3800 (1996).

[24] S. Förster and M. Antonietti, Advanced Materials **10**, 195 (1998).

[25] J. Bansmann *et al.*, Langmuir **23**, 10150 (2007).

[26] R. Skomski, *Simple Models of Magnetism (Oxford Graduate Texts)* (OUP Oxford, 2008).

[27] S. Okamoto *et al.*, Physical Review B **66**, 024413 (2002).

[28] L. Nèel, Ann. Géophys. **5**, 99 (1949).

[29] W. Brown, Physical Review **130**, 1677 (1963).

[30] S. Bedanta and W. Kleemann, Journal of Physics D: Applied Physics **42**, 013001 (2009).

[31] C. Kittel, Reviews of Modern Physics **21**, 541 (1949).

[32] E. C. Stoner and E. P. Wohlfarth, Philosophical Transactions of the Royal Society A: Mathematical, Physical and Engineering Sciences **240**, 599 (1948).

[33] M. A. Chuev and J. Hesse, Journal of Physics: Condensed Matter **19**, 506201 (2007).

[34] W. Wernsdorfer, Journal of Magnetism and Magnetic Materials **242-245**, 132 (2002).

[35] H. F. Du and A. Du, Journal of Applied Physics **99**, 104306 (2006).

[36] B. Stahl *et al.*, Physical Review B **67**, 014422 (2003).

[37] K. Barmak *et al.*, Journal of Applied Physics **98**, 033904 (2005).

[38] P. Villars, L. D. Calvert, and W. B. Pearson, *Pearson's Handbook of Crystallographic Data for Intermetallic Phases* (ASM International, Cleveland, OH, 1991).

[39] G. Daalderop, P. Kelly, and M. Schuurmans, Physical Review B **44**, 12054 (1991).

[40] M. F. Campos and F. J. G. Landgraf, Journal of Phase Equilibria **21**, 443 (2000).

[41] K. Coffey, M. Parker, and J. Howard, IEEE Transactions on Magnetics **31**, 2737 (1995).

[42] Z. R. Dai, S. Sun, and Z. L. Wang, Nano Letters **1**, 443 (2001).

[43] M. Müller and K. Albe, Physical Review B **72**, 094203 (2005).

[44] Y. K. Takahashi, Journal of Applied Physics **95**, 2690 (2004).

[45] D. C. Berry and K. Barmak, Journal of Applied Physics **102**, 024912 (2007).

[46] R. Kozubski *et al.*, Journal of Phase Equilibria and Diffusion **26**, 482 (2005).

[47] C.-H. Lai, C.-H. Yang, and C. C. Chiang, Applied Physics Letters **83**, 4550 (2003).

[48] U. Wiedwald *et al.*, Applied Physics Letters **90**, 062508 (2007).

[49] F. Bolzoni, F. Leccabue, R. Panizzieri, and L. Pareti, IEEE Transactions on Magnetics **20**, 1625 (1984).

[50] I. Galanakis, M. Alouani, and H. Dreyssé, Journal of Magnetism and Magnetic Materials **242-245**, 27 (2002).

[51] C. Antoniak *et al.*, Journal of Physics: Condensed Matter **21**, 336002 (2009).

[52] J. Bogner *et al.*, Physical Review B **58**, 14922 (1998).

[53] J. Lyubina *et al.*, Applied Physics Letters **89**, 032506 (2006).

[54] M. M. Bendele, *Optimierung epitaktischer FePt Schichten* (Diplomarbiet, Universität Ulm, 2008).

[55] C. J. Sun *et al.*, Japanese Journal of Applied Physics **45**, 2539 (2006).

[56] G. Chang *et al.*, Physical Review Letters **87**, 067208 (2001).

[57] W. Grange *et al.*, Physical Review B **62**, 1157 (2000).

[58] J. MacLaren, R. Duplessis, R. Stern, and S. Willoughby, IEEE Transactions on Magnetics **41**, 4374 (2005).

[59] C. Chen *et al.*, Physical Review Letters **75**, 152 (1995).

[60] R. A. Ristau, K. Barmak, L. H. Lewis, K. R. Coffey, and J. K. Howard, Journal of Applied Physics **86**, 4527 (1999).

[61] J. Liu, K. Elkins, D. Li, V. Nandwana, and N. Poudyal, IEEE Transactions on Magnetics **42**, 3036 (2006).

[62] F. Tournus, N. Blanc, A. Tamion, M. Hillenkamp, and V. Dupuis, Physical Review B **81**, 220405 (2010).

[63] D. Alloyeau *et al.*, Nature materials **8**, 940 (2009).

[64] B. Yang, M. Asta, O. N. Mryasov, T. J. Klemmer, and R. W. Chantrell, Acta Materialia **54**, 4201 (2006).

[65] C.-B. Rong, Y. Li, and J. P. Liu, Journal of Applied Physics **101**, 09K505 (2007).

[66] M. E. Gruner, Journal of Physics D: Applied Physics **41**, 134015 (2008).

[67] J. Bansmann *et al.*, Surface Science Reports **56**, 189 (2005).

[68] P. Hawkes and J. C. Spence, *Science of Microscopy* (Springer US, 2006).

[69] D. B. Williams and C. B. Carter, *Transmission Electron Microscopy: A Textbook for Materials Science* (Springer US, 2005).

[70] R. Wang *et al.*, Physical Review Letters **100**, 017205 (2008).

[71] D. Alloyeau *et al.*, Ultramicroscopy **108**, 656 (2008).

[72] J. Biskupek *et al.*, Ultramicroscopy **110**, 820 (2010).

[73] C. Beeli, B. Doudin, J.-P. Ansermet, and P. A. Stadelmann, Ultramicroscopy **67**, 143 (1997).

[74] A. C. Daykin and A. K. Petford-Long, Ultramicroscopy **58**, 365 (1995).

[75] P. Schattschneider *et al.*, Ultramicroscopy **108**, 433 (2008).

[76] J. F. Watts and J. Wolstenholme, *An Introduction to Surface Analysis by XPS and AES* (Wiley UK, 2003).

[77] W. R. Mason, *Magnetic Circular Dichroism Spectroscopy* (Wiley UK, 2007).

[78] C. T. Chantler, Journal of Physical and Chemical Reference Data **24**, 71 (1995).

[79] C. T. Chantler, Journal of Physical and Chemical Reference Data **29**, 597 (2000).

[80] J. Yeh and I. Lindau, Atomic Data and Nuclear Data Tables **32**, 1 (1985).

[81] W. S. M. Werner, Surface and Interface Analysis **18**, 217 (1992).

[82] W. H. Gries, Surface and Interface Analysis **24**, 38 (1996).

[83] S. Tanuma, C. J. Powell, and D. R. Penn, Surface and Interface Analysis **25**, 25 (1997).

[84] M. P. Seah and W. A. Dench, Surface and Interface Analysis **1**, 2 (1979).

[85] D. Shirley, Physical Review B **5**, 4709 (1972).

[86] S. Tougaard, Surface and Interface Analysis **11**, 453 (1988).

[87] J. Végh, Journal of Electron Spectroscopy and Related Phenomena **151**, 159 (2006).

[88] J. Stöhr, Journal of Magnetism and Magnetic Materials **200**, 470 (1999).

[89] W. L. O'Brien, B. P. Tonner, G. R. Harp, and S. S. P. Parkin, Journal of Applied Physics **76**, 6462 (1994).

[90] C. Ederer, M. Komelj, and M. Fähnle, Physical Review B **68**, 052402 (2003).

[91] C. Piamonteze, P. Miedema, and F. M. F. de Groot, Physical Review B **80**, 184410 (2009).

[92] J. Lee *et al.*, Journal of Physics: Condensed Matter **9**, L137 (1997).

[93] C. Antoniak *et al.*, Physical Review Letters **97**, 117201 (2006).

[94] H. Winick, *Synchrotron Radiation Sources: A Primer* (World Scientific Publishing Co Pte Ltd, 1995).

[95] W. L. O'Brien and B. P. Tonner, Physical Review B **50**, 12672 (1994).

[96] K. Fauth, Applied Physics Letters **85**, 3271 (2004).

[97] T. Regan *et al.*, Physical Review B **64**, 214422 (2001).

[98] R. Nakajima, J. Stöhr, and Y. U. Idzerda, Physical Review B **59**, 6421 (1999).

[99] A. Kleibert, K.-H. Meiwes-Broer, and J. Bansmann, Physical Review B **79**, 125423 (2009).

[100] U. Wiedwald *et al.*, ChemPhysChem **6**, 2522 (2005).

[101] P. de la Presa *et al.*, Journal of Applied Physics **103**, 103909 (2008).

[102] C. Parkinson, Surface Science **545**, 19 (2003).

[103] B. Kern, *Mizellare Herstellung und Charakterisierung von magnetischen Nanopartikeln* (Diplomarbiet, Universität Ulm, 2006).

[104] L. Han, U. Wiedwald, B. Kuerbanjiang, and P. Ziemann, Nanotechnology **20**, 285706 (2009).

[105] P. C. J. Graat and M. A. J. Somers, Applied Surface Science **100-101**, 36 (1996).

[106] H.-G. Boyen *et al.*, Advanced Materials **17**, 574 (2005).

[107] G. R. Wallwork, Reports on Progress in Physics **39**, 401 (1976).

[108] B. Yang, M. Asta, O. Mryasov, T. Klemmer, and R. Chantrell, Scripta Materialia **53**, 417 (2005).

[109] E. Goering, A. Fuss, W. Weber, J. Will, and G. Schütz, Journal of Applied Physics **88**, 5920 (2000).

[110] T. Bublat and D. Goll, Journal of Applied Physics **108**, 113910 (2010).

[111] K. Zürn, *Herstellung und Untersuchung geordneter magnetischer Kobaltnanoteilchen*, PhD thesis, Universität Ulm, 2009.

[112] H. M. Lu, Z. H. Cao, C. L. Zhao, P. Y. Li, and X. K. Meng, Journal of Applied Physics **103**, 123526 (2008).

[113] Y. Ding and S. A. Majetich, Applied Physics Letters **87**, 022508 (2005).

[114] B. Rellinghaus, Journal of Magnetism and Magnetic Materials **266**, 142 (2003).

[115] J. Lyubina, O. Gutfleisch, and O. Isnard, Journal of Applied Physics **105**, 07A717 (2009).

[116] C.-B. Rong *et al.*, Advanced Materials **18**, 2984 (2006).

[117] F. Parker, M. Foster, D. Margulies, and A. Berkowitz, Physical Review B **47**, 7885 (1993).

[118] M. Kuz'min, Physical Review Letters **94**, 107204 (2005).

Acknowledgment

The presented work in this thesis was only possbile to achieve with the generous help and collaboration with many people. Here, I would like to give my sincere acknowledgments to:

- Prof. Dr. P. Ziemann, for accepting me as Ph. D. student and offering me the opportunity of this project. His general guidance and the critical discussions is indispensable for my research work and his expansive scientific horizon also broadens my knowledge.

- Prof. Dr. U. Kaiser, for her great help in structure investigation by TEM and discussions and for her kindly acceptance to be my second referee.

- Dr. U. Wiedwald, for excellent collaborations in almost *every* details of the research work over many years. The whole work would not be possible without his kind assistance and constant motivation. As a foreign student in Germany I also received numerous personal assistance from him. And thanks for organizing our group entertaining events such as bowling every few months. It was of great fun!

- Prof. Dr. H.-G. Boyen, for his brilliant idea about FePt oxidation behavior and many motivating discussions.

- Dr. J. Biskupek and Dr. Z. Zhang, for their collaborations in the HRTEM investigation of FePt nanoparticles. Also for discussions concerning my questions about HRTEM.

- Prof. Dr. K. Fauth, "master of XMCD", for allowing me to use his excellent instrument, on which the XMCD data in this thesis was collected.

- B. Kern, for her collaboration in preparation and characterization of FePt nanoparticles.

- B. Kuerbanjian and L. Shan for their collaboration in the FePt oxidation experiments and the preparation of CoPt nanoparticles. Also for their friendly accompany during the tedious XMCD measurement at BESSY II.

- M. Bendele, for the preparation of FePt thin films.

- S. Nau, for his help in the XMCD measurement and preparation of Pt thin films.

- AOR Dr. A. Plettl, for his kindly scientific discussions and for allowing me to work in the clean room. Special thanks for his attribution to the XMCD measurement at BESSY II.
- Dr. A. Klimmer, for his assistance in XMCD measurements at BESSY and his contribution of strong muscle in the lab.
- C. Pfahler, for his kindly help on all the details about working in the clean room. His experience about thin film deposition helped me quite a lot.
- M. Trautvetter, for scientific discussions and contribution to the XMCD measurement at BESSY II. His happy and optimistic atmosphere gives greater motivation in the group. Special thanks for his help in the exam procedure of Ph.D. and correction of the German abstract.
- Prof. Dr. B. Koslowski, for many hard and critical discussions and for helping me with the computer problems.
- Prof. Dr. P. Walther, for giving me the access to SEM and TEM.
- Dr. C. Hoffmann-Richter, for the AFM access.
- Z. Wu, for the collaboration of FePt nanowires and his personal friendship.
- Dr. K. Küpper and Dr. D. Schmitz, for their collaboration in XMCD measurements on NiO nanoparticles.
- H.-D. Kerpes and W. Kaufmann, for their technical support in all the instruments and for the arrangement of liquid helium supply, and also for the design of many additional parts in our instruments. The acknowledgment also goes to the workshop of Ulm University, where all these special parts are manufactured.
- V. Besserer, for the help on electronics. Thank for his maintenance to the old electronic devices so that they are still alive. Also thanks for the nice music at our Christmas parties.
- G. Dinger and T. Hager, for their help in administrative affairs. Thanks to their dedicated work I have never encountered difficulties when dealing with official documents. They also gave me timely assistance on visa applications.
- All the colleagues of Institut für Festkörperphysik, for their kindly help and scientific discussions. It was a great pleasure to work in such an open and active atmosphere.

- Sonderforschungsbereich SFB 569 and Landesschwerpunkt Baden-Württemberg for the financial support.
- And also numerous contributors of the open-source programs. With their excellent software I can analyze the experimental data and write the whole thesis.
- And at last the most important, my family, supporting me my whole work and life. And especially for my wife Meifang, who supported me during the writing of this thesis with patience and care.

Curriculum vitae

Persönliche Angaben:

Name:	Luyang Han
Geburtstag, -ort:	01.05.1983 in Jingzhou, Hubei, V.R. China
Familienstand:	verheiratet, ein Kind
Anschrift:	Stuifenweg 4, 89075 Ulm

Schulbildung:

09/1989 - 06/1994	Grundschule Jingzhou, Jingzhou
09/1994 - 06/1997	Mittelschule Yindu, Jingzhou
09/1997 - 06/2000	Mittelschule Jingzhou, Jingzhou
	Bestehen der staatlichen Hochschulaufnahmeprüfung

Akademischer Werdegang:

09/2000 - 07/2004	Beijing Universität für Luft- und Raumfahrt
	Studiengang: Materialwissenschaft
	Abschluss: Bachelor of Engineering
10/2004 - 10/2006	Universität Ulm
	Studiengang: Advanced Materials
	Abschluss: Master of Science
seit 11/2006	Angestellt in der Abteilung Festkörperphysik, Universität Ulm
	Forschungsarbeit auf der Herstellung und Charakterisierung
	von magnetischen Nanopartikeln

Publications and conference contributions

Publication list

A. Ethirajan, U. Wiedwald, H.-G. Boyen, B. Kern, L. Han, A. Klimmer, F. Weigl, G. Kästle, P. Ziemann, K. Fauth, J. Cai, R. J. Behm, A. Romanyuk, P. Oelhafen, P. Walther, J. Biskupek and U. Kaiser
A Micellar Approach to Magnetic Ultrahigh-Density Data-Storage Media: Extending the Limits of Current Colloidal Methods
Advanced Materials **19**, 406-410 (2007)

U. Wiedwald, A. Klimmer, B. Kern, L. Han, H.-G. Boyen, P. Ziemann and K. Fauth
Lowering of the $L1_0$ ordering temperature of FePt nanoparticles by He^+ ion irradiation
Applied Physics Letters **90**, 062508 (2007)

L. Han, U. Wiedwald, B. Kuerbanjiang and P. Ziemann
Fe oxidation versus Pt segregation in FePt nanoparticles and thin films.
Nanotechnology **20**, 285706 (2009)

Z. Wu, H. Dong, A.L. Chuvilin, U. Wiedwald, L. Han and C.E. Krill
FePt Nanorods and Nanowires for Novel Ferrofluids
Solid State Phenomena **154**, 89-94 (2009)

J. Biskupek, J.R. Jinschek, U. Wiedwald, M. Bendele, L. Han, P. Ziemann and U. Kaiser
Identification of magnetic properties of few nm sized FePt crystalline particles by characterizing the intrinsic atom order using aberration corrected S/TEM
Ultramicroscopy **110**, 820-825 (2010)

M.Y. Ge, L.Y. Han, U. Wiedwald, X.B. Xu, C. Wang, K. Kuepper, P. Ziemann and J.Z. Jiang
Monodispersed NiO nanoflowers with anomalous magnetic behavior
Nanotechnology **21**, 425702 (2010)

T. Härtling, T. Uhlig, A. Seidenstücker, N.C. Bigall, P. Olk, U. Wiedwald, L. Han, A. Eychmüller, A. Plettl, P. Ziemann and L.M. Eng
Fabrication of two-dimensional Au@FePt core-shell nanoparticle arrays by photochemical metal deposition
Applied Physics Letters **96**, 183111 (2010)

S. Saranu, S. Selve, U. Kaiser, L. Han, U. Wiedwald, P. Ziemann and U. Herr
Effect of large mechanical stress on the magnetic properties of embedded Fe nanoparticles

(Submitted to Beilstein Journal of Nanotechnology)

A. Manzke, A. Plettl, U. Wiedwald, L. Han, P. Ziemann, E. Schreiber, U. Ziener, N. Vogel, K. Landfester, K. Fauth, J. Biskupek and U. Kaiser
Bimetallic alloy nanoparticles prepared by miniemulsions
(In preparation)

Conference contributions

SFB Young Researcher Meeting 2006
Location: Marburger Hütte, Kleinwalsertal
Date: 26.07.2006 - 28.07.2006
Ordered FePt Nanoparticle Array (Talk)

Kompetenznetz »Funktionelle Nanostrukturen« Baden-Württemberg, Statusworkshop 2006
Location: Evangelische Akademie Baden, Bad Herrenalb
Date: 14.09.2006 - 15.09.2006
A micellar approach to arrays of FePt alloy nanoparticles (Talk)

Seeheim Conference on Magnetism 2007
Location: Holiday-Inn, Frankfurt
Date: 26.08.2007 - 30.08.2007
Preparation and Characterization of Ordered Nanoparticle Ensemble of Magnetic Binary Alloy (Poster)

DPG-Tagung 2008
Location: TU Berlin
Date: 25.02.2008 - 29.02.2008
The Oxidation Behavior of FePt Nanoparticles in A1 and $L1_0$ Phase (poster)

Kompetenznetz »Funktionelle Nanostrukturen« Baden-Württemberg, Statusworkshop 2008
Location: Evangelische Akademie Baden, Bad Herrenalb
Date: 8.10.2008 - 10.10.2008
Oxidation behavior of FePt nanoparticles and films (Talk)

Trends in Nanoscience 2009
Location: Kloster Irsee
Date: 10.02.2010 - 11.02.2010
Structural and Magnetic Investigations on Metallic and Partially Oxidized FePt Nanoparticles (Poster)

DPG-Tagung 2009
Location: TU Dresden
Date: 22.03.2009 – 27.03.2009
Oxidation Behavior of FePt Nanoparticles and Films (Talk)

The International Conference on Magnetism 2009
Location: Karlsruhe
Date: 06.07.2009 - 31.07.2009
Structure and Magnetism of A1 and L10 FePt Nanoparticles (Poster)

DPG-Tagung 2010
Location: Uni Regensburg
Date: 21.03.2010 - 26.03.2010
Alloying of Co nanoparticles on differently oriented Pt films and its influence on magnetic properties (Talk)

Declaration

I declare, that the presented thesis is written by myself independently using only the allowed resources. Furthermore, all sentences in the text, whose words or meaning is adopted from other work, are denoted as citation with declaration of the original reference.

Erklärung

Hiermit erkläre ich, dass ich die vorliegende Arbeit selbständig und nur mit den angegebenen Hilfsmitteln angefertigt habe und dass alle Stellen, die im Wortlaut oder dem Sinne nach an- deren Werken entnommen sind, durch Angabe der Quellen als Entlehnung kenntlich gemacht worden sind.

Ulm, den 17.02.2011

Luyang Han

_____